REPUBLIC OF TURKEY

ADANA ALPARSLAN TÜRKEŞ SCIENCE AND TECHNOLOGY UNIVERSITY

GRADUATE SCHOOL OF NATURAL AND APPLIED SCIENCES

DEPARTMENT OF NANOTECHNOLOGY AND ENGINEERING SCIENCES

INVESTIGATION OF STRUCTURAL, MAGNETIC AND MAGNETOCALORIC PROPERTIES OF Ho AND Fe SUBSTITUTED $CoCr_2O_4$ SPINEL NANOPARTICLES

SEMİRAMİS GÜLKESEN

MASTER OF SCIENCE

ADANA 2020

REPUBLIC OF TURKEY
ADANA ALPARSLAN TÜRKEŞ SCIENCE AND TECHNOLOGY UNIVERSITY

GRADUATE SCHOOL OF NATURAL AND APPLIED SCIENCES
DEPARTMENT OF NANOTECHNOLOGY AND ENGINEERING SCIENCES

INVESTIGATION OF STRUCTURAL, MAGNETIC AND MAGNETOCALORIC PROPERTIES OF Ho and Fe SUBSTITUTED $CoCr_2O_4$ SPINEL NANOPARTICLES

SEMİRAMİS GÜLKESEN
MASTER OF SCIENCE

SUPERVISOR
ASSOC.PROF.DR. MUSTAFA AKYOL

ADANA 2020

I hereby declare that all information in this thesis has been obtained and presented in accordance with academic rules and ethical conduct. I also declare that, as required by these rules and conduct, I have fully cited and referenced all information that is not original to this work.

Semiramis GÜLKESEN

ABSTRACT

INVESTIGATION OF STRUCTURAL, MAGNETIC AND MAGNETOCALORIC PROPERTIES OF Ho AND Fe SUBSTITUTED $CoCr_2O_4$ SPINEL NANOPARTICLES

Semiramis GÜLKESEN

Department of Nanotechnology and Engineering Sciences

Supervisor: Assoc. Prof. Dr. Mustafa AKYOL

June 2020, 91 pages

In this study, structural, magnetic and magnetocaloric properties of $Co(Cr_{1-x}Fe_x)_2O_4$ ($0.0 \leq x \leq 1.0$) spinel multiferroic compounds produced by sol-gel method were investigated. Structural, morphological and elemental properties of all synthesized compounds were investigated by measuring X-Ray Diffraction (XRD), Scanning Electron Microscope (SEM) and Energy-Dispersive X-Ray Spectrometry (EDS). It is determined that $Co(Cr_{1-x}Fe_x)_2O_4$ ($0.0 \leq x \leq 1.0$) spinel materials have cubic crystal structure and the lattice parameter increases with increasing Fe content. In addition, it is observed from the SEM images that the particle size increases with Fe content. From the elemental analysis results, it has been determined that the atomic percent ratios of the synthesized compounds are close to the desired values. It is observed that the magnetization values both temperature and magnetic field dependence increase with increasing of Fe content in the main structure. It is determined that the magnetic transition temperature increases with increasing Fe content in the main structure. Magnetic entropy change of the samples is determined from isothermal magnetization measurements taken in the magnetic transition temperature region. Furthermore, various concentrations of Ho^{3+} ions were substituted by Cr^{3+} and Fe^{3+} ions in $CoCrFeO_4$. The structural, magnetic and magnetocaloric properties of the synthesized Ho-substituted $CoCrFeO_4$ compounds were investigated using the measurement methods mentioned above. No significant change in magnetic transition temperature is observed by Ho^{3+} ions in $CoCrFeO_4$ compound. However, it is observed that the magnetization value decreases with increasing amount of Ho.

Keywords: Spinel materials, multifferroic, sol-gel, magnetic entropy.

ÖZET

Ho VE Fe YERLEŞTİRİLMİŞ $CoCr_2O_4$ SPİNEL NANOPARÇACIKLARIN YAPISAL, MANYETİK VE MANYETOKALORİK ÖZELLİKLERİNİN İNCELENMESİ

Semiramis GÜLKESEN
Nanoteknoloji ve Mühendislik Bilimleri Anabilim Dalı
Danışman: Doç. Dr. Mustafa AKYOL
Haziran 2020, 91 sayfa

Bu çalışmada, sol-jel yöntemi ile üretilen $Co(Cr_{1-x}Fe_x)_2O_4$ ($0.0 \leq x \leq 1.0$) spinel yapıdaki multiferroik bileşiklerinin yapısal, manyetik ve manyetokalorik özellikleri incelenmiştir. Sentezlenen tüm bileşiklerin yapısal, morfolojik ve elementel özellikleri X-Işını Kırınımı (XRD), Taramalı Elektron Mikroskobu (SEM) ve Enerji Dağılımlı X-Işını Spektrometresi (EDS) ölçümleri yapılarak araştırılmıştır. $Co(Cr_{1-x}Fe_x)_2O_4$ ($0.0 \leq x \leq 1.0$) spinel yapıdaki bileşiklerin kübik kristal yapıda olduğu ve Fe miktarının artması ile örgü parametresinin de arttığı belirlenmiştir. Ayrıca SEM görüntülerinden parçacık boyutunun da Fe miktarı ile birlikte arttığı gözlenmiştir. Elementel analiz sonuçlarından, sentezlenen bileşiklerin atomik yüzde oranlarının hedeflenen değerlere yakın olduğu belirlenmiştir. Ana yapıdaki Fe miktarının artması ile mıknatıslanmanın da arttığı sıcaklığa ve manyetik alana bağlı gerçekleştirilen mıknatıslanma ölçümlerinden gözlenmiştir. Ana yapıdaki Fe oranının artması ile manyetik geçiş sıcaklığının da arttığı belirlenmiştir. Manyetik geçiş sıcaklığı bölgesinde alınan izotermal manyetizasyon ölçümlerinden manyetik entropi değişimi belirlenmiştir. Ayrıca farklı oranlarda Ho^{3+} iyonları $CoCrFeO_4$ bileşiğindeki Cr^{3+} ve Fe^{3+} iyonları ile yer değiştirecek şekilde katkılanmıştır. Sentezlenen bileşiklerin yapısal, manyetik ve manyetokalorik özellikleri yukarıda belirtilen ölçüm yöntemleri kullanılarak araştırılmıştır. $CoCrFeO_4$ bileşiğine Ho^{3+} eklenmesi ile manyetik geçiş sıcaklığında dikkate değer bir değişme gözlenmemiştir. Ancak, mıknatıslanma değeri Ho miktarının artması ile azaldığı gözlenmiştir.

Anahtar Kelimeler: Spinel malzemeler, multiferroik, sol-jel, manyetik entropy.

I dedicate this thesis to my family.

ACKNOWLEDGEMENTS

First of all, I would like to express my gratitude to all these people who were with me during the completion of this thesis, contributing to my scientific and life experience. Thank you very much to these people.

In particular, I present my sincere gratitude to my supervisor, Assoc.Prof.Dr. Mustafa AKYOL. Throughout my master's studies, I am grateful for her endless support, experience in nanotechnology, guidance, advice, encouragement and all help in my research projects. I must say that Assoc.Prof.Dr. Mustafa AKYOL, I could not complete my thesis if he had not always supported me at the beginning of my master's degree and had not always been with me. He always helped me whenever I encountered a problem and needed guidance. His compassionate personality, educator and researcher spirit has always been a light to me and will continue to be my whole life.

Secondly, I would like to thank Assoc.Prof.Dr. Ahmet EKİCİBİL, Assoc.Prof.Dr. Mustafa GÜNEŞ and Assoc.Prof.Dr. Efe EFEOĞLU for their supports and assistance while starting my graduate education.

Thirdly, I would like to thank our group members and colleagues who Assoc.Prof.Dr. Ali Osman AYAŞ, Dr. Selda KILIÇ ÇETİN, İdris ADANUR, Kutluhan Utku TÜMEN, Burak KIVRAK and Ahmet ÜNVERDİ for their helps and support.

Finally, I extend my deepest thanks to my dear grandmother who looked after to me during my childhood, and to my mom, dad and brother.

I would like to thank to all employees of Graduate School of Natural and Applied Sciences for educational helps and thank to Scientific Research Council for financial support. This thesis was financially supported by Adana Alparslan Türkeş Science and Technology University Scientific Research Council with project number of 19332004.

TABLE OF CONTENTS

LIST OF FIGURES

LIST OF TABLES

NOMENCLATURE

Å	: Angstrom
$\vec{a}$	: Acceleration
$\vec{B}$	: Magnetic field
C	: Curie constant
°C	: Celsius degree
D	: Crystallite size
$\vec{E}$	: Electric field
e^-	: Electron charge
EDS	: Energy-Dispersive X-Ray Spectroscopy
eV	: Electron Volts
FC	: Field Cooled
g	: Gram
hkl	: Miller indices
$\vec{H}$	: External magnetic field
H_c	: Coercive field
I	: Current
J	: Current density
$\vec{J}$	: Total angular momentum
j	: Total angular momentum quantum number
K	: Kelvin
k_B	: Boltzmann Constant
$\vec{L}$	: Orbital angular momentum
l	: Orbital angular momentum quantum number
m	: Mass
$\vec{M}$	: Magnetization vector
M_s	: Saturation Magnetization
Oe	: Oersted
PPMS	: Physical Properties Measurement System

R	: Radius
$\vec{S}$	: Spin angular momentum quantum number
SEM	: Scanning Electron Microscopy
T	: Temperature
T_B	: Blocking temperature
T_C	: Curie temperature
T_N	: Neel temperature
VSM	: Vibrating Sample Magnetometer
ZFC	: Zero Field Cooled
XRD	: X-Ray Diffraction
Q	: Temperature constant
τ	: Relaxation time
V	: Speed
χ	: Magnetic susceptibility
λ	: Wavelength
θ	: Bragg angle
μ	: Magnetic moment
μ_B	: Bohr magnetron
μ_0	: Free space magnetic permeability
γ	: Gyromagnetic ratio
π	: Pi number

1. INTRODUCTION

Nanoscience continues to develop technologies with new scientific developments for years. It refers to the science and technology of materials whose dimensions range from 1 nanometer to 100 nanometers. The structures of the materials on the nano scale have not been fully explored. The interface determines the physical properties of nanomaterials. Quantum phenomena are the ultimate foundation of the properties of atoms and molecules, but they are hidden behind classical behavior in macroscopic matter and structures. This opens up a wide world of new applications of even well-known materials.

1.1. Spinel structures

Multiferroic materials show the ferroelectric and ferromagnetic order, which simultaneously exhibit unique physical properties due to the mapping between magnetic and electrical parameters. A schematic illustration of a muştiferroic materials' magnetic and electric ordering. It is used in practical applications in many important fields such as electrochemical sensors, biomedical materials, active components of ferrofluids, electromagnetic sensors, telecommunication systems and data storage medium (Akyol, Adanur, Ayaş, & Ekicibil, 2017; Galdikas, Martūnas, & Šetkus, 1992; Gopal Reddy, Manorama, & Rao, 1999; He, 2014; Iqbal & Siddiquah, 2008; Kim, Hiraga, Morita, & Sakka, 2001; Koseoglu et al., 2008; Zakrzewska, 2001).

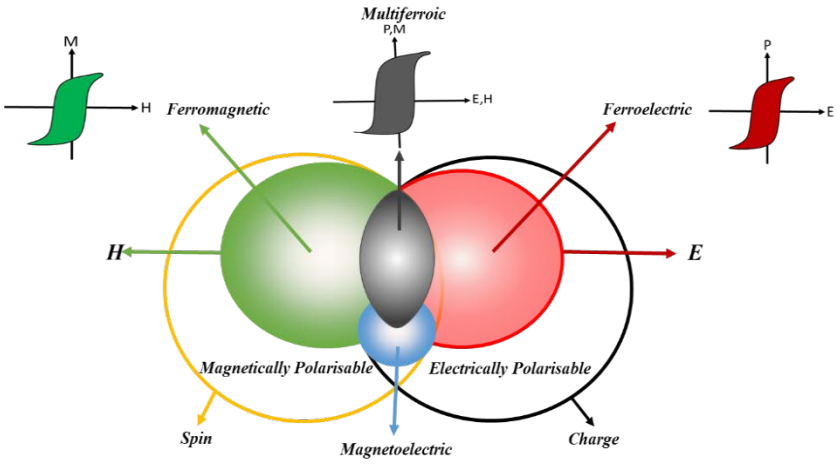

Figure 1.1. The schematic illustration of multiferroic properties by combining magnetic and ferroelectric ordering.

A wide variety of multiferroic material families have been studied to improve their multiferroic properties. Among them, the spinel materials formed as AB_2O_4, where A is a tetrahedral divalent cation and B is a trivalent cation of the octahedral regions of multiferroic materials, which has been explored in extensive studies due to their interesting physical properties. Figure 1.2 shows spinel crystal structure.

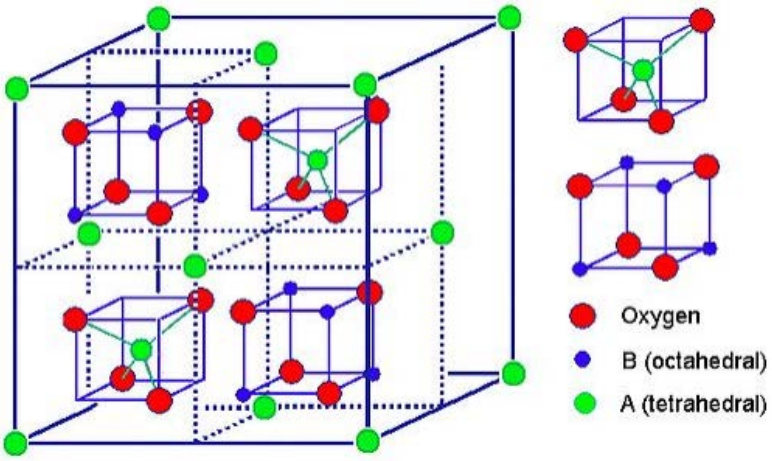

Figure 1.2. Spinel structure ("Spinel structure," 2020).

Many inorganic oxides consist of a face-centered cubic lattice of ions held together by interstitial cations. There are two types of spaces between the elements of such a cage, the four closest neighbors of which are tetrahedral cracks and the six closest neighbors are octahedral spaces. If all tetrahedral places are empty and all octahedral places are filled, it has a crystal rock salt structure; If only tetrahedral places are occupied, the crystal has a zinc-blend structure.

Depending on the cation distribution on different crystallographic regions, spinel compounds can generally be divided into three categories.

1. Normal spinel structure
2. Inverse spinel structure
3. Mixed spinel structure

1.1.1. Normal spinel structures

In normal spinel structure, the unit cell is made up of 8 FCC cells. The anions (here we considered oxide ions: O^{2-}) occupy the FCC lattice points. The divalent A^{2+} cations occupy 1/8 of the tetrahedral voids, whereas the trivalent B^{3+} cations occupy 1/2 of octahedral voids. A normal spinel materials chemical formula can be represented as $(A^{2+})^{tet}(B^{3+})_2{}^{oct}O_4$.

1.1.2. Inverse spinel structures

In inverse spinel structure, the A^{2+} ions occupy the octahedral voids, whereas 1/2 of B^{3+} ions occupy the tetrahedral voids and the other 1/2 occupy octahedral sites like $B(AB)O_4$. The inverse spinel materials chemical formula can be represented as $(B^{3+})^{tet}(A^{2+}B^{3+})^{oct}O_4$.

1.1.3. Mixed spinel structures

This kind of spinel materials are intermediate between the normal and inverse spinel structure. If the divalent cations (A^{2+}) are present on both tetrahedral and octahedral sites, the spinel is mixed spinel structure. A mixed spinel materials chemical formula can be represented as $(A^{2+}{}_{1-m}B^{3+}{}_k)^{tet}(A^{2+}{}_mB^{3+}{}_{2-k})^{oct}O_4$.

In the following table (Table 1.1), the possible spinel structures that are combined from various combinations of metals in periodic table are tabulated.

Table 1.1. Normal and inverse spinel structures based on occupation of A^{2+} and B^{3+} ions in spinel structure.

A^{2+}	B^{3+}	Structure
Non transition metal or d^0 or d^5 or d^{10} transition metal	Non transition metal	Normal spinel
Non transition metal or d^0 or d^5 or d^{10} transition metal	A transition metal with d^1 or d^2 or d^3 or d^4 or d^6 or d^7 or d^8 or d^9 configurations	Normal spinel
A transition metal with d^1 or d^2 or d^3 or d^4 or d^6 or d^7 or d^8 or d^9 configurations	Non transition metal or transition meta with d^0 or d^5 or d^{10} configurations	Inverse spinel
Transition metal with higher CFSE* value	Transition metal with lower CFSE* value	Inverse spinel

*CFSE: Crystal field stabilization energy.

1.2. Introduction to magnetism

According to the classical atomic model, electrons create an I current in the opposite direction to their motions while moving around a nucleus with a velocity *V* in a radius *R*. Hence, this current loop creates a magnetic moment $\vec{\mu} = I\vec{A}$ where $\vec{A}$ is a normal area vector. A schematic representation of the electron-nucleus system is shown in Fig. 1.3.

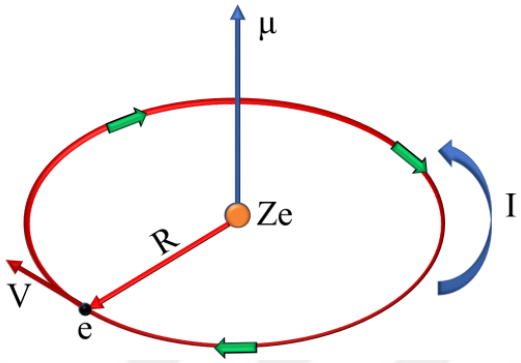

Figure 1.3. Magnetic moment produced by current loop (Akyol, 2011).

The current corresponding to the electron movement in a circular orbit around the nucleus of a simple hydrogen atom, is given by following relation,

$$I = \frac{eV}{2\pi R} \tag{1}$$

where *V* is the velocity of electron and *e* is the charge of electron. Hence, the magnetic dipole can be written as follows.

$$|\vec{\mu}| = \left|I\vec{A}\right| = \frac{eV}{2\pi R}\pi R^2\left|\hat{A}\right| \tag{2}$$

If it is expressed the magnetic dipole with orbital angular momentum, it is obtained by following equation.

$$\vec{L} = m\vec{V} \times \vec{R} \tag{3}$$

$$|\vec{\mu}| = \frac{1}{2} eVR|\hat{A}| = \frac{e}{2m_e}|\vec{L}| = \gamma|\vec{L}| \tag{4}$$

where γ is gyromagnetic ratio. Until now, we thought electrons only had orbital angular momentum, but electrons also have a spin angular momentum that can be written with the operator $\hat{S}^2$.

$$\hat{S}^2\chi = \hbar^2 s(s+1)\chi \tag{5}$$

Quantized angular momentum is given as follows.

$$|\vec{S}| = \hbar|\sqrt{s(s+1)}| \tag{6}$$

Then, spin magnetic moment can be written as in equation (7);

$$|\mu_s| = \gamma|\vec{S}| = \gamma\hbar\sqrt{s(s+1)} \tag{7}$$

In addition, it can be written as ($\mu_B = {e\hbar}/{2m_e}$ of Bohr magneton $\gamma\hbar$. Therefore, the magnetic dipole originates from both the orbital and spin angular momentum can be written as follows;

$$|\mu_s| = \gamma|\vec{S}| = \mu_B\sqrt{s(s+1)} \tag{8}$$

$$|\mu_l| = \gamma|\vec{L}| = \mu_B\sqrt{l(l+1)} \tag{9}$$

It can be written as total contribution of orbital and spin angular momentum to magnetic dipole,

$$|\mu_j| = \gamma|\vec{J}| = \mu_B\sqrt{j(j+1)} \tag{10}$$

where *j* is the total angular momentum quantum number and is equal to the sum of the orbital angular momentum and spin angular momentum.

$$\vec{J} = \vec{L} + \vec{S} \tag{11}$$

1.2.1. Classification of magnetic materials

The magnetism in a material comes from the orbital movements of electrons, spin movements and how electrons interact with each other. The best way to understand magnetic material types is to define how the materials react to the magnetic field. All substances in nature show magnetic properties. In nature, magnetic materials are basically divided into five main groups which are diamagnetic, paramagnetic, ferromagnetic, antiferromagnetic and ferrimagnetic.

1.2.1.1. Diamagnetism

Diamagnetic materials are materials that do not have permanent magnetic dipoles. Therefore, when an external magnetic field is applied, the electrons in orbit interact with this magnetic field and their speed changes. They have a negative magnetic susceptibility, but when the field is removed, the magnetic susceptibility disappears and hence no magnetization occurs. An electromotive force is induced when the current is changed in a circular wire. The electromotive force, by its nature, tries to return this current to its previous state. Electrons can be thought of as currents passing through a circular wire. When an external magnetic field is applied, a magnetization occurs against the field. In this case, the applied magnetic field is pushed by the material (Akyol, 2011). Materials with this type of structural dynamics are called "diamagnetic" materials. Materials of diamagnetic nature are examples such as water, DNA, petroleum and many plastics. An applied magnetic field induces a small negative magnetic moment on diamagnetic atoms, and this magnetic moment is proportional to the magnitude of the applied field. The schematic representation of the magnetic moments of the diamagnetic materials under the field and without field is shown in Figure 1.4.

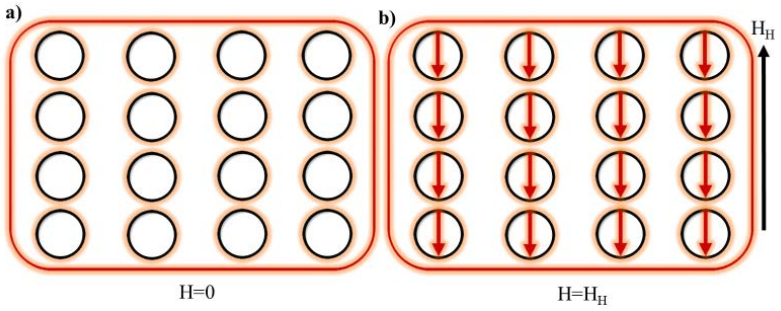

Figure 1.4. Arrangement of the magnetic moments of a diamagnetic material a) external magnetic field is not applied and b) external magnetic field is applied.

Figure 1.5 shows how a diamagnetic material responds to an applied magnetic field. As seen in Figure 1.5, a diamagnetic material creates an opposite directional magnetization on the applied area. However, as the magnetic field applied from the outside is increased, the magnetization of a diamagnetic material appears to increase in the opposite direction. In other words, when a diamagnetic material is exposed to a magnetic field, it creates a magnetization inversely to the field. When the magnetic field is removed, the net magnetic moment becomes zero. Based on these graphs, it is seen that magnetic susceptibility in a diamagnetic material represents the mathematical relationship given by $\chi = M/H$ where M is magnetization and H is applied magnetic field.

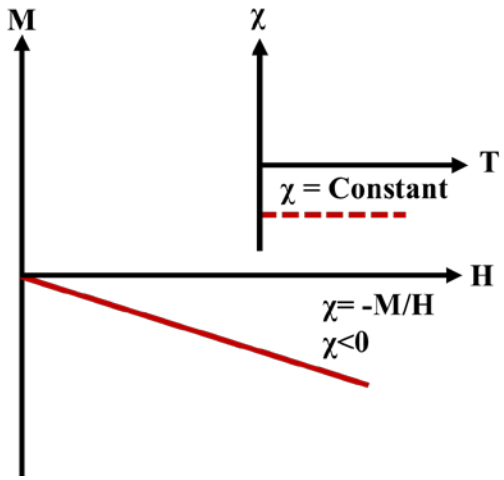

Figure 1.5. *M-H* plot of a diamagnetic material.

1.2.1.2. Paramagnetism

In paramagnetic materials, it is known that neighboring atoms separated from each other do not interact and each atom has a net magnetic moment even when there is no applied field.

This is due to the fact that there are unpaired electrons in the orbits of atoms or molecules. When no external field is applied, the magnetic moments are randomly directed in the lattice, and because of the thermal fluctuation, these magnetic moments change their orientation continuously. Therefore, net magnetic moments are approximately zero. When an external magnetic field is applied, the spins are lined up in the direction of the field. Spins remain predominantly random and some magnetic moments are lined up in the field direction, but have a small net magnetization in the direction of the applied magnetic field. Figure 1.6a-b show the orientation of the magnetic moments of atoms before and after applying a magnetic field to a paramagnetic material, respectively. Figure 1.6b is the latest state that can be taken by the influence of a strong field applied externally to a paramagnetic material and is called the saturation state of magnetization. If the applied field is weak, such an orientation may not be complete in the material (Akyol, 2011).

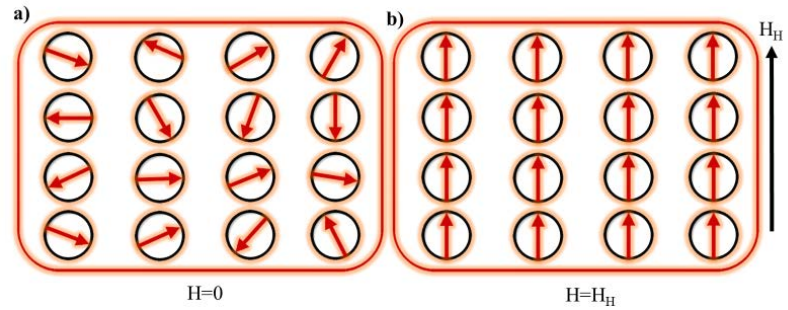

Figure 1.6. Arrangement of the magnetic moments of a paramagnetic material a) external magnetic field is not applied and b) external magnetic field is applied.

Figure 1.7 shows the reaction of a paramagnetic material to the field when a magnetic field is applied from the outside. As seen in Figure 1.7, when an external magnetic field is applied to a paramagnetic material, the magnetic moments, which are irregular in the material, begin to be arranged in the same direction as the field increases. Therefore, the magnetic moments create a magnetization in the same direction as the magnetic field applied from the outside. As the applied magnetic field increases, the total magnetization of the material increases linearly. This is because the applied magnetic field regulates more magnetic moment. If the applied field is large enough, magnetization begins to change, that is, material reaches saturation magnetization. However, if the applied field has small values, the $M = \chi H$ relationship begins to play a role.

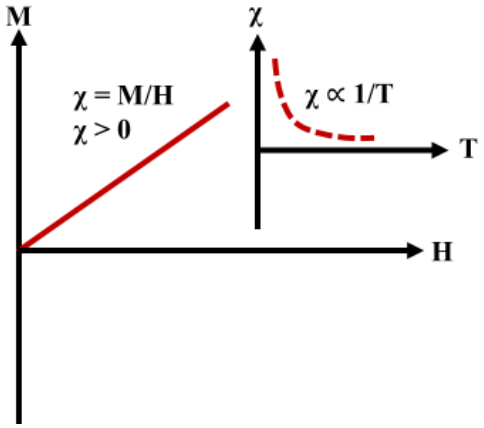

Figure 1.7. *M-H* plot of a paramagnetic material.

1.2.1.3. Ferromagnetism

Unlike paramagnetic materials, in a ferromagnetic material, all atoms are of the same type and each atom has a clear magnetic moment. Ferromagnetic materials are materials with spin coupling between orbital electrons. This spin coupling causes the long distance magnetic order as a result of the exchange energy that provides spin sorting. All ferromagnetic materials lose their ferromagnetic behavior at a certain temperature due to thermal fluctuations. This temperature is called Curie temperature (T_C). Ferromagnetic materials are systems with atomic scale long distance order since they have unpaired electron spins lined up parallel to each other in regions known as domains. Unpaired electrons in the *d*-shell of transition metals cause spin coupling. The domains have a strong internal magnetic field and can exist even when there is no applied magnetic field. For example, in a bulk material, since the domains will be randomly oriented relative to each other, the material will not gain magnetization without an applied field. However, since an external field is applied, the domains in a ferromagnetic material will begin to line up and the material will gain magnetization. Figure 1.8a shows the domains in a bulk ferromagnetic material and the sequence of magnetic moments before external field is applied. In Figure 1.8b, when a magnetic field is applied to the material from the outside, the magnetic moments in the domains are lined up according to this field and the magnetization of the material increases in the direction of the applied field. This magnetization is about three to four times more than paramagnetic materials.

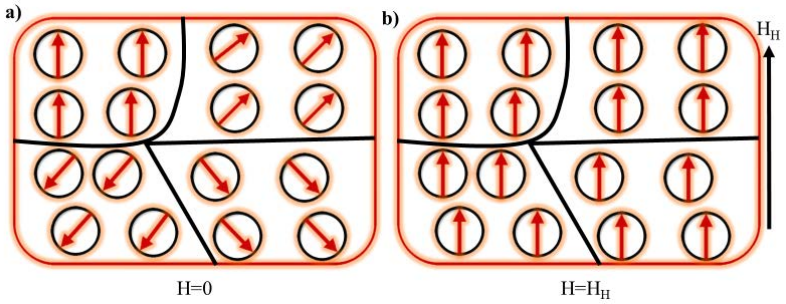

Figure 1.8. Arrangement of the magnetic moments of a ferromagnetic material a) external magnetic field is not applied and b) external magnetic field is applied.

The main feature of any ferromagnetic material is that it shows an irreversible and nonlinear magnetization in the field-dependent direction when a magnetic field is applied from the outside. This reaction is summarized by the hysteresis loop. In Figure 1.9a, when a magnetic field is applied from outside to a ferromagnetic material, the reaction against the field is shown in Figure 1.9b(c) of the representative hysteresis curve of a hard (soft) ferromagnetic material (Coey, 2010).

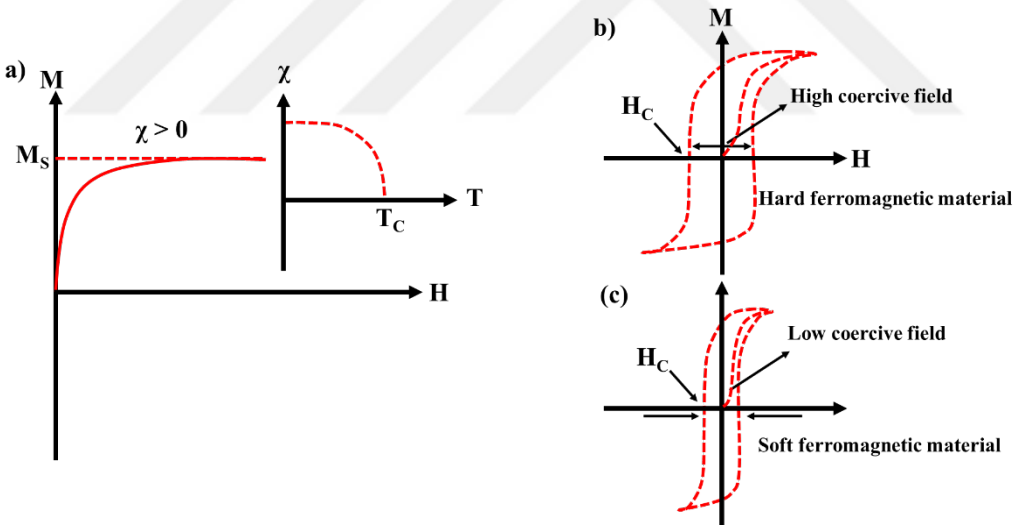

Figure 1.9. a) *M-H* plot of a ferromagnetic material, hysteresis curves of b) hard and c) soft ferromagnetic material.

As seen in Figure 1.9a, when a magnetic field is applied on a ferromagnetic material from outside, the atoms in the material begin to respond and regulate rapidly in the field direction. It increases the total magnetization of the material in a short time. When the applied field is increased, the magnetization reaches saturation magnetization (M_S) value (Coey, 2010). Figure 1.9b shows that hard ferromagnetic materials have a large coercive field. This is

suitable for permanent/natural magnets because they remain magnetized when a sufficient fieldis applied to saturate the magnetization. Figure 1.9c shows that soft ferromagnetic materials have a small coercive field. These materials are temporary magnets and immediately lose their magnetization as soon as the applied field is removed. The applied field is used to reveal the spontaneous/natural ferromagnetic order that already exists on the scale of microscopic domains (Coey, 2010).

1.2.1.4. Antiferromagnetism

Like ferromagnetic materials, atoms are the same type in antiferromagnetic materials and have a clear magnetic moment. Unlike ferromagnetic materials, however, neighboring magnetic moments have an anti-parallel sequence to one another. Therefore, the nearest neighboring magnetic moments have a dynamic that destroys each other. The fact that magnetic moment orientations of an antiferromagnetic material are anti-parallel is due to the super exchange interaction (Coey, 2010). Antiferromagnetic materials are systems with long-range order and have a small positive magnetic sensitivity due to these anti-parallel-aligned spins. An applied field tends to sort the spins, which is larger than the diamagnetic characteristic of electron orbits. Figure 1.10 shows the orientation of the magnetic moments of the atoms before and after applying an external magnetic field.

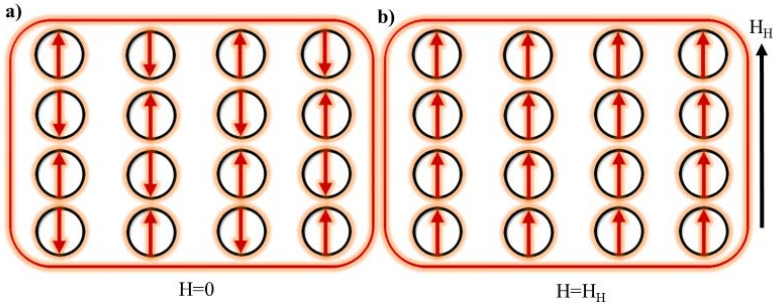

Figure 1.10. Arrangement of the magnetic moments of an antiferromagnetic material a) external magnetic field is not applied and b) external magnetic field is applied.

Considering that the magnetic moments in an antiferromagnetic material are equally strong, how these magnetic moments destroy each other can be seen in Figure 1.10a. As seen in Figure 1.10b, when a strong magnetic field is applied to this material, atomic moments tend towards the field.

As shown in Figure 1.11, when a magnetic field is applied from outside, a magnetization value occurs in the same direction as the applied field since the opposite oriented magnetic moments in the material are arranged in the same direction with the field. However, it can be seen that as the applied field increases, total magnetization increases. When a sufficiently high magnetic field is applied, magnetization of the material is expected to reach saturation value. In Figure 1.14, as the temperature increases in an antiferromagnetic material, the magnetization increases and then it reaches its maximum value at Neel transition temperature (T_N). After this temperature, the material begins to exhibit paramagnetic behavior. Here the paramagnetic zone complies with Curie-Weiss law. The details on Curie-Weiss law will be discussed in Section 1.2.2.

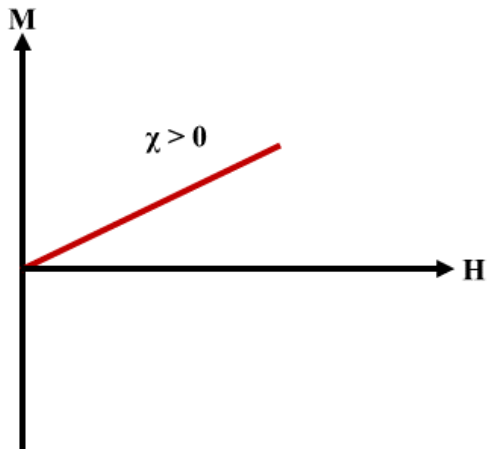

Figure 1.11. *M-H* plot of an antiferromagnetic material.

1.2.1.5. Ferrimagnetism

Ferrimagnetism is similar to antiferromagnetism as it has an anti-parallel magnetic moment arrangement. However, their magnetic moments have different magnitudes. Therefore, the magnetic moments of ferrimagnetic materials do not destroy each other and have a clear magnetization. However, saturation magnetization is lower than ferromagnetic materials. Magnetization of ferrimagnetic materials is similar to ferromagnetism in terms of hysteresis behavior. Ferrimagnetic materials usually consist of two different types of atoms and appear in complex crystal structures. The super-exchange interaction between magnetic moments causes the anti-parallel allignment of the magnetic moments. However, the magnetic orientation of some regions within the crystal structure may be opposite to the general orientation of the crystal structure. Therefore, total magnetization decreases in these regions.

Figure 1.12 shows the arrangement of magnetic moments before a field is not applied to a ferrimagnetic material and after a sufficiently high field is applied from the outside.

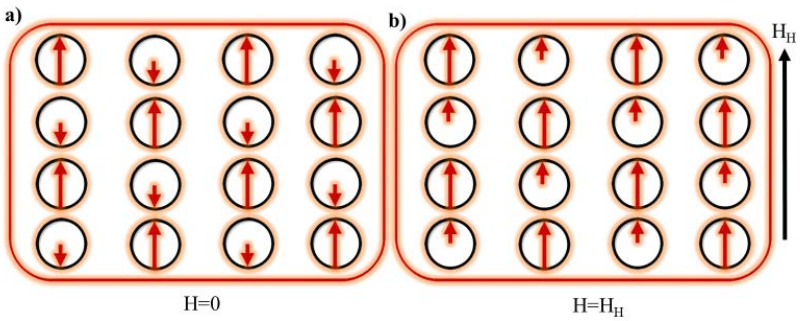

Figure 1.12. Arrangement of the magnetic moments of a ferrimagnetic material a) external magnetic field is not applied and b) external magnetic field is applied.

As shown in Figure 1.13, when an external field is applied, the response of a ferromagnetic material to the field is very similar to the response of a ferromagnetic material. However, the saturation magnetization of a ferrimagnetic material is lower compared to a ferromagnetic material. The magnetic field applied from the outside starts to direct the magnetic moments in the material in the same direction as the field. If the field is further increased, the arrangement of the magnetic moments becomes more orderly and the total magnetization of the material increases. If the field is increased more, the total magnetization reaches saturation value since there will be no more atoms to be regulated in the material.

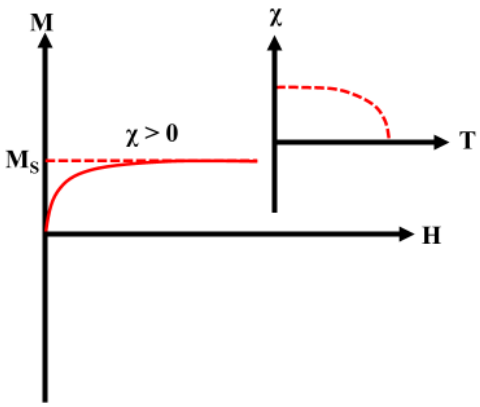

Figure 1.13. *M-H* plot of a ferrimagnetic material.

1.2.2. Curie temperature and Curie-Weiss law

Ferromagnetic materials lose their ferromagnetic properties above a critical temperature called Curie temperature, T_c, and go into a paramagnetic state (see Fig. 1.14). When the temperature is increased, the thermal vibrations of ions rise to a very high level and this temperature increase disrupts the ferromagnetic orientation of the magnetic dipoles of the material. In this case, the material begins to show a paramagnetic behavior. Magnetic susceptibility (χ) of material indicates how much it reacts to the external magnetic field and is expressed by following equation.

$$\chi = \frac{M}{H} = \frac{C}{T} \tag{12}$$

where *C* is Curie constant. The magnetization of a material is defined as the magnetic moment per unit volume or per unit mass of and depends on the individual magnetic dipole of the atoms in the material and their interactions with each other. This mathematical expression is invalid for the phenomenon of ferromagnetism because the net magnetic moments of ferromagnetic materials interact with each other. Due to this interaction, each magnetic moment in a ferromagnetic material is influenced by the average molecular field formed by other magnetic moments. This was first described by Weiss (Weiss, 1906) with the molecular field theory. Since the material passes to the paramagnetic state above the curie temperature, the expression takes its form in equation (13).

$$\chi = \frac{C}{T - \theta} \tag{13}$$

This is called Curie-Weiss law (Weiss, 1906). Here, θ is a temperature constant and it takes negative, positive and zero values in antiferromagnetic, ferro/ferri-magnetic and paramagnetic materials, respectively.

- If θ = 0, Curie law (equation 12) takes over.
- If θ > 0, the material is ferromagnetic below Curie critical temperature, T_c.
- If θ <0, the material is antiferromagnetic below the Neel critical temperature, T_N.

Figure 1.14 shows the material's transition at critical Neel and Curie temperatures. Curie temperature is a characteristic of ferromagnetic materials. Neel temperature is a characteristic of antiferromagnetic materials. A heat treated ferromagnetic (antiferromagnetic) material shows paramagnetic properties above the Curie (Neel) temperature (Coey, 2010).

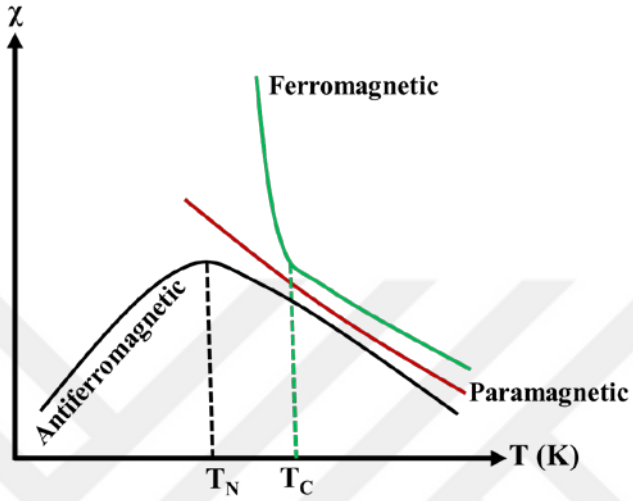

Figure 1.14. Magnetic transition of antiferromagnetic and ferromagnetic materials at critical Neel and Curie temperatures.

1.2.3. Magnetic domains

The atoms of ferromagnetic and ferrimagnetic materials can be thought of as small magnets with an N-pole and an S-pole. These atomic magnets or dipoles interact with the nearest neighboring dipoles and form magnetic zones in the material, arranged in separate groups in the same direction as their magnetic axes. There are millions of these domains in an unmagnetized piece of iron (Fe), but each domain points in a different direction before the piece of iron is magnetized. When the piece of iron is exposed to a magnetic field from the outside, the magnetic moments act like a small compass needle and rotate until they are arranged in the same direction as the field. Then one end of these magnetic moments is lined up to indicate the N-pole and the other end to the S-pole.

1.2.4. Multi-domain structures and Hysteresis loop

The main feature of ferromagnetic and ferrimagnetic materials is that they show a complex change in their magnetization when exposed to a magnetic field. This change is best explained by the hysteresis loop. Much can be learned about a magnetic material by analyzing the

hysteresis loop. This behavior against the magnetic field results from the magnetic materials being formed from magnetic regions. The hysteresis loop provides important information about the saturation magnetization (M_s), remenant magnetization (M_r), coercive field (H_c) of a magnetic material and whether the material is magnetically hard or soft. Figure 1.15 shows an example of a hysteresis loop of a magnetic material consisting of a multi-domain structure.

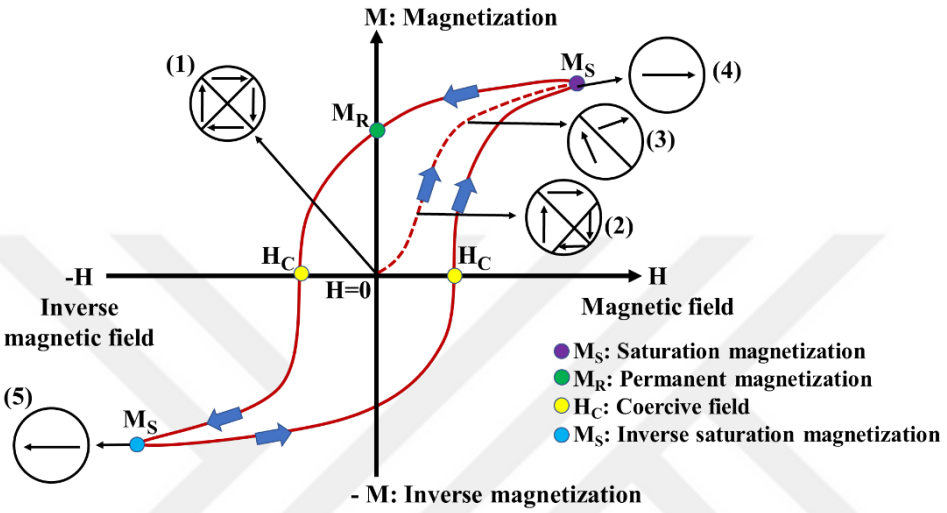

Figure 1.15. Hysteresis loop of a multi-domain magnetic material.

Ferromagnetic and ferrimagnetic materials are materials that can have net magnetization even when there is no external magnetic field. When exposed to an external magnetic field, their magnetization increases rapidly and reaches a saturation value. This saturation value is called saturation magnetization and its unit is emu. When the applied field is removed, the material has a remenant magnetization. When the field is applied in the opposite direction, the magnetization is forced to be zero at the coercive field value. The coercive field gives information about how easy or difficult to magnetize a material and is the half width of the hysteresis loop where magnetization passes from zero in the positive and negative direction of the applied field. Therefore, the main points in the hysteresis loop are M_s, M_r and H_c. Materials with $H_c \geq 100$ Oe (10000 A/m) are called “hard magnetic materials”. Materials with $H_c \leq 100$ Oe (10000 A/m) are called “soft magnetic materials”. In hard magnetic materials, magnetic zones tend to not be easily regulated and zone walls do not move easily. Therefore, the material must have a strong magneto-crystalline anisotropy or alternatively they may have a “shape anisotropy” observed in nano-dimensions. When the field is increased in the opposite direction, the magnetic moments in the material have a direction in the opposite

direction and show a saturation magnetization in the opposite direction. This behavior is characterized by the hysteresis loop as shown in Figure 1.15.

1.2.5. Single domain structures and Superparamagnetism

When the nanoparticles with a multi-domain structure are exposed to an external magnetic field, the domains begin to head in the direction of the magnetic field and have a single domain consisting of a giant magnetic moment. This behavior is defined as superparamagnetism. When you go from macroscopic dimensions to nanoscale, surface/volume ratio increases and quantum mechanical effects become dominant. For this reason, when the nanoscale comes down, the materials begin to show different physical properties. The phenomenon of superparamagnetism is one of these features. The superparamagnetic effect can occur in materials made up of crystals of small dimensions. If the spins in a material alling in a single direction, it can be said that these materials consist of a single domain and its saturation magnetization is M_s.

It is the first time that Stoner and Wohlfarth (Stoner et al., 1948) showed the magnetization vactor rotates around an axis. Stoner and Wohlfarth argued that the response of affinity magnetization to the applied field was determined by shape, stress, crystal and exchange anisotropy. When the physical size of a magnetized particle is smaller, the domain boundary energy partially contributes to the total energy and becomes energetically unfavorable so that no domain boundary forms, eventually turning into a point structure. Then, the particle acts as a single domain and shows properties different from those of multi-domain particles with domain walls. Since superparamagnetic particles are of very small size, they have one or more “easy” axes and their energy is smaller than the energy of “hard” axes. Magnetic moments tend towards low energy regions, and the axis where magnetic moments tend to this direction is defined as 'easy axis'. In superparamagnetic materials, anisotropy energy can be defined as the energy required to change the direction of magnetization from one easy axis to another, and may result from many physical parameters such as spin interactions, particle shape, stress, and exchange anisotropy. The simplest case for this model is where uniaxial anisotropy exists. Uniaxial anisotropy is called the easy axis where the magnetic moment directs itself to minimize the energy. The particle shown in Figure 1.16 has uniaxial anisotropy and is exposed to a static field from the outside.

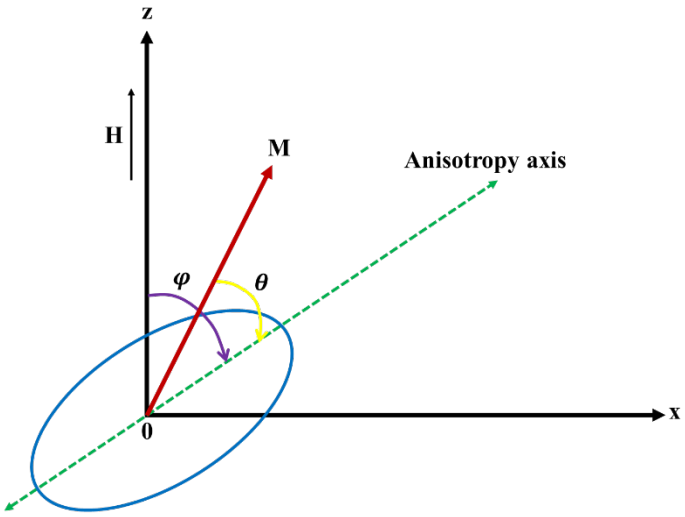

Figure 1.16. Single-domain particle and magnetization exposed to an external magnetic field.

In a critical radius, the particle does not thermodynamically generate domain walls. Here, anisotropy energy (KV) has a much greater value ($KV >> k_BT$) than thermal energy (k_BT), resulting in the phase rotation of a single domain. This requires the reverse cycle of magnetization with the rotation of the magnetic moment in the direction of the applied field. When there is no externally applied field, the preferred direction of the single-domain magnetic particle is determined by magnetic anisotropy. This orientation is shown as the anisotropy axis in Figure 1.17 (Willard, Kurihara, Carpenter, Calvin, & Harris, 2004). When the particle size falls below the single domain value, spins are more affected by thermal fluctuations ($KV << k_BT$) and the system exhibits superparamagnetic behavior (Leslie-Pelecky & Rieke, 1996).

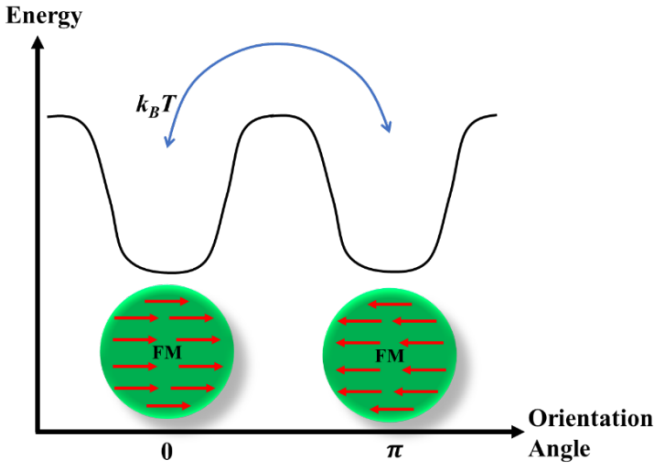

Figure 1.17. Comparison of magnetic anisotropy energy with thermal energy (k_BT) (Eisenmenger & Schuller, 2003).

Superparamagnetism is a time-dependent physical event. Anisotropy energy can be considered as the energy barrier necessary to direct magnetization in a certain direction. The probability of exceeding this energy barrier by thermal fluctuation is proportional to the Boltzmann factor ($e^{-(KV/k_BT)}$). When this happens, the particles exhibit superparamagnetic behavior, because thermal fluctuations cause the spins to be oriented in random directions, so that the magnetization direction changes between parallel and antiparallel orientations (Eisenmenger et al., 2003). If thermal energy is large enough to be compared to anisotropy energy barrier, Neel relaxation occurs and the magnetization vector can cross the energy barrier and jump from one easy axis to another. However, when the anisotropy energy is much larger than the thermal energy, the magnetization vector makes an oscillating motion around the easy axis that it is found with its thermal energy (Stoner et al., 1948, Umut, 2012). Since the transition of the thermal excitation and magnetization vector between different easy axes is a random event, the frequency of this transition occurs in a Neel relaxation time τ_N, which can be defined as an average time value between two passes. τ_N can be formulized as following relation (Jr., 1959);

$$\tau_N = \tau_0 e^{-(KV/k_BT)} \tag{14}$$

where τ_0 is a measure of the reversal time of particle magnetization, K is anisotropy constant, V is volume of particle, k_B is Boltzman constant and T is temperature. Equation 14 is called

the Neel-Arrhenius equation. It is in the range of 10^{-9}-10^{-11} s for particles exhibiting pure superparamagnetic behavior that do not interact. The temperature and size range in which superparamagnetic behavior can be observed varies according to the magnetization measurement technique. The t_m measurement time for a particular magnetization measurement method;

- If $t_m > \tau_N$, magnetization during the measurement changes the direction between the axes many times, making the mean time zero in vectorial and the particle shows superparamagnetic behavior.
- If $t_m < \tau_N$, it is driven into one of the axes that is easy to magnetize the particle throughout the measurement and the particle magnetization is “blocked”.
- If $t_m = \tau_N$, particles move from blocked state to superparamagnetic state, in which case a critical T_B blocking temperature can be defined.

If the measurement time t_m = 100 s and $\tau_0 = 10^{-9}$ is taken for a standard magnetization measurement, the T_B blocking temperature can be written as follows.

$$T_B = \frac{KV}{25k_B} \tag{15}$$

The size limitation is evident in the particles where superparamagnetic behavior is observed and it varies between different materials. Figure 1.18 shows coercive field as a function of particle size that superparamagnetic particles have single domain. Superparamagnetic particles exhibit ferromagnetic behavior under the blocking temperature. Above the blocking temperature, they act as paramagnets with very high susceptibility, as thermal energy is sufficient to rotate the particle moment. However, single-domain particles may have a higher blocking temperature than room temperature (Leslie-Pelecky & Rieke, 1996).

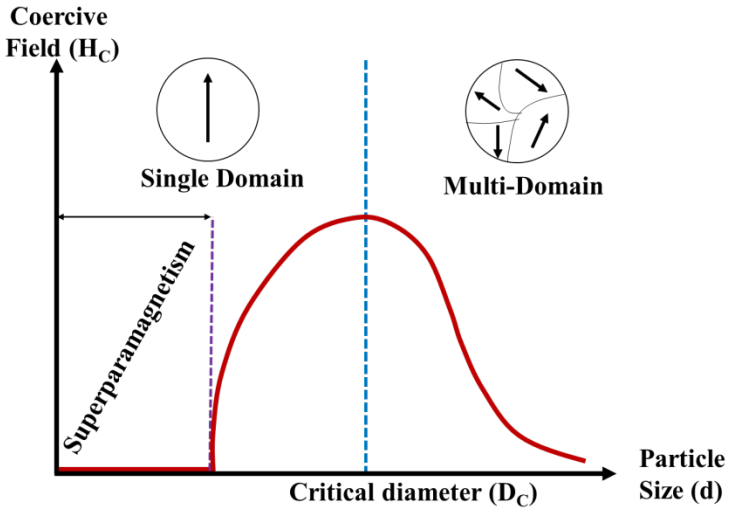

Figure 1.18. Change in domain structure and magnetic properties to particle size.

1.3. Cobalt chromite spinel structures

Cobalt chromites $CoCr_2O_4$ are known to have the normal spinel structure in which Co^{2+} ($3d^7$) divalent cations occupy tetrahedral places, in other words, tetrahedral oxygen coordination, Cr^{3+} ($3d^5$) trivalent cations occupy octahedral areas (Akyol et al., 2017; Ishibashi & Yasumi, 2007; Kamenskyi et al., 2013; Lawes et al., 2006; Tomiyasu, Fukunaga, & Suzuki, 2004). Figure 1.19 shows the electronic configuration of Co^{2+} divalent cations in A-site and Cr^{3+} trivalent cations in B-site of a spinel structure. They show paramagnetic to the collinear short-range ferrimagnetic (FiM) transition ($T_C \approx 95$ K) where it breaks the reverse symmetry to produce ferroelectricity due to its inverse interaction between a non-collective neighbor spins (Yang et al., 2012). Upon further lowering of the temperature, the short-range FiM sequence turns into a long-range, non-collinear spiral magnetic transition ($T_s \approx 28$ K). Therefore, the $CoCr_2O_4$ is due to the onset of the non-collinear spiral magnetic transition, the beginning of the short-range FiM transition due to the non-collinear spin structure (Choi et al., 2009). Below the spiral magnetic transition temperature, a locking transition occurs ($T_L \approx 14$ K).

The properties of magnetic materials such as magnetic saturation and remenant magnetization depend on the particle size and the particle shape due to surface anisotropy effects. Therefore, the synthesis techniques of magnetic materials play an important role in terms of both particle size and particle shape.

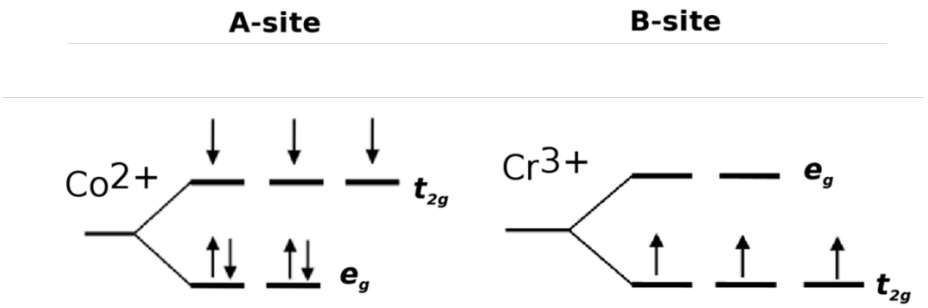

Figure 1.19. Electronic configurations of $CoCr_2O_4$ normal spinel compounds.

1.4. Cobalt ferrite spinel structures

An interesting aspect of spinel ferrite nanoparticles is their unique magnetic properties, since the magnetic response is controlled by particle size and shape. Although there are various spinel nanoparticle materials used in biomedicine and magnetic recording, a lot of research has been done to understand nanomagnetic ferrites. Cobalt ferrite ($CoFe_2O_4$) is widely used for magnetic recording applications and ferrofluids because of its unique magnetic properties with large first order magneto-crystalline anisotropy (K) constant compared to other spinel materials. $CoFe_2O_4$ materials have also been used as contrast agents in Magnetic Resonance Imaging (MRI) (Akyol, Adanur, Ayaş, Karadağ, & Ekicibil, 2018; Goldman, 1999; Kuncser et al., 2003; X.-H. Li et al., 2010).

For practical applications, it is desirable for the materials to have larger magnetic anisotropy and larger magnetic moments, reducing the particle sizes to the nano-meter scale. Changing the cations in the A/B sites can alter the magnetic interactions like antiferromagnetic A-B and exchange interaction B-B. Therefore, research attention is mainly focused on improving the magnetic properties of $CoFe_2O_4$ by substituting several cations such as Cr, Zn, Ni, Mn in regions A and B. In order to reduce antiferromagnetic interactions between *d-d* (Co^{2+}-Fe^{3+}) orbital electrons in the spinel structure, the non-transition metal (*p*-orbital) spinel structure can be incorporated into one of its locations. Thus, *p-d* exchange interaction can increase effective magnetization across the entire structure (Akyol et al., 2018). Figure 1.20 shows electronic configuration of $CoFe_2O_4$ in A and B-sites of Co^{2+} and Fe^{3+} cations. Since $CoFe_2O_4$ is inverse spinel structure, half of Fe^{3+} ions occupy A-site and other half occupy B-site.

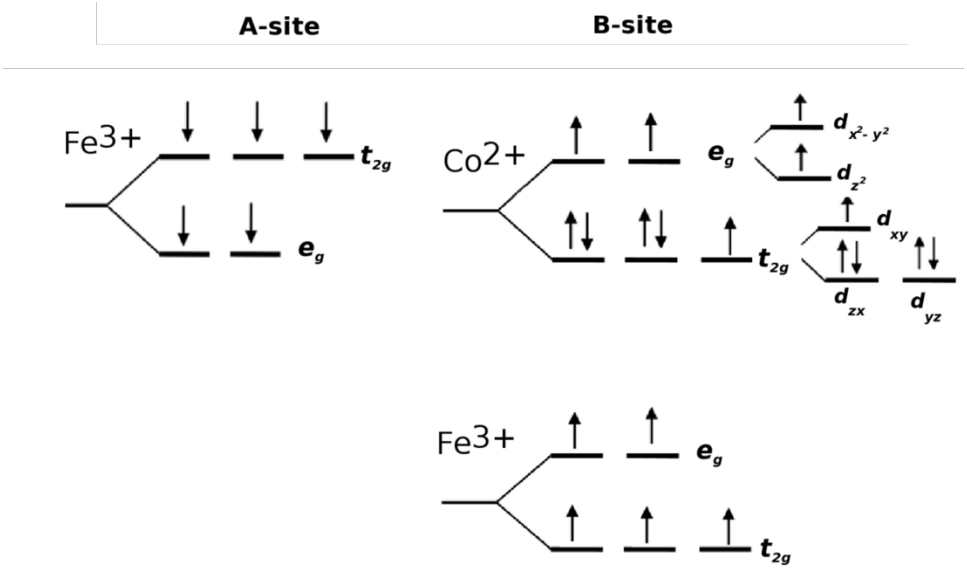

Figure 1.20. Electronic configurations of $CoFe_2O_4$ inverse spinel compounds.

1.5. Thesis objectives

In this thesis, we have first optimized some physical properties of Co-based spinel multiferroic material for practical applications working around room temperature. To do this, Fe^{3+} ions have substituted by the Cr^{3+} ions in $CoCr_2O_4$ spinel structure. Based on magnetic transition temperature and maximum magnetic entropy change values, we have continued to study on the effect of Ho^{3+} ions as a rare earth on the structural, magnetic and magnetocaloric properties of $CoCrFeO_4$ spinel materials.

2. LITERATURE REVIEW

Zhang et al. produced $CoCr_{2-x}Fe_xO_4$ samples (where *x* varies between 0.0 and 1.0 with a step of 0.2) by solid-state reaction method in air and they studied the compensation effect and magnetostriction. They found that the lattice parameter (*a*) increases gradually upon Fe-doping, having a sharp increase at *x*=0.10 compared to other concentrations. It was noticed that the Fe^{3+} ion dominantly distributed on the A site for the high doping concentrations, except x = 0-0.1. They worked on the magnetic properties of samples by performing the temperature and field dependences of magnetization and they found that the Curie temperature increases regularly upon Fe-doping. The magnetization dependence was measured under 5T and it displayed the minimum value at x=0.1, meaning that there exists the composition compensation effect. The M-H curves showed that coercivity (H_c) increases from both sides of the compensation point (x=0.1), however it dropped to 2986 Oe at this point as a minimum value. From the ZFC-FC curves and a negative magnetization was observed on the FC curve under 1kOe at ~40 K. The magnetostriction effect having a maximum value of the strain as 280 ppm was observed for x=0.4 at 5K (Zhang et al., 2013).

Li et al. fabricated $CoCr_2O_4$ polycrystalline ceramics by sol-gel method. They worked on the negative magnetization and exchange bias effect on $Co(Cr_{1-x}Ho_x)_2O_4$ where *x* varies between 0.00 and 0.12 with a step of 0.02. No significant change was observed for lattice parameters (*a*) and unit cell volumes (*V*). Reliability factors ($R_p,\ R_{wp}\ and\ \mathcal{X}^2$) varry between 2.42% – 2.95% (2.85% for pure sample), 3.24% – 4.31% (4.00% for pure sample) and 1.150 – 2.189 (1.921 for pure sample), respectively. It was determined that transition temperature ($T_C(K)$) was increased (from 94 K up to 130 K) upon all doping concentrations. At an applied field of 500 Oe, both field cooling (FC) and zero-field cooling (ZFC) were carried out for the investigation of magnetic properties. The magnetic anisotropy was illustrated by the irreversibility of ZFC and FC processes and it provides conditions for the negative magnetization (NM) phenomenon. It was observed that the FC magnetization decreased continuously and significant NM was observed below T_{comp} for 0.06% Ho doping concentration. The $Co(Cr_{0.90}Ho_{0.10})_2O_4$ sample was chosen for further investigations of magnetic properties due to having the most apparent NM phenomenon. Two symmetrical curves were observed, implying that the net magnetic moments are anti-parallel to the

external magnetic field below T_{comp}. It was reported that magnetization was increased while magnetic field increases from 50 Oe to 500 Oe (C. L. Li et al., 2018).

Panneer Muthuselvam et al. synthesized $CoFe_{2-x}Ho_xO_4$ ferrites where *x*=0.05 by mechanical alloying and they studied the influence of annealing temperature (600-1200°C) on the structural and magnetic properties of samples. Grain sizes (*D*) and lattice parameters (a) were found to be as follows; 50 nm and 8.3745 Å; 59 nm and 8.3750; 64 nm and 8.3870 Å; 67 nm and 8.4064 Å; 76 nm and 8.3783 Å; 90 nm and 8.380 Å for annealing temperature (T_{AN}) of 950 °C; 1000 °C; 1050 °C; 1100 °C; 1150 °C; 1200 °C, respectively. As can be seen from results, the more increasing the annealing temperature, the more increased value of both a and *D*. Saturation magnetization (M_S), the remanence ratio (M_R/M_S), and coercivity (H_c) parameters of samples for different T_{AN} values (950 °C, 1000 °C, 1050 °C, 1100 °C, 1150 °C) were tabulated as follows; 1.71062 $\mu_B/f.u$, 0.436, 941; 2.43477 $\mu_B/f.u$, 0.362, 893; 2.75857 $\mu_B/f.u$, 0.347, 902; 2.71385 $\mu_B/f.u$, 0.242, 628; 2.59645 $\mu_B/f.u$, 0.210, 634, respectively. No data of these three parameters were reported for $T_{AN} = 1200$ ℃. From the data reported in the study, it can be seen that both Ho-doping and annealing temperature (T_{AN}) had a positive effect on both magnetic and structural properties of CFHO ferrites (Panneer Muthuselvam & Bhowmik, 2010).

Panneer Muthuselvam et al. produced $CoFe_{0.95}Ho_{0.05}O_4$ ferrites via mechanical alloying and studied the influence of annealing temperature (600-1200 °C) on the electrical properties of samples. They coded the samples according to the annealing temperature (T_{AN}) where $T_{AN} = 600$°C, $CoFe_{0.95}Ho_{0.05}O_4$ sample was named as S60 and for others; $T_{AN} = 800$°C, S80; $T_{AN} = 950$°C, S95; $T_{AN} = 1000$°C, S100; $T_{AN} = 1050$°C, S105; $T_{AN} = 1100$°C, S110; $T_{AN} = 1150$°C, S115; $T_{AN} = 1200$°C, S120. In the study, they also focused on Ac conductivity of samples in different frequencies (1 Hz – 3 MHz) at different temperatures (303-525 K). Activation energies (E_a) at different frequencies (0 Hz, 1 kHz, 50 kHz and 500 kHz) of the CFHO ferrites (S80, S95, S100, S105, S110 and S115) were found as 0.62, 0.60, 0.52 and 0.32 eV; 0.60, 0.59, 0.47 and 0.25 eV; 0.59, 0.59, 0.44 and 0.23 eV; 0.64, 0.63, 0.51 and 0.33 eV; 0.62, 0.60, 0.45 and 0.32 eV; 0.61, 0.56, 0.48 and 0.31 eV, respectively. From the data obtained, it can be concluded that E_a can be altered via T_{AN}. Electrical conductivities (σ) of above mentioned ferrites (S80-S110) at 303 and 523 K were as follows; 0.9248 $10^{-10} S/cm$, –; 7.4870 $10^{-10} S/cm$, 13.002 $10^{-6} S/cm$; 0.1983 $10^{-10} S/cm$, 0.319 $10^{-6} S/$

cm; 0.6154 $10^{-10}S/cm$, 1.881 $10^{-6}S/cm$; 1.5200 $10^{-10}S/cm$, 3.691 $10^{-6}S/cm$; 2.6230 $10^{-10}S/cm$, 4.990 $10^{-6}S/cm$, respectively. It was noticed that the conductivity was improved about 10^4 times, implying that the temperature has a significant effect on electrical properties of ferrites including the conductivity (Muthuselvam & Bhowmik, 2010).

Kamala Bharathi et al. fabricated pure, Sm- and Ho-doped nickel ferrites ($NiFe_2O_4$, $NiFe_{1.925}Sm_{0.075}O_4$ and $NiFe_{1.925}Ho_{0.075}O_4$) via solid-state chemical reaction. They studied the effect of doping on the structural, magnetic, dc electrical conductivity, ferromagnetic, ferroelectric, and dielectric properties of the samples. They used for their samples' code as NFO, NFSO and NFHO for $NiFe_2O_4$, $NiFe_{1.925}Sm_{0.075}O_4$ and $NiFe_{1.925}Ho_{0.075}O_4$, respectively. A slight increase in the lattice constant (a) of NFO (8.335 Å) upon doping was observed and were calculated as 8.348 Å and 8.346 Å for NFSO and NFHO, respectively. A decrease in the saturation magnetization compared to NFO (49.8 emu/g) with both doping Ho and Sm elements, and they reported as 42.5 emu/g and 45 emu/g for NFSO and NFHO, respectively. Curie temperature of ferrites were determined as $T_c = 853, 839$ and $812\ K$ for NFO, NFSO and NFHO, respectively. It can be seen that T_c values decreases upon doping Ho and Sm. At room temperature, the ferroelectricity in both Ho and Sm doped nickel ferrites was confirmed by the ferroelectric hysteresis loop measurements. 0.28 and 0.32 $\mu C/cm^2$ values of remenant polarization were reported for NFSO and NFHO, respectively. The magnetocapacitance of NFSO and NFHO were obtained as –1.8% and –1.2% for a field of 3200 Oe, whereas there was no magnetocapacitance of NFO. At 300 K, dc electrical conductivity (σ) of NFO, NFSO and NFHO were found as 9.8×10^{-9}, 3.4×10^{-10} and $3.1 \times 10^{-10}\ \Omega^{-1}cm^{-1}$, respectively. It can be said that conductivity decreased upon doping Ho and Sm (Bharathi, Markandeyulu, & Ramana, 2011).

Osial et al. synthesized undoped and Ho-doped SuperParamagnetic Iron Oxide Nanoparticles (SPIONs), Fe_3O_4 nanoferrites, by co-precipitation route. They studied the effect of Ho-doping concentrations (1%, 2.5%, 5%, 7.5% and 10%) on the characterization of nanoferrites. It was found that undoped, 1% and 2.5% Ho-doped nanoferrites had a spherical shape ~10-15 nm, however, further doping concentration led to irregular growth of crystals having a diameter of about threefold. It was reported that crystallite size of Ho-doped (up to 5%) SPIONs was increased up to 19 nm compared to that of pristine one (10 nm). The saturation magnetization was found to be 83 emu/g for the pure Fe_3O_4 whereas it decreased to 65 emu/g upon

increasing temperature from 100 to 300 K. However, only at 1% Ho-doped nanoferrites, M_s value was increased (slightly), for other doping concentrations, all M_s values were decreased at both 100 and 300 K. The low coercive field was also observed for the 2.5% and 5% doping, whereas H_c increased for 7.5% and 10% Ho-dopings. It was noticed that the best characteristics were at 2.5% Ho-doped SPIONs, and 1-2.5% Ho-doped SPIONs showed superparamagnetic behavior at room temperature (Zhang et al., 2013).

Shirsath et al. produced Manganese Ferrite ($MnFe_2O_4$) via self-ignited sol–gel method. They studied the effect of Ho-doping at different concentrations on the magnetic, structural and electrical properties of $MnFe_2O_4$ nanoparticles. It was reported that Ho-doping had a positive effect on the both electrical and magnetic properties. Lattice constant was calculated as 8.491 Å, 8.498 Å, 8.507 Å and 8.511 Å for undoped $MnFe_2O_4$ and for Ho-doped $MnFe_2O_4$ at 0.05%, 0.10% and 0.15%, respectively. Crystallite size was tabulated as 6 nm, 6 nm, 9 nm and 9 nm for Ho-doped $MnFe_2O_4$ at 0.00%, 0.05%, 0.10% and 0.15%, respectively. At room temperature, for 0.00% and 0.15% Ho-doped $MnFe_2O_4$, the remanence ratios were calculated as 0.31 and 0.60; remanence and saturation magnetization were found as 16.70 emu/g, 42.78 emu/g and 54.57 emu/g, 71.60 emu/g; coercive fields were noted as 172 Oe and 766 Oe, respectively. For electrical measurements of undoped and Ho-doped $MnFe_2O_4$; they observed a decrease in dielectric constant while observing an increase in both resistivity and the activation energy for electric conduction in the paramagnetic region (E_p) and ferrimagnetic region (E_f). As can be seen from calculations and results, Ho-doping influences favorably the electrical and magnetic characteristics of $MnFe_2O_4$ (Shirsath, Mane, Yasukawa, Liu, & Morisako, 2014).

Karimunnesa et al. fabricated single-phase cubic spinel structured undoped and Ho-doped $CoFe_2O_4$ (CFO) samples via standard solid-state reaction technique at different concentrations. In their work, the effect of Ho-doping on the structural, magnetic and transport properties were investigated. Lattice constants were found as 8.360 Å, 8.371 Å, 8.380 Å, 8.398 Å and 8.416 Å for 0.00%, 0.05%, 0.10%, 0.15% and 0.20% Ho-doped $CoFe_2O_4$ ferrites, respectively, implying that unit cell expanded. Grain sizes also increased (from 27 to 75 μm) with the Ho-doping, meaning that the doping had a significant effect on the grain growth. The saturation magnetization ($M_s = 47.69$ emu/g for $x = 0.00$ and 31.31 emu/g for $x = 0.20$) and Curie temperature

(T_c = 465 ℃ for x = 0.00 and 350 ℃ for x = 0.20) were decreased after Ho-doping. Coercivity values of all CFHO samples were increased compared to that of pristine one (CFO). Electrical resistivity was found to be decreased via Ho-doping except for x = 0.20, while the dielectric constant values of CFHO ferrites was found to be improved for all concentrations. As can be from results, Ho-doping had an important role to alter the characteristics (Karimunnesa et al., 2018).

Yousaf et al. synthesized both some rare earth (RE) metals (including Ho) doped and undoped Manganese Zinc (MnZn) spinel nanoferrites by sol gel combustion approach at low sintering temperature. They investigated the effects of RE metal doping on optical, structural, conductive and magnetic properties of RE's doping on the MnZn. For undoped MnZn, they obtained crystallite size and lattice parameter as 32.41 nm and 8.3690 Å, respectively, where they are noted as 26.97 nm and 8.4577 Å for Ho-doped MnZn, respectively. As seen from the structural calculations, a decrease was occurred after Ho-doping. The ratio of remanence and saturation magnetization between Ho-doped and undoped MnZn were found as 0.267 where M_r and M_s were tabulated as 2.83 emu/g and 14.76 emu/g for undoped MnZn and 7.04 emu/g and 26.36 emu/g for Ho-doped MnZn, respectively. A decrease in coercivity was observed from 28.80 Oe to 10.71 Oe upon Ho-doping. An improvement was obtained for optical properties of Ho-doped MnZn that the bandgap energy $E_g = 1.682\ eV$ increased from 1.652 eV (for undoped MnZn), Lastly, from the absorbance curve, it is seen that Ho-doped MnZn has a better characteristics from that of pristine one(Yousaf, Akhtar, Wang, & Noor, 2020).

3. MATERIALS AND METHODS

Solid-state reaction method and sol-gel method are the most preferred material synthesis techniques in the preparation of spinel compounds. The common goal in the methods to be selected in accordance with the intended use of the material is to obtain homogeneous samples in the desired stoichiometry with a small particle size.

In this chapter, the preparation procedures of $Co(Cr_{1-x}Fe_x)_2O_4$ ($0.0 \leq x \leq 1.0$) and Ho-substituted $CoCrFeO_4$ spinel compounds within the scope of the thesis and the measurement systems used to examine the structural, magnetic and magnetocaloric properties of the materials will be given in detail.

3.1. Material production by Sol-Gel method

The sol-gel method is based on the molecular dissolution of the starting inorganic compounds such as metal salts, nitrates, hydroxides and oxides prepared in appropriate stoichiometric ratios in a liquid. In this method, the product with a very homogeneous distribution can be obtained due to the dissolution of chemicals in solution form on a molecular basis in the liquid. The name sol-gel comes from the abbreviations of the words solution-gelation. "Left" is the name given to the solution in liquid suspension so that the starting inorganic compounds show homogeneous distribution. Since the intermolecular Van der Waals and electrical propulsion forces are more effective than the gravitational force, the materials that make up the left do not collapse to the bottom. Thus, if the molecule expands in solution and reaches a large size, this substance is called “gel”.

Sol-gel method is a preferred method because of the following features:

1. Due to the use of liquid solution states of the substances, a highly homogeneous and pure material can be obtained at the molecular level.
2. Thanks to its low preparation temperatures, it enables the development of ceramics that cannot be prepared normally by eliminating energy savings, minimum evaporation losses, minimum environmental pollution and phase changes.
3. For the working process, it is sufficient to provide simple containers, magnetic stirrer and atmospheric conditions for the environment.

4. Powder production in controllable shapes and sizes can be achieved.

5. Fiber production can be achieved by using metal-oxide solutions.

6. Production of amorphous solid glass materials, which cannot be obtained by liquid phase cooling, can be achieved.

7. Due to the low viscosity of the sol, it facilitates the preparation of thin coating films and allows the production of thin SiO_2 and TiO_2 coatings on the glass and to improve the mechanical, chemical, electrical and optical properties of the coated surfaces.

3.2. Preparation of spinel samples

The multifferoic spinel samples were synthesized by using sol-gel technique with $Co(NO_3)_2.6H_2O$, $Fe(NO_3)_3.9H_2O$, $Cr(NO_3)_3.9H_2O$ and Ho_2O_3 chemicals as starting materials. In order to obtain the desired stoichiometry, appropriate amounts of starting materials were first dissolved in distilled water at 50 °C, and then, citric acid and ethylene glycol were added to the mixture. A viscous residual was formed after slowly boiling the solutions at 200 °C. Afterwards the obtained residuals were dried slowly at 300 °C until a dry gel was formed. Finally, in order to remove organic materials produced during chemical reactions, the residual precursor was burned for one hour in air at 500 °C. The resulting powders were calcinated for 5 h in air at 550 °C, and thereafter, they were furnace cooled. After cooling, the resulting materials were grounded using an agate mortar to obtain fine powder. Afterwards, powder formed samples were pressed into discs and sintered at 1100 °C for 24 h in air atmosphere and then furnace cooled to the room temperature (RT). Figure 3.1 shows our sol-gel production process.

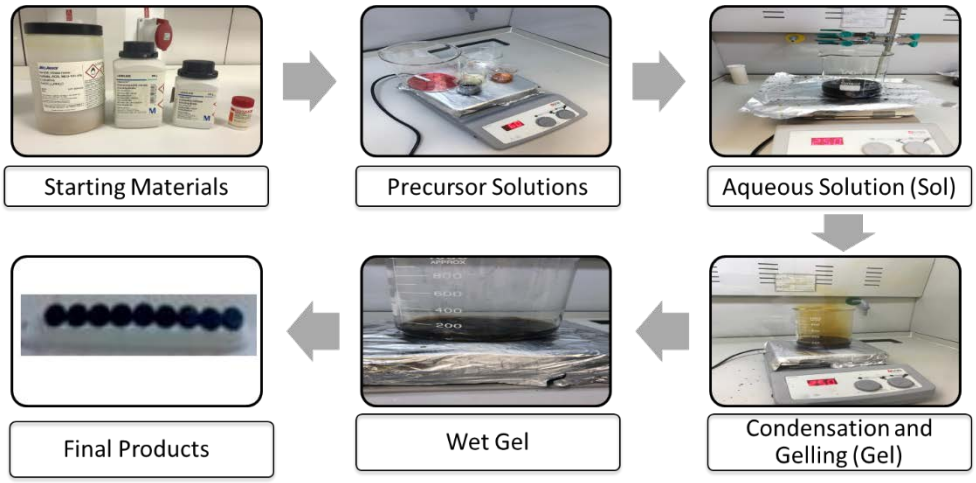

Figure 3.1. The process of preparing compounds.

3.3. Structural analysis

In this study, x-ray diffraction (XRD), scanning electron microscopy (SEM) and energy-dispersive x-ray spectrometry (EDS) measurements were performed to analyze structural properties of the produced spinel samples.

3.3.1. X-Ray diffraction (XRD) method

At the beginning of the twentieth century, the German physicist Max von Laue discovered that crystalline x-rays were refracted, when the atoms in the structure were crystal form. Laue predicted that it is possible for the wavelengths of x-rays to be refracted by the crystals because they are electromagnetic waves equal to the distance between the atoms in the crystals. He experimented with this prediction on the copper sulfate crystal. He placed it on an x-ray beam path to record the diffracted beam and he observed exemplary stains on the photographic plate. This experiment is also crucial to show that x-rays are in wave nature and to prove that atoms are arranged in crystals periodically. Due to this work, Laue was awarded the Nobel Prize in physics in 1914. Laue's experiment was received with great interest by British physicist W.L.Bragg. He expressed the conditions required for diffraction by analyzing the results of the experiment in a simple mathematics relation called "Bragg's Law". This mathematical expression expresses the necessary condition for diffraction.

In order to explain the Bragg law, the reflection of x-rays from two adjacent planes with a distance *d* between them is shown in Figure 3.2.

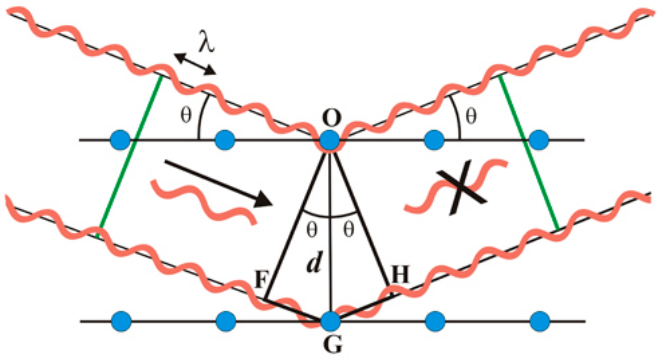

Figure 3.2. Diffraction of x-rays from crystal planes and Bragg law ("Bragg Law," 2020).

In Figure 3.2, λ is the wavelength of the x-ray, the θ is angle between the incident light and the reflection plane, and *d* is the distance between the planes. In order to occur a constructive

interference, the path difference taken by the scattered rays between the two consecutive planes must be exactly the multilples of wavelength. The reflected beams in this way are in the same phase and form diffraction beams by strengthening each other. This is known as the Bragg Law, and it is expressed as;

$$n\lambda = 2dsin\theta \tag{16}$$

here, n is an integer. Bragg reflection occurs only if it satisfies the condition $\lambda \leq 2d$. This result also gives a physical explanation on why we cannot use visible rays.

In the powder diffraction method, the crystal to be examined is turned into very fine powder and placed in a monochromatic (single wavelength) x-ray beam. Each part of the powder crystal is a very small crystal that is arbitrarily oriented relative to the incoming bundle. The maximum reflection occurs when the x-ray is oriented with the crystal planes to make the correct Bragg angle, and the scattered x-rays reach the monochromator and then the detector through the router slit. X-ray diffraction pattern is shown in a graph of the diffracted beams intensity as a function of the reflection angle (2θ). XRD measurements of the samples in this study were done by using PANalytical EMPYREAN x-ray diffraction analysis system (see Figure 3.3) with Cu-Kα (1.5405 Å) x-ray source in the Çukurova University Central Research Laboratory. Measurements were carried out at room temperature between 20 ° and 80 ° in steps of 0.002 °.

Figure 3.3. PANalytical EMPYREAN X-ray diffraction (XRD) system.

3.3.2. Scanning electron microscope (SEM) imaging and Energy-dispersive X-ray spectrum (EDS) methods

Scanning electron microscopy (SEM) is a method which is used to analyze the morphology of the micro and nanostructures of the material in high resolution. The surface of the material can be examined by accelerated high energy electrons scanning. As shown in Figure 3.4, an electron beam is produced in an electron gun placed in the upper part of the SEM. These electrons are usually produced by heating metallic filaments such as tungsten. After the electron beam leaves the gun, it passes through the microscope through electromagnetic lenses that will focus the beam on the sample. The orbit of electrons is adjusted by the current applied to the coils producing magnetic fields. When the electron beam hits the sample, it interacts with the sample's atoms (elastic and inelastic collisions) and causes scattering of other electrons from the sample. With a special detector placed in SEM, electron signals are collected from each pixel to create a suitable point-to-point image corresponding to the display screen. By combining the signals, an image of the scanned material is obtained.

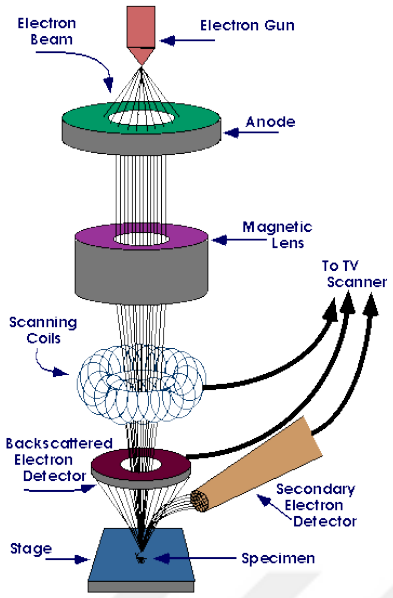

Figure 3.4. Working scheme of the scanning electron microscope (SEM) ("SEM," 2020).

The interaction of the high-voltage accelerated electron beam with the sample takes place in a similar manner to the water drop. As a result of inelastic interaction with the outer orbits of the material atoms, low-energy Auger electrons are formed, which carry information about the material surface and form the working principle of Auger spectroscopy. The types of electrons required in SEM are backscattered electrons and secondary electrons. Back scattering electrons are caused by elastic collisions of incoming electrons with atoms in the material. Back scattering electrons are high energy electrons scattered from the deep regions (50-300nm) of the sample surface and give information about the composition of the sample. Secondary electrons result from inelastic collisions of incoming electrons with atoms in the material. Secondary electrons emerge from an area of the surface of the sample at a depth of 5-50 nm with less energy than the electrons in the beam, providing the topographic image of the sample.

Energy-dispersive x-ray spectroscopy (EDS) is an analysis method that helps to determine the elements in a sample and the quantities of these elements. The EDS is in the form of a scanning electron microscope system. The x-rays emitted from the sample surface exposed to the high energy electron beam show characteristic features due to their energy and wavelengths. These characteristic x-rays are detected by special x-ray detectors. Thanks to the peaks obtained from the characteristic x-ray energy values of the elements, the analysis of the elements in the material is performed.

SEM images and EDS analyzes of the polycrystalline samples produced within the scope of the thesis were taken using the EDS integrated FEI Quanta FEG 650 model scanning electron microscope in the Çukurova University Central Research Laboratory (Figure 3.5). Tablet-shaped materials were cleaned and placed in the sample holder and SEM images were taken at at various magnification rates under vacuum. EDS analyzes were performed at 20 kV acceleration voltage.

Figure 3.5. EDS integrated FEI Quanta FEG-650 model scanning electron microscope.

3.4. Magnetic analysis

The Physical Property Measurement System (Quantum Design, PPMS) is a highly integrated system designed as the primary research equipment to accurately measure the physical properties of the material. PPMS system includes a variety of module in a one system. One of these modules is vibrating sample magnetometer (VSM). The PPMS systems are actively used in research laboratories worldwide and have the highest sensing sensitivities at wide temperature and magnetic field values required for material characterization. Temperature control system is sensitive to work between 2 K (-271ºC) - 400K (127 ºC) temperature range and provides control of heat flow to the sample area. The magnet control system adjusts the current from the power supply to create ±9 T magnetic field and allows the user to work in both continuous and discontinuous modes.

Magnetic measurements of all samples in this study were made using the Physical Property Measurement System (Quantum Design) PPMS Dyna Cool in ÇÜMERLAB laboratories (Figure 3.6). The operating temperature range of the system is 2-400 K and measurements can be taken at ± 9T magnetic field values. For all samples, magnetization measurements against temperature were made under 100 Oe magnetic field. Zero-field cooling (ZFC) and field cooling (FC) processes were applied for measurements. The transition temperatures of the samples from the magnetization measurements against temperature were determined and magnetic entropy changes of the materials were determined from the isothermal magnetization curves obtained by measuring the magnetization against the magnetic field with 4 K temperature steps in the regions above and below the transition temperature. In addition, magnetic hysteresis measurements were made at 5 K and 300 K temperatures for all samples.

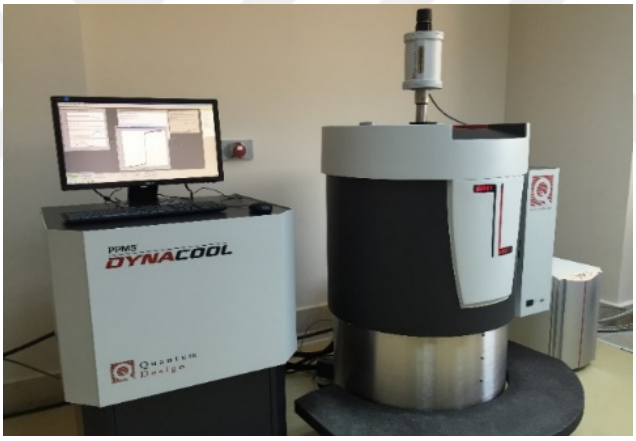

Figure 3.6. Quantum Design Dyna-Cool Phyical Property Measurement Sytem (PPMS).

4. RESULTS AND DISCUSSIONS

As explained in Chapter 1, the spinel materials (SMs) are formed as AB_2O_4 chemical formula where A is divalent 2+ and B is trivalent 3+ ions. In this thesis, the main spinel material is selected as cobalt-chromite ($CoCr_2O_4$) where divalent ion is Co^{2+} and trivalent ion is Cr^{3+}. Due to its considerable low magnetic transition temperature (around 98 K), we have substituted Fe^{3+} ions into the main structure by replacing with Cr^{3+} ions to arrange the magnetic transition temperature. Section 4.1 includes all experimental and theoretical calculations on optimization of transition temperature of Co-based SMs. Next, the effect of Ho, as a rare-earth element, doping into Co-based optimized spinel structure on structural, magnetic and magnetocaloric properties will be discussed in Section 4.2.

4.1. Optimization of transition temperature

In this section, the magnetic phase transition will be optimized by the substitution of Fe^{3+} ions with Cr^{3+} ions in B-site of cobalt-chromite spinel materials. The purpose of this work is to determine a suitable material having a magnetic phase transition occurring around room temperature for possible magnetism-based applications. In addition to the magnetic transition temperature, the magnetic moment of the produced sample will be enhanced due to substitution of anti-ferromagnetic Cr^{3+} ions by ferromagnetic Fe^{3+} ions in cobalt-based spinel structure. As we have already discussed in Chapter 3, various combinations of samples were synthesized by sol-gel process. The samples are labelled as given in the following Table. 4.1.

Table 4.1. Sample codes and their corresponding chemical formulas.

Sample Code	*x*-value in $Co(Cr_{1-x}Fe_x)_2O_4$	Chemical Formula
CCO	0.00	$CoCr_2O_4$
CCFO-1	0.25	$CoCr_{1.5}Fe_{0.5}O_4$
CCFO-2	0.50	$CoCr_{1.0}Fe_{1.0}O_4$
CCFO-3	0.75	$CoCr_{0.5}Fe_{1.5}O_4$
CFO	1.00	$CoFe_2O_4$

Before working magnetic properties of the produced samples, structural properties will be discussed in Section 4.1.1. After that the magnetic properties of these samples will be discussed in Section 4.1.2.

4.1.1. Structural properties of $Co(Cr_{1-x}Fe_x)_2O_4$ ($0.0 \leq x \leq 1.0$) spinel materials

4.1.1.1. X-ray diffraction (XRD) analysis of $Co(Cr_{1-x}Fe_x)_2O_4$ spinels

The synthesized samples are first characterized by x-ray diffraction (XRD) measurements. The samples are grinded before the XRD experiment to get fine powder form. XRD spectrum data were collected in a wide range of scanning angle from 20° to 80°. Figures 4.1(a-e) show the XRD patterns of $Co(Cr_{1-x}Fe_x)_2O_4$ spinel samples for x=0.00, 0.25, 0.50, 0.75 and 1.00, respectively. After collecting the XRD data, we have performed the data analysis by using High-Score Plus software to determine the crystal phase, lattice parameters, crystallite size and other structural parameters. Based on this analysis, the crystal structure of all samples are found as cubic structure. Due to having same crystal structure (*Fd-3m* space group) of $CoCr_2O_4$ and $CoFe_2O_4$ samples, it is considered that the substitution of Fe^{3+} ions by Cr^{3+} did not disrupt the crystal lattice.

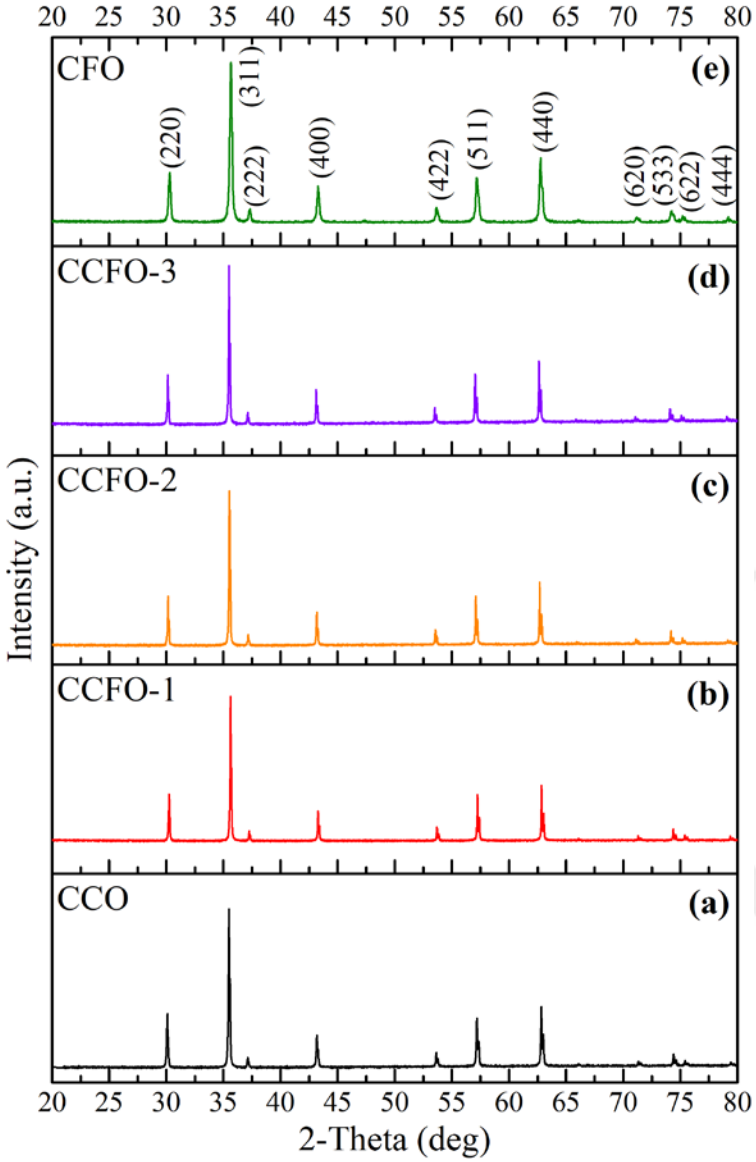

Figure 4.1. XRD patterns of $Co(Cr_{1-x}Fe_x)_2O_4$ spinel samples for a) x=0.00, b) x=0.25, c) x=0.50, d) x=0.75 and e) x=1.00.

The lattice parameters of the samples are found as 8.331, 8.352, 8.374, 8.381 and 8.412 for x=0.00, 0.25, 0.50, 0.75 and 1.00, respectively that it increases linearly with increasing of the Fe^{3+} content in $Co(Cr_{1-x}Fe_x)_2O_4$ lattice as shown in Figure 4.2. Since the ionic radii of Fe^{3+} (0.785Å) is larger than that of Cr^{3+} (0.755Å), the lattice is enlarged by the replacement of Fe^{3+} with Cr^{3+} ions. Because the Fe^{3+} ion doping generally prefers to settle into the A-site of spinel structure rather than B-site, the Co^{2+} will be forced to occupy in B-site when Fe^{3+} content is increased and finally (x=1.0) it becomes inverse spinel structure means half of the Fe^{3+} ions are settled into the A-site and another half of it is settled into the B-site. Due to this physical

phenomena, the lattice parameter increases with increasing Fe content in such spinel structure that Co^{2+} (0.885Å) ionic radii is larger than Fe^{3+}.

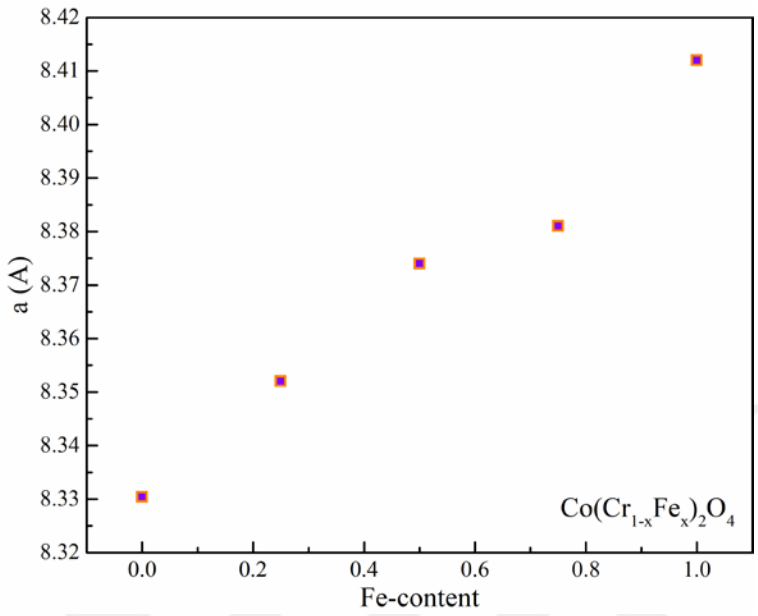

Figure 4.2. Lattice parameter as a function of Fe content in $Co(Cr_{1-x}Fe_x)_2O_4$ spinel structure.

Further structural properties were studied by calculating crystallite size of samples by using Debye-Scherrer equation;

$$D = \frac{\lambda\kappa}{\beta sin\theta} \tag{17}$$

where D is the crystallite size, λ is the x-ray wavelength (CuKα=1.5406Å), κ is the shape factor, β is the full-width at half maximum of the diffraction peaks and θ is the Bragg angle. We see a linear correlation between crystallite size and Fe content in $Co(Cr_{1-x}Fe_x)_2O_4$ spinel samples. All structural parameters (lattice constant, volume of a unit cell, *d*-spacing values and crystallite size) are tabulated in Table 4.2.

Table 4.2. Structural properties of $Co(Cr_{1-x}Fe_x)_2O_4$ ($0.0 \leq x \leq 1.0$) spinel samples.

Sample Code	*x*-value in $Co(Cr_{1-x}Fe_x)_2O_4$	*a* (Å)	V ($Å^3$)	*d*-spacing value (Å)	*D* (nm)
CCO	0.00	8.331	578.09	2.5076	75.46
CCFO-1	0.25	8.352	582.68	2.5183	234.89
CCFO-2	0.50	8.374	587.38	2.5250	233.32
CCFO-3	0.75	8.381	588.84	2.5271	311.07
CFO	1.00	8.412	594.88	2.5358	361.66

4.1.1.2. Scanning electron microscopy (SEM) imaging and Energy-dispersive x-ray spectrum (EDS) analysis of $Co(Cr_{1-x}Fe_x)_2O_4$ spinels

The morphological properties of produced samples have been studied by performing scanning electron microscope (SEM) imaging measurements. SEM imaging technique allows us to observe grains and their distribution. The grain size distribution for all samples has been determined by taking into account of randomly selected 100 grains in the SEM image and imageJ software.

SEM images of $CoCr_2O_4$ nanocrystals taken at 25kX and 100kX magnifications are presented in Figs. 4.3(a-b), respectively. The grains are uniformly formed and their shapes can be defined as cubic nanocrystal. The average grain size of nanocrystals is found around 210 nm for CCO sample (see Fig.4.3c).

Energy-dispersive x-ray spectrum (EDS) of CCO sample is shown in Fig.4.3d. As it can be seen that the EDS spectrum shows just our compounds element without any impurity. Inset of Fig.4.3d shows the weight and atomic percentage of each element in the compound. The chemical composition determined from energy-dispersive x-ray spectroscopy analysis is consisted with the nominal composition. The desired and EDS atomic percent results of each element are tabulated in Table 4.3.

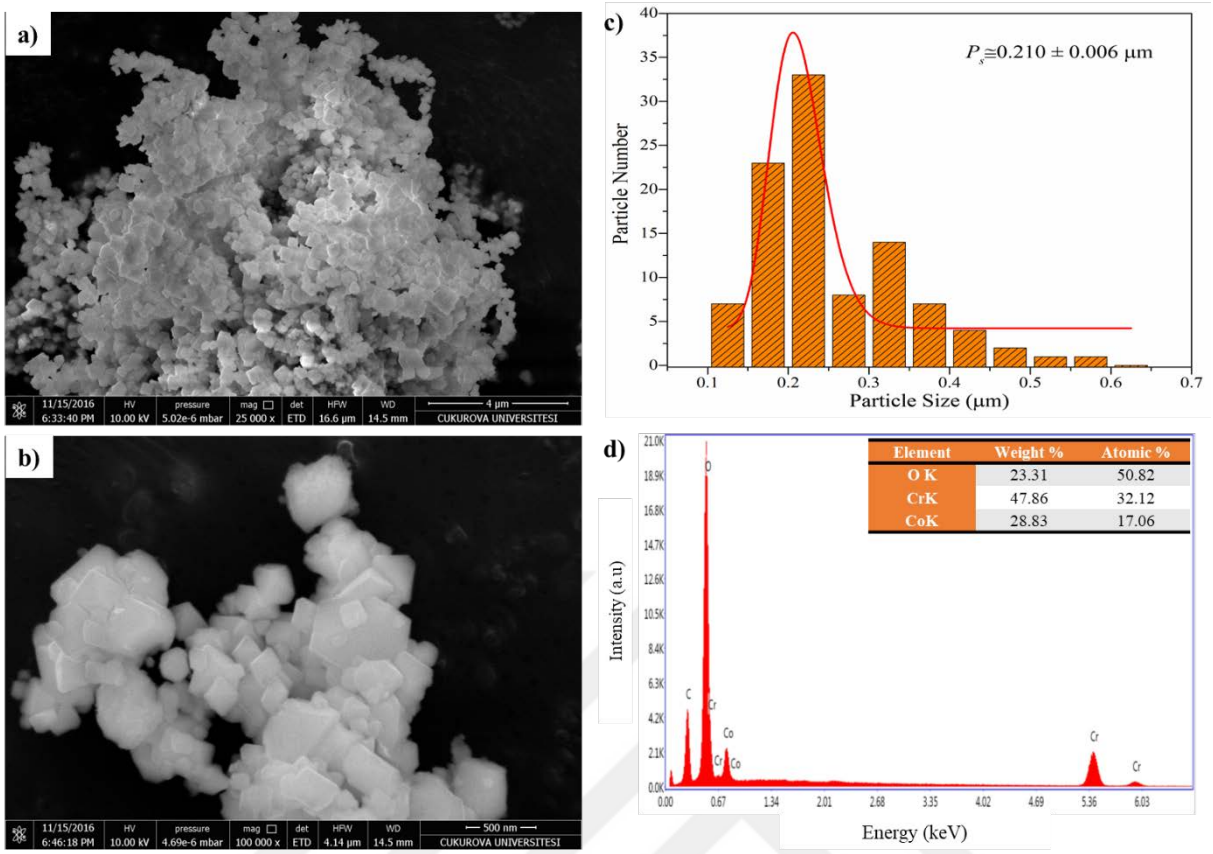

Figure 4.3. CCO sample's; a-b) SEM images, c) particle size distribution and d) EDS spectrum. Inset of d) atomic and weight percentage of elements.

SEM images of CCFO-1 nanocrystals taken at 15kX and 100kX magnifications are presented in Figs. 4.4(a-b), respectively. The grains are uniformly formed and their shapes can be defined as cubic nanocrystal. The average grain size of nanocrystals is found around 571 nm for CCFO-1 sample (see Fig.4.4c). The average grain size is increased when Fe is substituted into the lattice.

EDS spectrum of CCFO-1 sample is shown in Fig.4.4d. As it can be seen that the EDS spectrum shows just our compounds element without any impurity. Inset of Fig.4.4d shows the weight and atomic percentage of each element in the compound. The chemical composition determined from energy-dispersive x-ray spectroscopy analysis is consisted with our expected composition. The desired and EDS atomic percent results of each element are tabulated in Table 4.3.

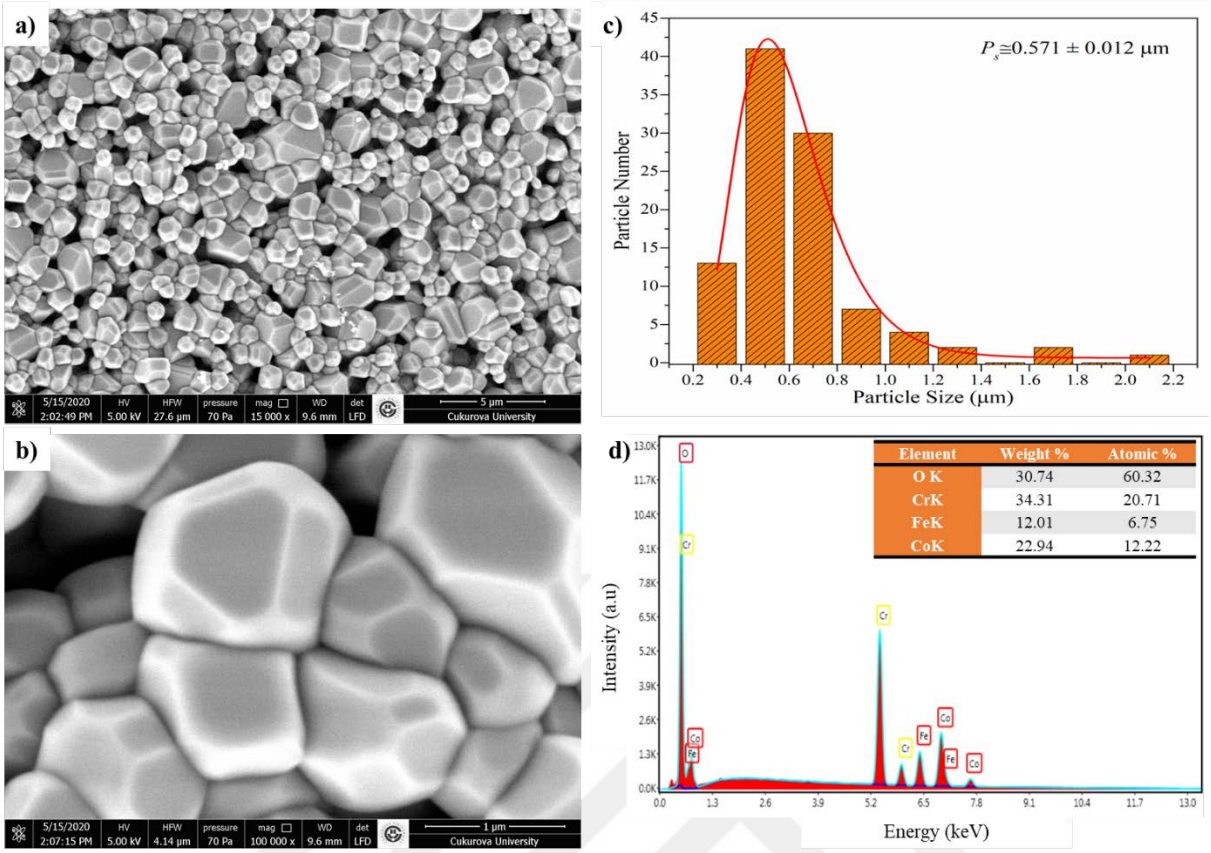

Figure 4.4. CCFO-1 sample's; a-b) SEM images, c) particle size distribution and d) EDS spectrum. Inset of d) atomic and weight percentage of elements.

SEM images of CCFO-2 nanocrystals taken at 15kX and 100kX magnifications are presented in Figs. 4.5(a-b), respectively. The grains are uniformly formed and their shapes can be defined as cubic nanocrystal, but the corner of cubic shape becomes oval. The average grain size of nanocrystals is found around 788 nm for CCFO-2 sample (see Fig.4.5c). The average grain size is increased when Fe content is increased in the lattice.

EDS spectrum of CCFO-2 sample is shown in Fig.4.5d. As it can be seen that the EDS spectrum shows just our compounds element without any impurity. Inset of Fig.4.5d shows the weight and atomic percentage of each element in the compound. The chemical composition determined from energy-dispersive x-ray spectroscopy analysis is consisted with our expected composition. The desired and EDS atomic percent results of each element are tabulated in Table 4.3.

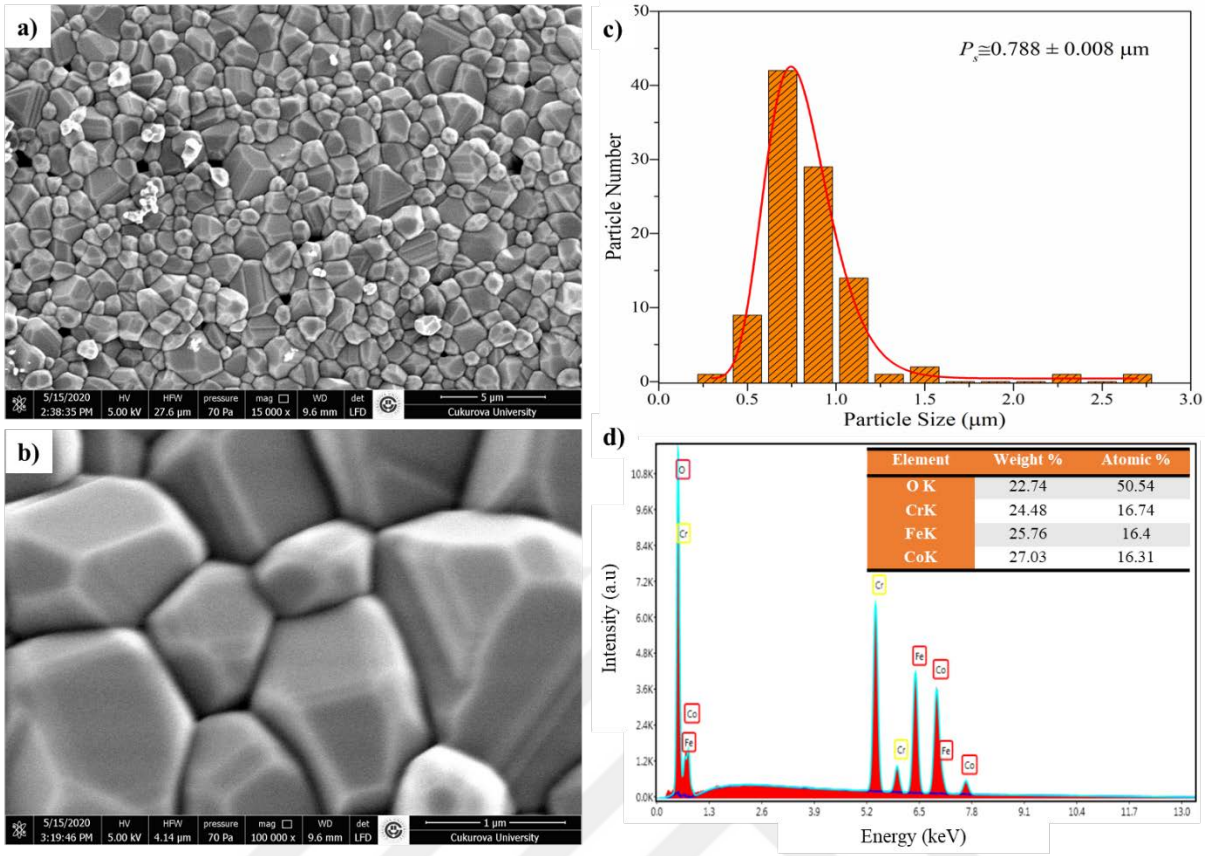

Figure 4.5. CCFO-2 sample's; a-b) SEM images, c) particle size distribution and d) EDS spectrum. Inset of d) atomic and weight percentage of elements.

SEM images of CCFO-3 nanocrystals taken at 15kX and 100kX magnifications are presented in Figs.4.6(a-b), respectively. The grains are uniformly formed and their shapes can be defined as cubic nanocrystal. The corner of grains becomes sharp-edged. The average grain size of nanocrystals is found around 1.074 µm for CCFO-3 sample (see Fig.4.6c). The average grain size is increased when Fe content is increased in the lattice.

EDS spectrum of CCFO-3 sample is shown in Fig.4.6d. As it can be seen that the EDS spectrum shows just our compounds element without any impurity. Inset of Fig.4.6d shows the weight and atomic percentage of each element in the compound. The chemical composition determined from energy-dispersive x-ray spectroscopy analysis is consisted with our expected composition. The desired and EDS atomic percent results of each element are tabulated in Table 4.3.

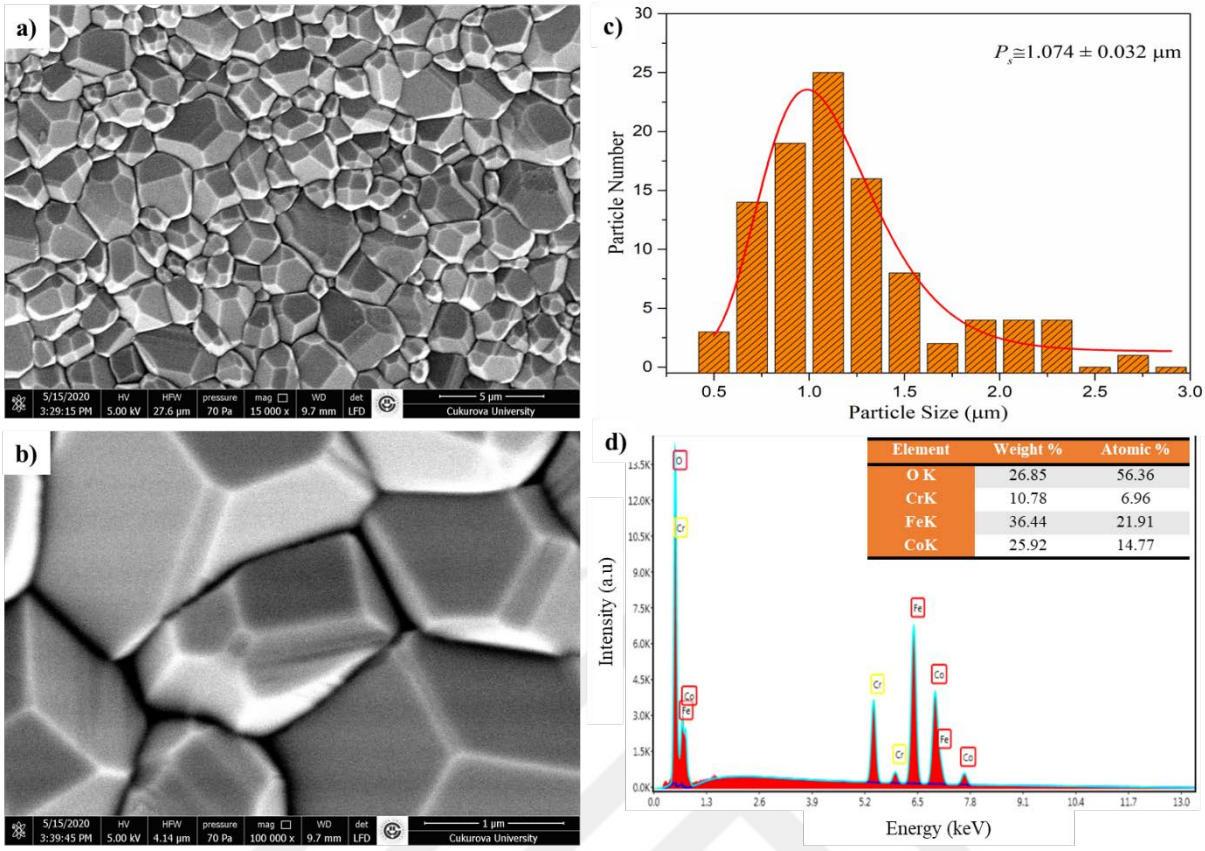

Figure 4.6. CCFO-3 sample's; a-b) SEM images, c) particle size distribution and d) EDS spectrum. Inset of d) atomic and weight percentage of elements.

SEM images of CFO nanocrystals taken at 5kX and 100kX magnifications are presented in Figs. 4.7(a-b), respectively. The grains are not uniformly formed and distributed in the sample. It is hard to identicate the grain size distribution and to determine the average grain size for CFO sample. But, it can be seen from all SEM images that the average grain size increased with increasing Fe content in main spinel structure. The average grain size of nanocrystals is found around 1.365 µm for CFO sample (see Fig.4.7c).

EDS spectrum of CFO sample is shown in Fig.4.7d. As it can be seen that the EDS spectrum shows just our compounds element without any impurity. Inset of Fig.4.7d shows the weight and atomic percentage of each element in the compound. The chemical composition determined from energy-dispersive x-ray spectroscopy analysis is consisted with our expected composition. The desired and EDS atomic percent results of each element are tabulated in Table 4.3.

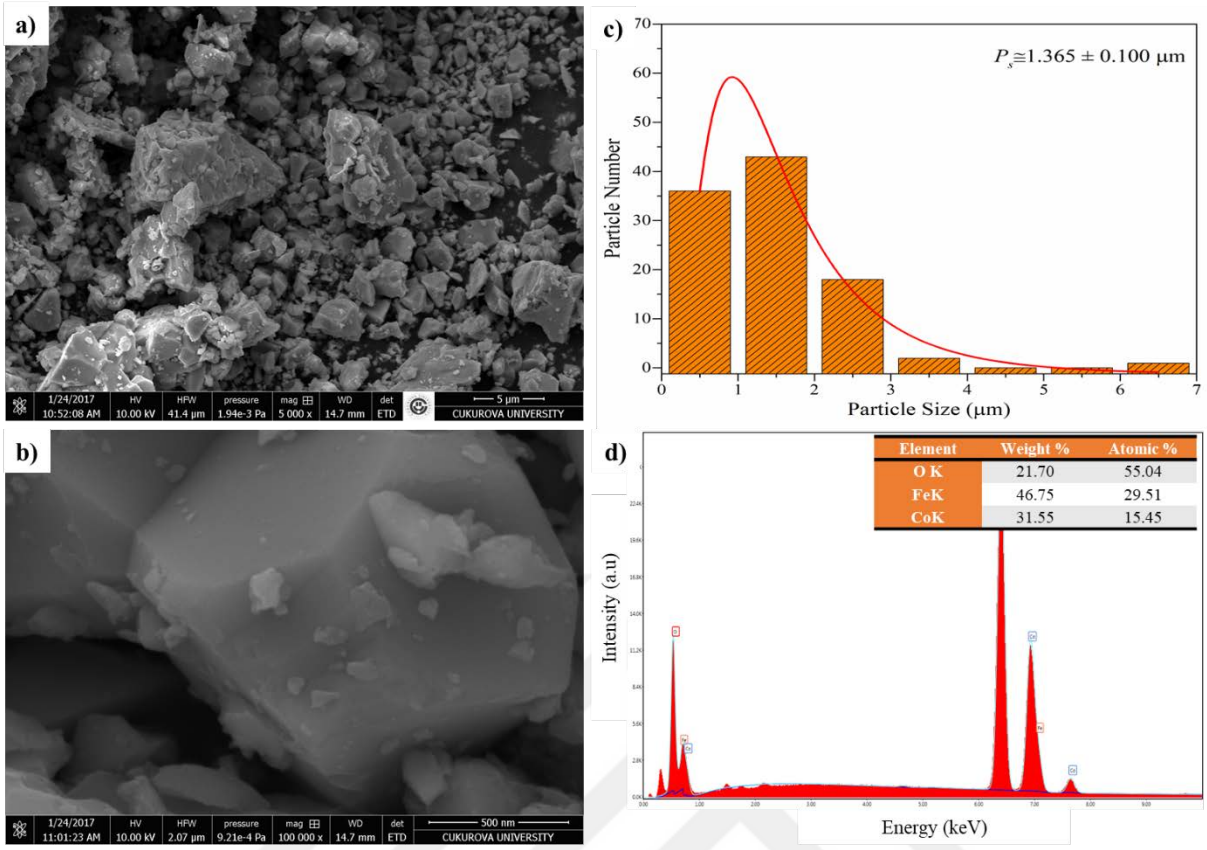

Figure 4.7. CFO sample's; a-b) SEM images, c) particle size distribution and d) EDS spectrum. Inset of d) atomic and weight percentage of elements.

Table 4.3. The desired and EDS results of atomic percent of each element in $Co(Cr_{1-x}Fe_x)_2O_4$ spinel materials.

Sample Code	Desired				Obtained from EDS			
	Co	Cr	Fe	O	Co	Cr	Fe	O
CCO	1.00	2.00	0.00	4.00	1.19	2.25	0.00	3.56
CCFO-1	1.00	1.50	0.50	4.00	0.86	1.45	0.47	4.22
CCFO-2	1.00	1.00	1.00	4.00	1.14	1.17	1.15	3.54
CCFO-3	1.00	0.50	1.50	4.00	1.03	0.49	1.53	3.95
CFO	1.00	0.00	2.00	4.00	1.08	0.00	2.07	3.85

4.1.2. Magnetic properties of $Co(Cr_{1-x}Fe_x)_2O_4$ ($0.0 \leq x \leq 1.0$) spinel materials

4.1.2.1. Temperature dependence of magnetic properties of $Co(Cr_{1-x}Fe_x)_2O_4$ spinel materials

Magnetic properties of produced samples first studied by temperature sweeping moment measurement in both zero-field-cooled (ZFC) and field-cooled (FC) conditions in the range of 5 – 380 K with an applied of 100 Oe. In ZFC magnetization measurement, the samples were

cooled from room temperature to 5 K with zero field and after stabilization of temperature, then moment data were recorded when samples were warming with a field of 100 Oe. In the FC mode, a field of 100 Oe was applied then samples were cooled down from room temperature to 5 K and moment data were recorded when cooling in the same field. Figure 4.8 shows the temperature dependence of magnetic moment of $CoCr_2O_4$ spinel material. The magnetic transition temperature (T_c) was found as 95 K for CCO sample.

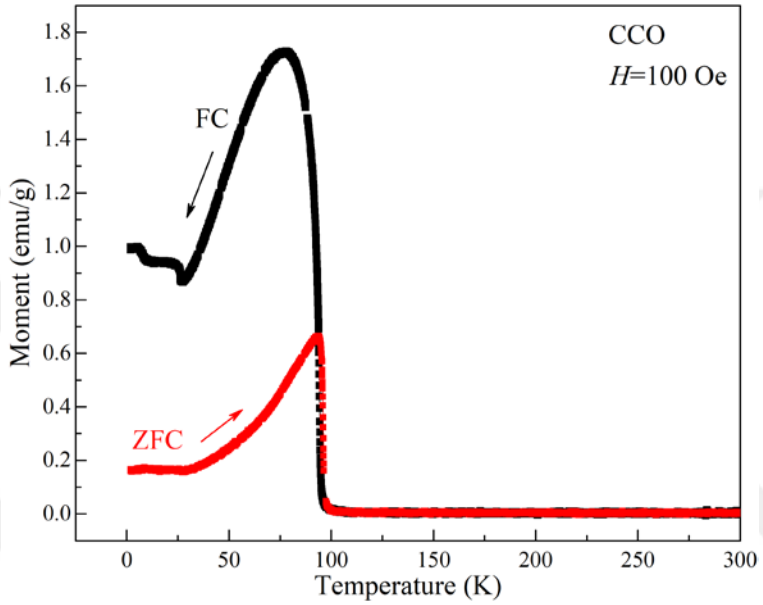

Figure 4.8. Temperature dependence of magnetic moment of $CoCr_2O_4$ spinel material.

Figure 4.9 shows the temperature dependence of magnetic moment of CCFO-1 sample. The magnetic transition temperature increased to 170 K when it is compared to Fe-free sample. This increment is expected because of doping ferromagnetic ordering ions into the antiferromagnetic ordering cite in cobalt-chromite spinel material structure. But it is still far away than the room temperature for practical applications. In addition to magnetic transition temperature, the magnetic moment value of sample increased with adding Fe^{3+} ions in $CoCr_2O_4$ spinel lattice that is confirmed the substitution of Fe^{3+} ions into the Cr^{3+} site in spinel lattice. The interesting point in this figure is that the negative moment in ZFC curve under around 125 K temperature. This behavior might come from the inverse spinel structure.

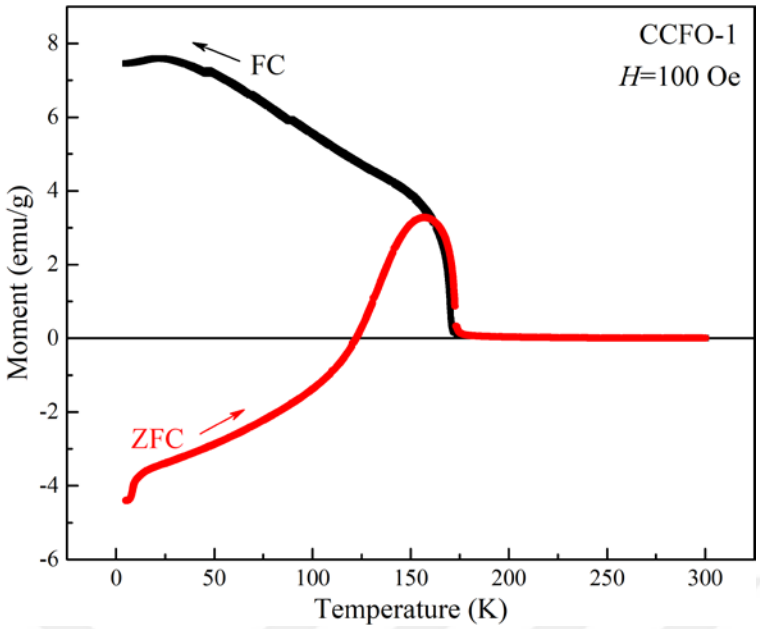

Figure 4.9. Temperature dependence of magnetic moment of $Co(Cr_{1-x}Fe_x)_2O_4$ spinel material for x=0.25.

Figure 4.10 shows the temperature dependence of magnetic moment of CCFO-2 sample. The magnetic transition temperature increased to 315 K when it is compared to other previous samples. Moreover, the magnetic moment value increased almost 12 times when it is compared to the Fe-free cobalt-chromite spinel sample. These magnetic properties (transition temperature and moment) make this sample suitable for practical application.

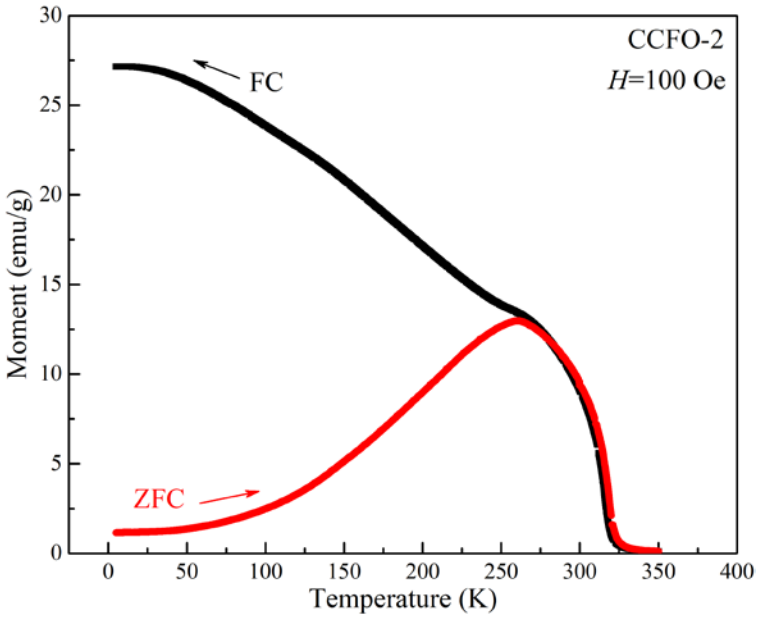

Figure 4.10. Temperature dependence of magnetic moment of $Co(Cr_{1-x}Fe_x)_2O_4$ spinel material for x=0.50.

Figure 4.11 shows the temperature dependence of magnetic moment of CCFO-3 sample. The magnetic transition could not be observed in working temperature range because of our measurement system's limit (~380 K). But, it can be said that the magnetic transition temperature is far away this limit.

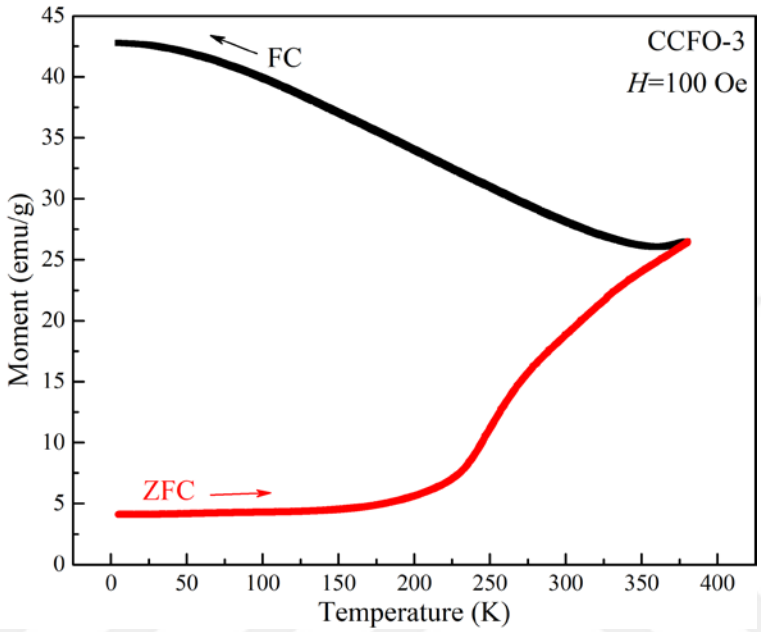

Figure 4.11. Temperature dependence of magnetic moment of $Co(Cr_{1-x}Fe_x)_2O_4$ spinel material for x=0.75.

Figure 4.12 indicates the *M-T* curves of $CoFe_2O_4$ spinel sample. Similar to the $CoCr_{0.5}Fe_{1.5}O_4$ sample, we could not see the magnetic transition point because of our measurement system's limit (~380 K).

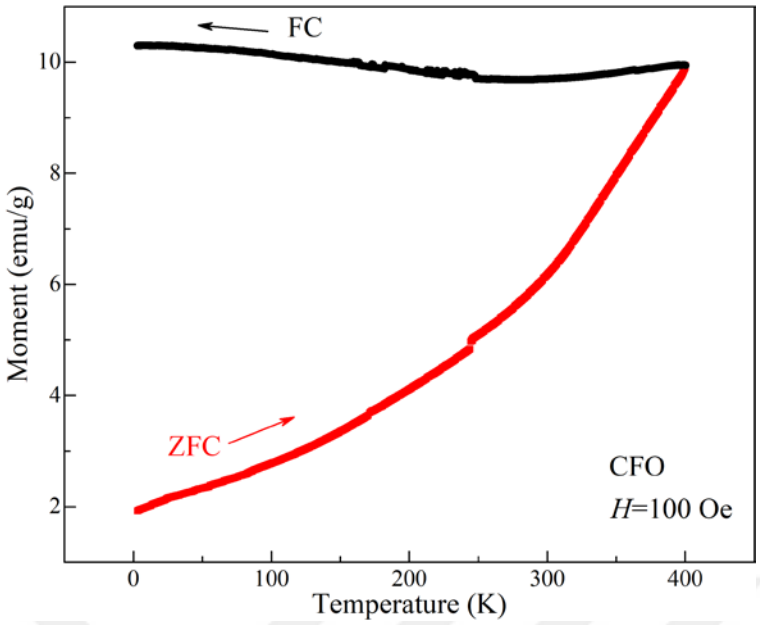

Figure 4.12. Temperature dependence of magnetic moment of $CoFe_2O_4$ spinel material.

The magnetic transition temperature versus Fe concentration in $Co(Cr_{1-x}Fe_x)_2O_4$ is shown in Figure 4.13. Due to the limit of our VSM system, we could not detect the transition temperature for x=0.75 and 1.0 in $Co(Cr_{1-x}Fe_x)_2O_4$. Here, it is obvious that the transition temperature increases with increasing Fe concentration in cobalt-chromite spinel structure. Therefore, we can conclude from the temperature dependence magnetization measurement that the most suitable sample is $CoCrFeO_4$ for practical application due to its wide magnetic transition temperature range around room temperature.

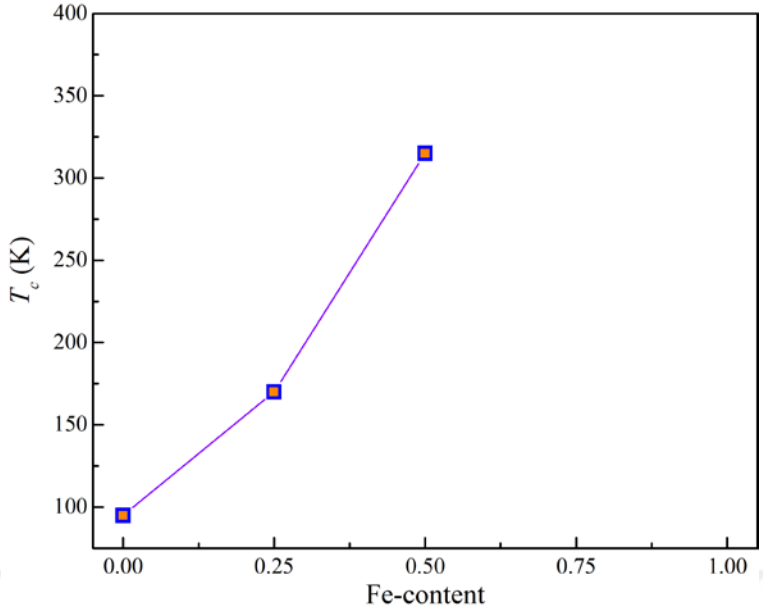

Figure 4.13. Fe-concentration as a function of magnetic transition temperature in $Co(Cr_{1-x}Fe_x)_2O_4$ spinel material.

4.1.2.2. Magnetic hysteresis of $Co(Cr_{1-x}Fe_x)_2O_4$ spinel materials

Next, we performed magnetic hysteresis (*M*-*H*) measurements by sweeping applied field at low (5 K) and room temperature (300 K) for all samples. For low temperature measurements, we cooled samples without applying magnetic field. Then, magnetic field is applied to the samples at constant ramping. Figure 4.14 shows magnetic hysteresis curve of CCO sample measured at 5 K. The full hysteresis curve indicates the CCO sample is ferromagnetically coupled at low temperature. This behavior is consistent with the *M*-*T* curve as shown in Figure 4.8. The coercive field (H_c), saturation magnetization (M_s) and remenant magnetization (M_r) were found as 3954 Oe, 2.83 emu/g and 1.39 emu/g, respectively. Since the sample has paramagnetic contribution, CCO sample could not saturate at 5 K. Due to this unsaturate situation, the M_s value is extracted from the point to be that the applied field is 5 T.

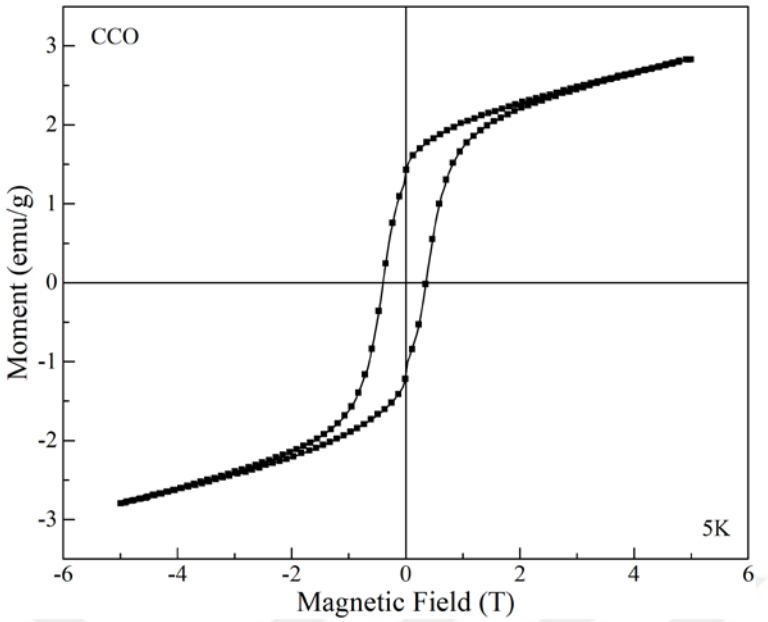

Figure 4.14. Magnetic hysteresis curve of $CoCr_2O_4$ sample at 5 K.

In addition to low temperature measurement, *M-H* curve was measured at room temperature as shown in Figure 4.15. The linearity of this curve indicates the sample is paramagnetic at room temperature. Since the CCO's magnetic transition temperature is around 95 K, this curve is consistent with the *M-T* result.

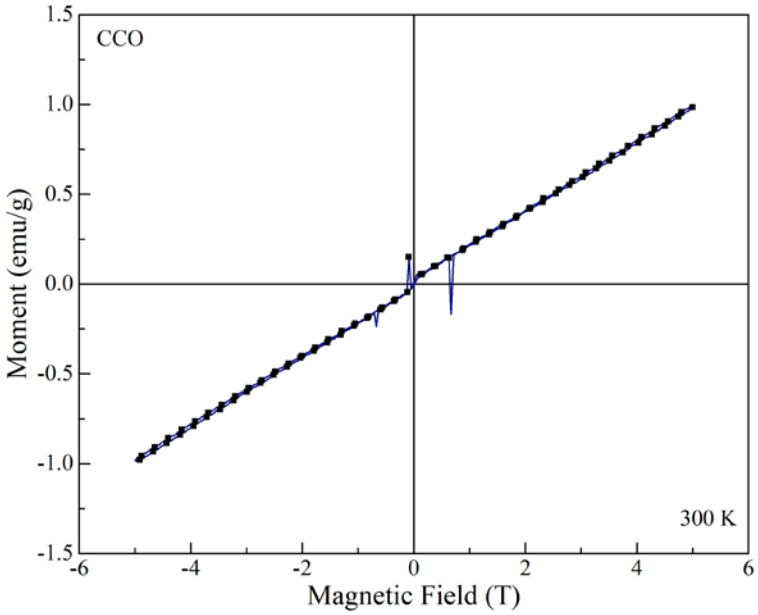

Figure 4.15. Magnetic hysteresis curve of $CoCr_2O_4$ sample at 300 K.

Figure 4.16 shows CCFO-1 sample's magnetic hysteresis curve measured at 5 K. A fully saturated magnetic hysteresis curve having coercieve field indicates CCFO-1 sample is

ferromagnetic order at 5 K. The H_c, M_s and M_r values were found as 776 Oe, 18.79 emu/g and 12.31 emu/g, respectively. It might be compared that the coercive field (saturation magnetization) decreases (increases) when Fe is added (for x=0.25) into the $Co(Cr_{1-x}Fe_x)_2O_4$ spinel lattice.

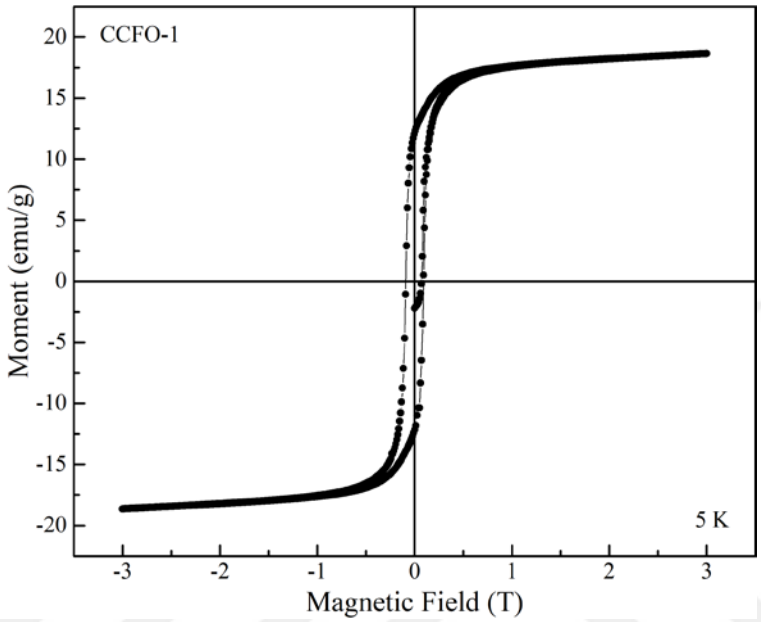

Figure 4.16. Magnetic hysteresis curve of $Co(Cr_{1-x}Fe_x)_2O_4$ spinel material for x=0.25 at 5 K.

The CCFO-1 sample's room temperature magnetic moment versus applied magnetic field measurement indicates a linear behavior that means the sample is paramagnetic at 300 K (see Figure 4.17). This result is consistent with the *M-T* curve (see Figure 4.9)

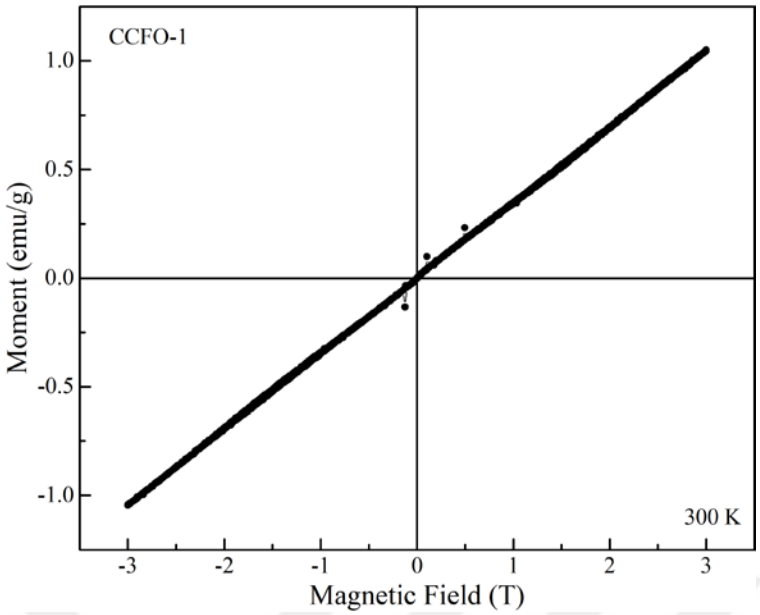

Figure 4.17. Magnetic hysteresis curve of $Co(Cr_{1-x}Fe_x)_2O_4$ spinel material for x=0.25 at 300 K.

Figure 4.18 shows CCFO-2 sample's magnetic hysteresis curve measured at 5 K. A fully saturated magnetic hysteresis curve having coercieve field indicates CCFO-2 sample is ferromagnetic order at 5 K. The H_c, M_s and M_r values were found as 954 Oe, 52.29 emu/g and 42.27 emu/g, respectively. The H_c and M_s values increase when Fe content is reached upto x=0.50 in the $Co(Cr_{1-x}Fe_x)_2O_4$ spinel lattice.

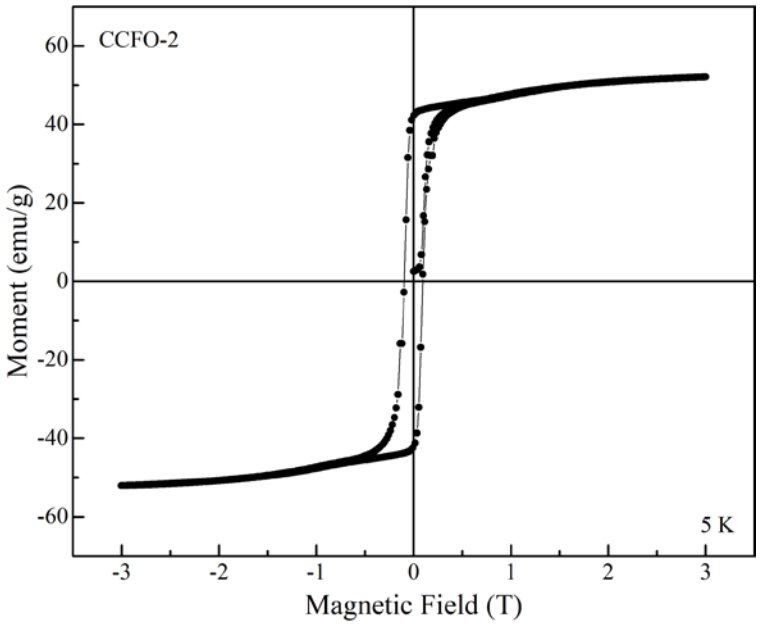

Figure 4.18. Magnetic hysteresis curve of $Co(Cr_{1-x}Fe_x)_2O_4$ spinel material for x=0.50 at 5 K.

In contrast to CCO and CCFO-1 samples, the CCFO-2 sample's room temperature magnetic moment indicates a non-linear behavior with applied magnetic field that means the sample is not paramagnetic at 300 K (see Figure 4.19). This result is consistent with the *M-T* curve (see Figure 4.10) that we observed the magnetic transition temperature at around 320 K.

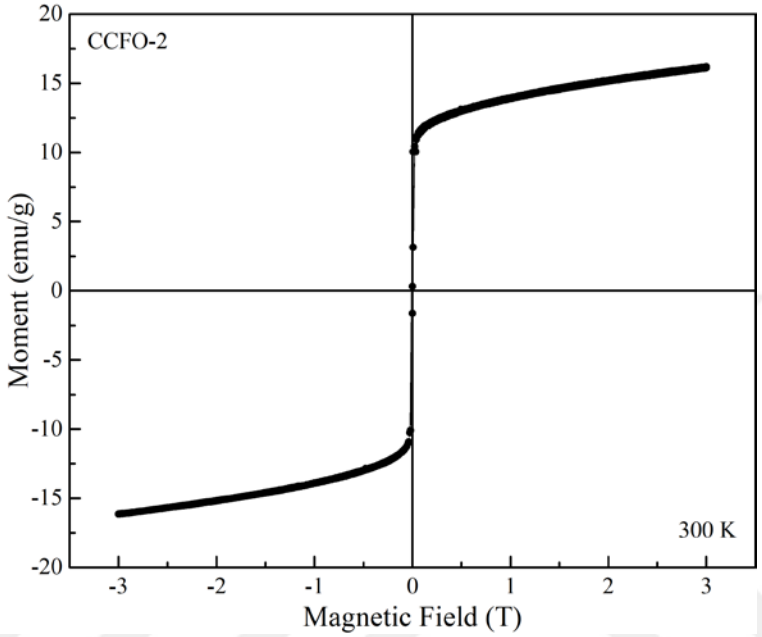

Figure 4.19. Magnetic hysteresis curve of $Co(Cr_{1-x}Fe_x)_2O_4$ spinel material for x=0.50 at 300 K.

Figure 4.20 shows CCFO-3 sample's magnetic hysteresis curve measured at 5 K. A fully saturated magnetic hysteresis curve having coercieve field indicates CCFO-3 sample is ferromagnetic order at 5 K. The H_c, M_s and M_r values were found as 1481 Oe, 79.56 emu/g and 71.37 emu/g, respectively. The H_c and M_s values increase when Fe content is reached upto x=0.75 in the $Co(Cr_{1-x}Fe_x)_2O_4$ spinel lattice.

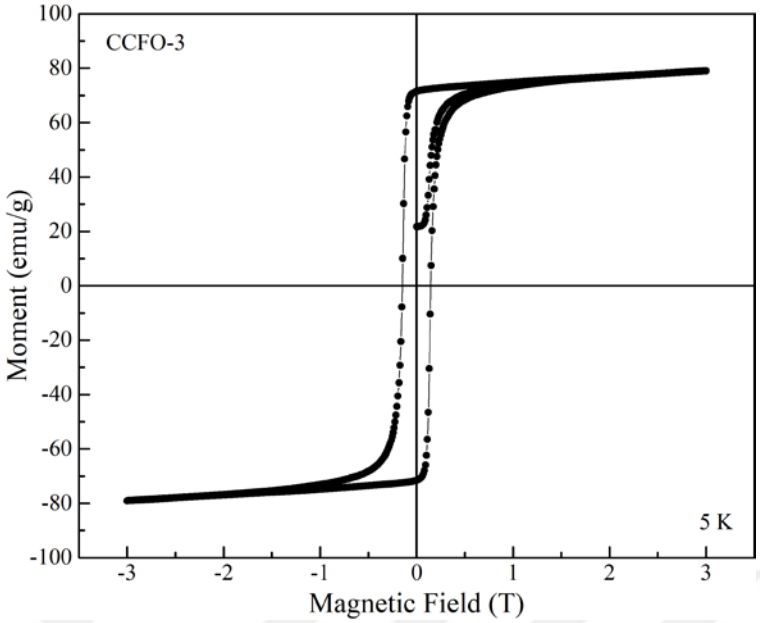

Figure 4.20. Magnetic hysteresis curve of $Co(Cr_{1-x}Fe_x)_2O_4$ spinel material for x=0.75 at 5 K.

The CCFO-3 sample's room temperature magnetic moment indicates a non-linear behavior with applied magnetic field that means the sample is not paramagnetic at 300 K (see Figure 4.21) that is similar to CCFO-2 sample's curve. This result is consistent with the *M-T* curve (see Figure 4.11) that we could not see the magnetic transition temperature in our working temperature range.

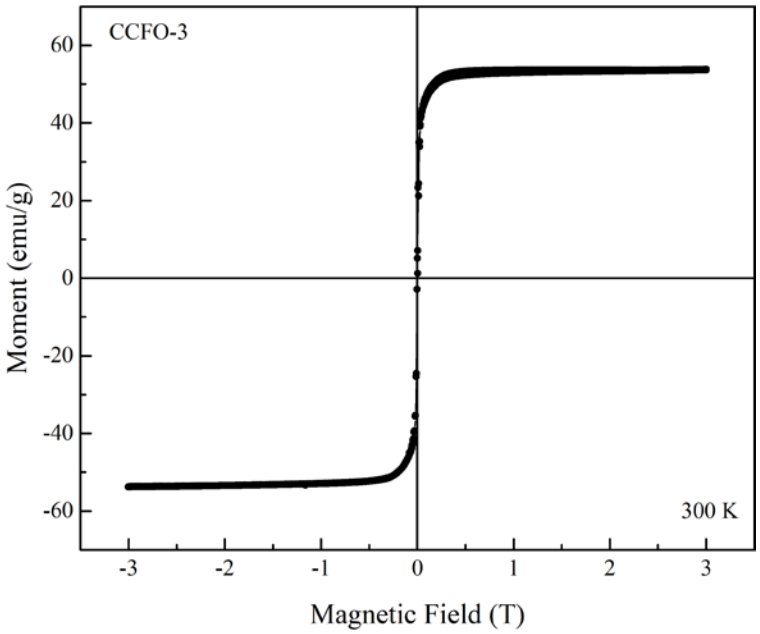

Figure 4.21. Magnetic hysteresis curve of $Co(Cr_{1-x}Fe_x)_2O_4$ spinel material for x=0.75 at 300 K.

Figure 4.22 shows CFO sample's magnetic hysteresis curve measured at 5 K. A fully saturated magnetic hysteresis curve having coercieve field indicates CFO sample is ferromagnetic order at 5 K. The H_c, M_s and M_r values were found as 3043 Oe, 90.83 emu/g and 66.09 emu/g, respectively. The H_c and M_s values increase when Fe content is reached to x=1.0 in the $Co(Cr_{1-x}Fe_x)_2O_4$ spinel lattice that means we have fully cobalt-ferrite spinel material.

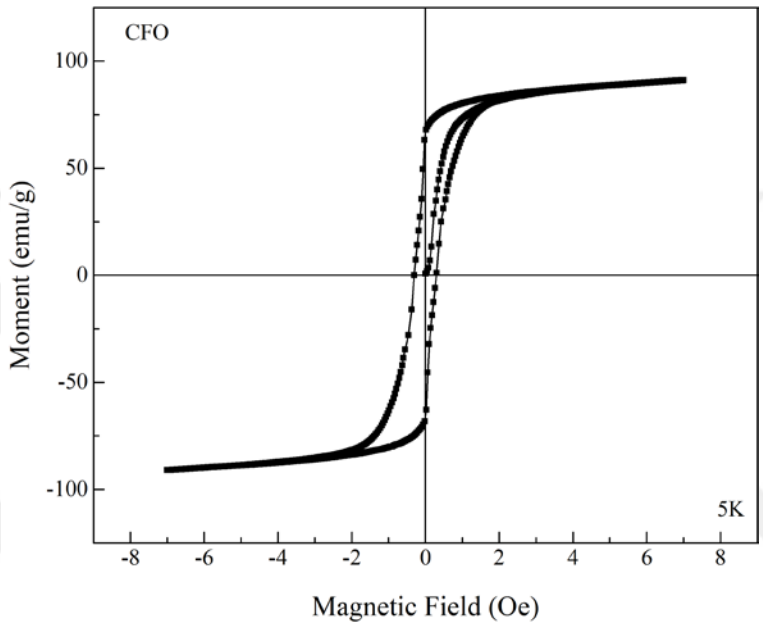

Figure 4.22. Magnetic hysteresis curve of $CoFe_2O_4$ spinel material at 5 K.

The CFO sample's room temperature magnetic moment indicates a non-linear behavior with applied magnetic field that means the sample is not paramagnetic at 300 K (see Figure 4.23) that is similar to CCFO-2 and CCFO-3 sample's curve. This result is consistent with the *M*-*T* curve (see Figure 4.12) that we could not see the magnetic transition temperature in our working temperature range.

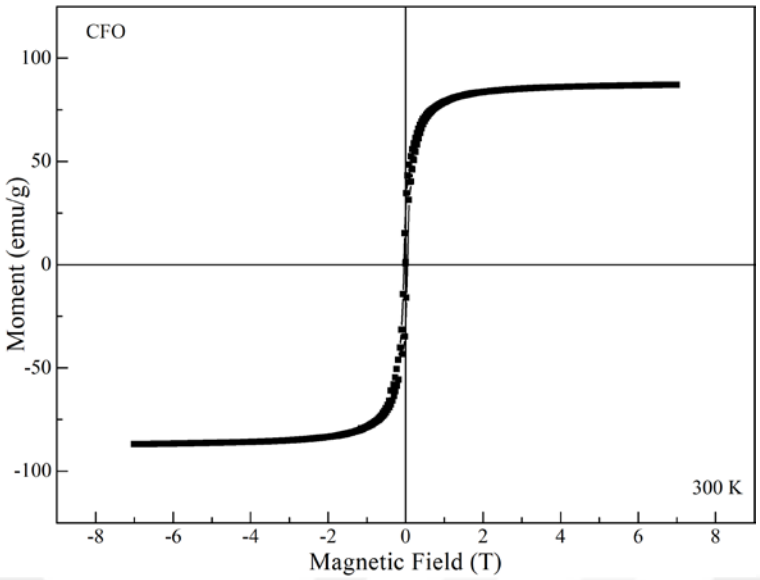

Figure 4.23. Magnetic hysteresis curve of $CoFe_2O_4$ spinel material at 300 K.

Figure 4.24(a-d) show the saturation magnetization, coercieve field, remenant magnetization and the ratio of remanant magnetization versus saturation magnetization as a function of Fe content in cobalt chromite spinel structure at 5 and 300 K temperatures.

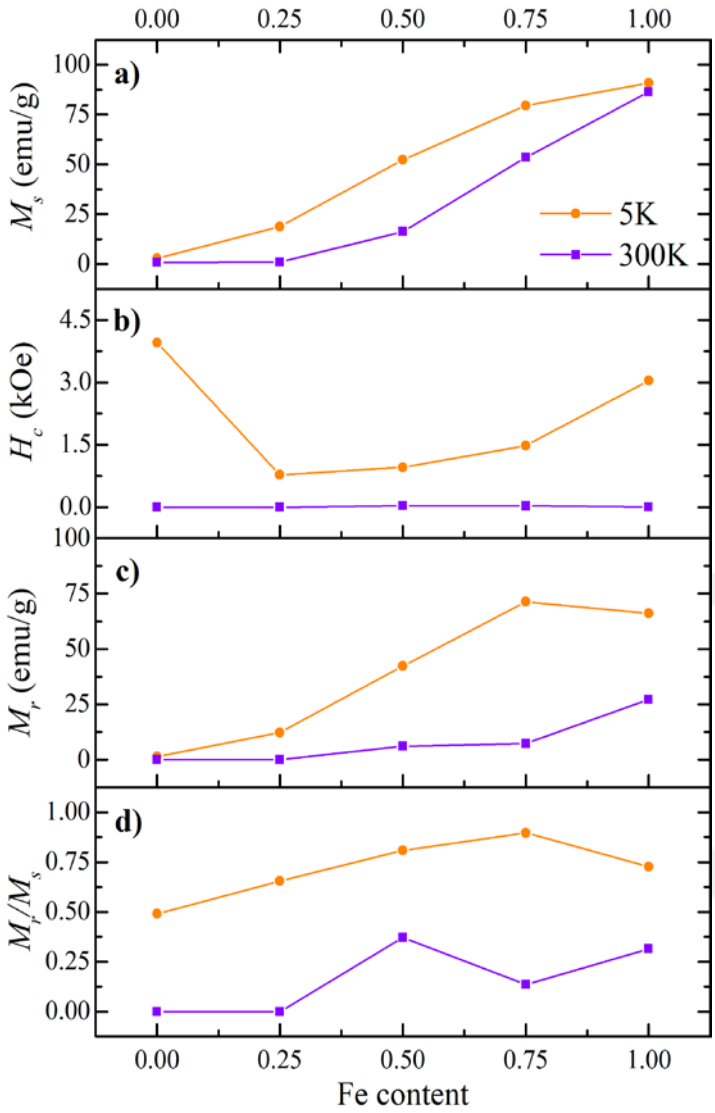

Figure 4.24. Fe concentration as a function of a) coercieve field, b) saturation magnetization, c) remenant magnetization and d) the ratio of remanant magnetization *vs* saturation magnetization in $Co(Cr_{1-x}Fe_x)_2O_4$ spinel material.

4.1.2.3. Isothermal initial curves of $Co(Cr_{1-x}Fe_x)_2O_4$ spinel materials

Isothermal initial curves of $Co(Cr_{1-x}Fe_x)_2O_4$ spinel materials are measured by sweeping magnetic field from 0 to 7 T around samples' magnetic transition temperature region by 4 K temperature steps. Figures 4.25, 4.26 and 4.27 show isothermal initial curves of CCO, CCFO-1 and CCFO-2 samples, respectively. We could not measure isothermal initial curves of CCFO-3 and CFO samples, because the magnetic transition temperatures of them are above our measurement system's limit. In all these figures, the magnetic moment response to applied magnetic field are quite similar that while it suddenly increases with magnetic field at low measurement temperatures, the linear behavior occurs at high measurement temperatures.

It indicates the magnetic property of samples changes from ferromagnetic to paramagnetic when the measurement temperature goes up from critical temperature. Since the magnetic transition temperature range of CCFO-2 sample is higher than other samples, the number of initial curves are more than other samples.

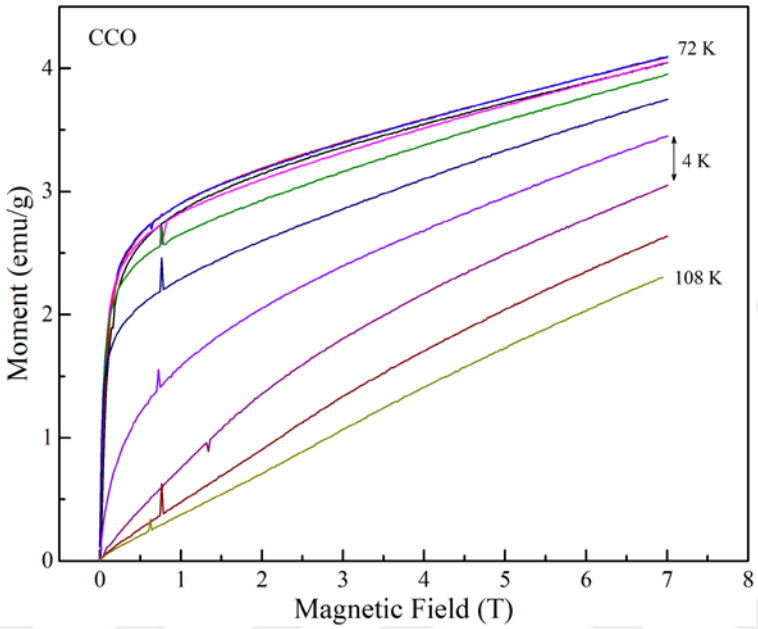

Figure 4.25. Magnetic initial curves of $CoCr_2O_4$ sample at around its transition temperature.

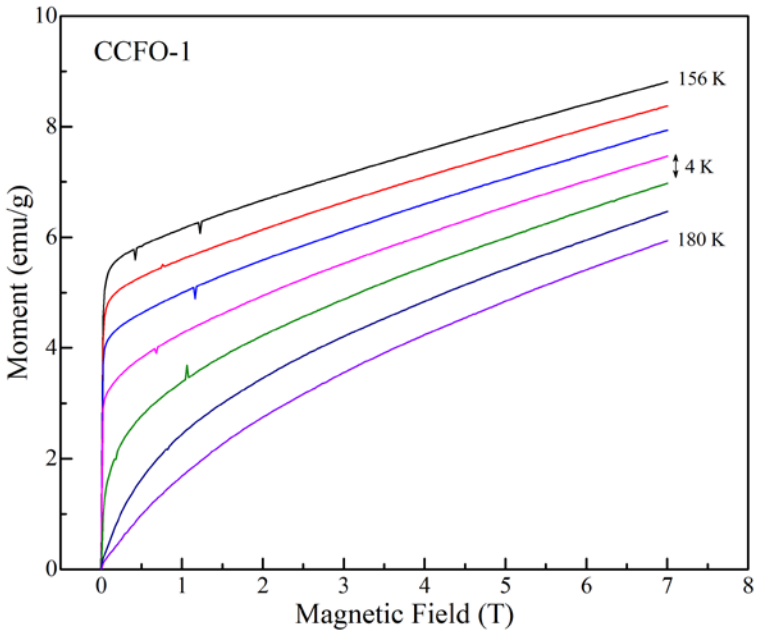

Figure 4.26. Magnetic initial curves of $Co(Cr_{1-x}Fe_x)_2O_4$ sample for x=0.25 at around its transition temperature.

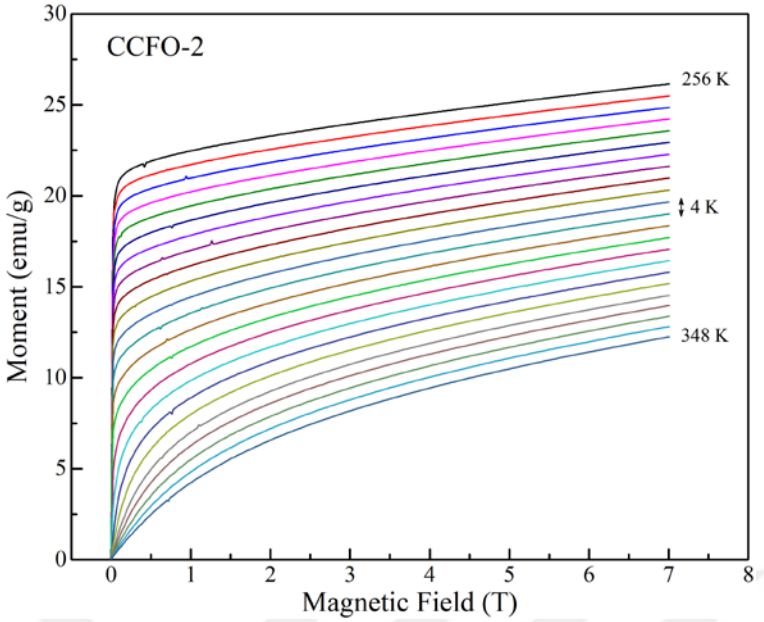

Figure 4.27. Magnetic initial curves of $Co(Cr_{1-x}Fe_x)_2O_4$ sample for x=0.50 at around its transition temperature.

4.1.2.4. Temperature dependent magnetic entropy change of $Co(Cr_{1-x}Fe_x)_2O_4$ spinel materials

Next, we calculated the magnetic entropy change (ΔS_M) as a function of temperature for CCO, CCFO-1 and CCFO-2 samples. The ΔS_M values of samples were calculated by using following thermodynmamic formula;

$$\Delta S_M = \int_0^{H_{max}} \left(\frac{dM}{dT}\right)_H dH \tag{18}$$

where H_{max} is the maximum applied magnetic field. Due to the nature of magnetic materials, the maximum magnetic entropy change can be seen at around magnetic transition temperature. Based on the Eq. (18), initial *M-H* curves measured at around T_C by 4 K steps (see Fig. 4.25, 4.26 and 4.27) were processed at each temperature step. Therefore, temperature dependences of ΔS_M under various applied magnetic field variations for CCO, CCFO1 and CCFO-2 samples were obtained and plotted in Fig. 4.28, Fig. 4.29 and Fig.4.30, respectively. Note that due to temperature limit of our magnetization measurement system, we could not measure initial curves for CCFO-3 and CFO samples. As expected that the maximum ΔS_M values for samples have been observed at around their Curie temperatures under low field variations. As seen from the figures that the ΔS_M values versus temperature curves of all

samples are schematically similar to each other. But the sharp magnetic entropy change in CCO sample becomes wider when Fe is added into the lattice. This is also related to the magnetic transition temperature range that is consistent with *M-T* curves of samples. The maximum magnetic entropy change values of CCO, CCFO-1 and CCFO-2 samples are found as -0.92 J/kgK, -1.26 J/kgK and -1.40 J/kgK under 7 T magnetic field, respectively. It is seen that the maximum magnetic entropy change slightly increases with Fe-content in $CoCr_2O_4$ spinel structure. Therefore, we can conclude that both magnetic transition temperature and magnetic entropy change values can be increased by increasing Fe-content in cobalt-chromite.

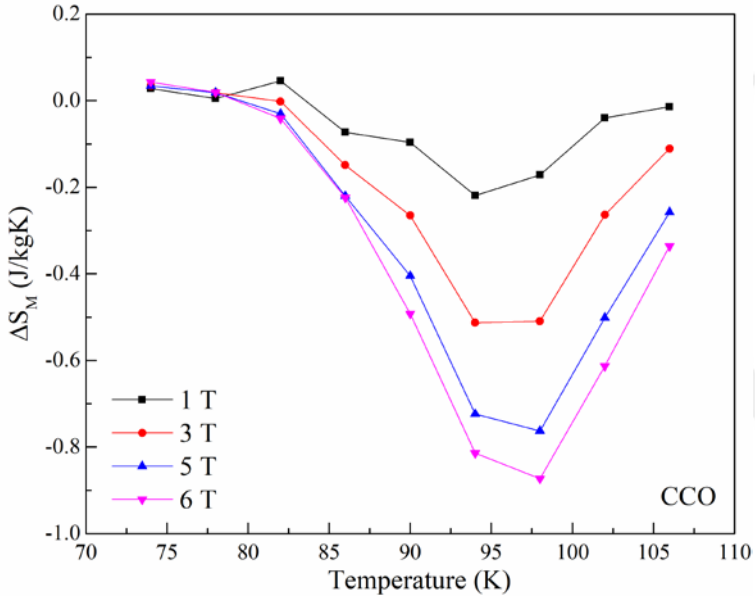

Figure 4.28. The magnetic entropy changes as a function of temperature for CCO sample.

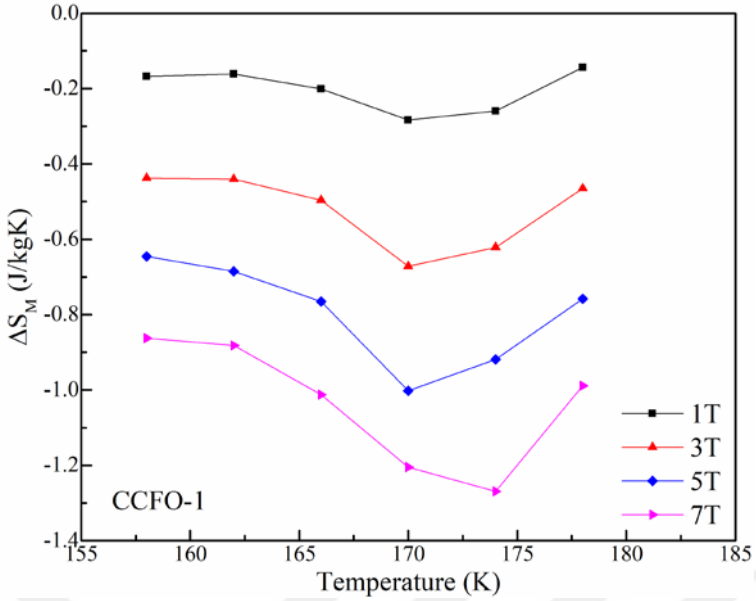

Figure 4.29. The magnetic entropy changes as a function of temperature for CCFO-1 sample.

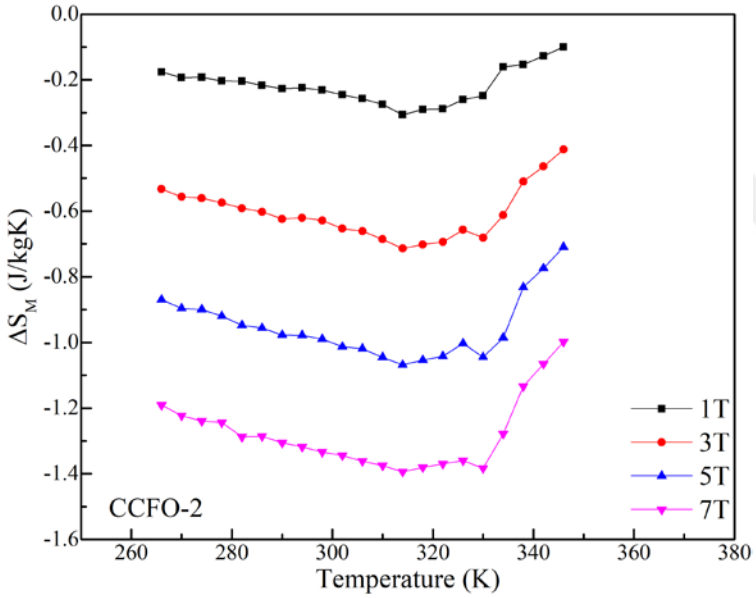

Figure 4.30. The magnetic entropy changes as a function of temperature for CCFO-2 sample.

4.2. Ho-substituted $CoCrFeO_4$ Spinels

In this part of thesis, to study the effect of Ho on the structural, magnetic and magnetocaloric properties of $CoCrFeO_4$ spinel nanoparticles, Ho^{3+} ions at various contents will be substituted with the trivalent ions in the $CoCrFeO_4$ spinel nanoparticles optimized in Section 4.1. The purpose of this work is to determine a suitable material having both a magnetic phase transition occurring around room temperature and tunable magnetic properties for possible magnetism-based applications. As we have already discussed in Chapter 3, various combinations of sample structures were synthesized by sol-gel process. The samples are labelled as given in the Table. 4.4.

Table 4.4. Sample codes and their corresponding chemical formula.

Sample Code	Ho content (%)	Chemical Formula
CHCFO-1	10	$CoHo_{0.10}Cr_{0.95}Fe_{0.95}O_4$
CHCFO-2	20	$CoHo_{0.20}Cr_{0.90}Fe_{0.90}O_4$
CHCFO-3	30	$CoHo_{0.30}Cr_{0.85}Fe_{0.85}O_4$
CHCFO-4	40	$CoHo_{0.40}Cr_{0.80}Fe_{0.80}O_4$

Before working magnetic properties of the produced samples, first structural properties will be discussed in sub-section 4.2.1. After that the magnetic properties of these samples will be discussed in sub-section 4.2.2.

4.2.1. Structural properties of Ho-substituted $CoCrFeO_4$ spinels

4.2.1.1. X-ray diffraction (XRD) analysis of Ho-substituted $CoCrFeO_4$ spinels

The Ho-substituted samples are first characterized by performing XRD measurements. The samples are grinded before the XRD experiment to get fine powder form. XRD spectrum data were collected in a wide range of scanning angle from 20° to 80°. Figure 4.31a-e show the XRD patterns of Ho-substituted $CoCrFeO_4$ spinel samples from 10 to 40% Ho content, respectively. After collecting the XRD data, we have perfomed the data analysis by using High-Score Plus software to determine the crystal phase, lattice parameters, crystallite size and other structural parameters. Based on this analysis, we have observed two identical crystal symmetries which are cubic and orthorhombic structures comes from spinel crystal symmetery and $HoCrO_3$/$HoFeO_3$ labelled as * in the Figure 4.31, respectively. The lattice constant, unit-cell volume, *d*-spacing and crystallite size values of $CoCrFeO_4$ samples are

tabulated in Table 4.5. As seen in this table, all structural paramteres decrease with increasing Ho-content in the sample structure, except the CHCFO-4 sample.

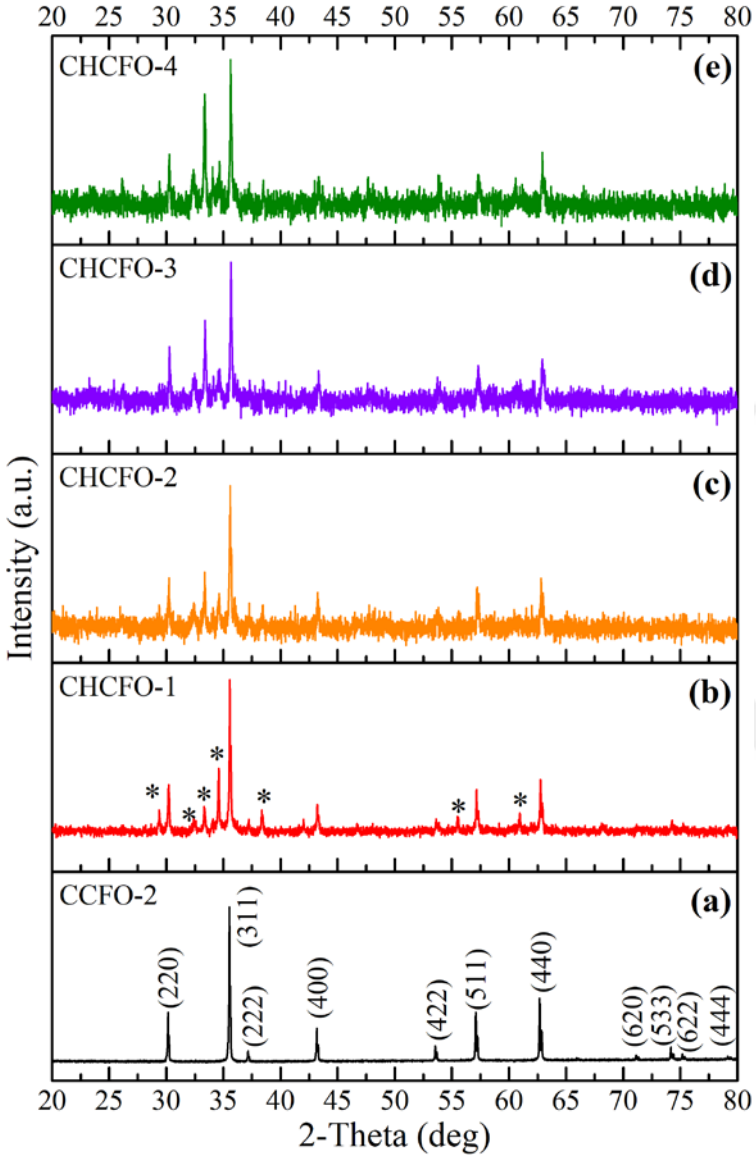

Figure 4.31. XRD patterns of Ho-substituted $CoCrFeO_4$ spinel samples for a) 0%, b) 10%, c) 20%, d) 30% and e) 40% Ho content.

Table 4.5. Structural properties of Ho-substituted $CoCrFO_4$ spinel samples.

Sample Code	Ho content *(%)*	*a* (Å)	V (Å^3)	*d*-spacing value (Å)	*D* (nm)
CCFO-2	00.0	8.374	587.38	2.5250	233.32
CHCFO-1	10.0	8.365	585.29	2.5221	145.61
CHCFO-2	20.0	8.356	583.35	2.5193	103.28
CHCFO-3	30.0	8.342	580.57	2.5153	80.49
CHCFO-4	40.0	8.349	582.09	2.5174	97.09

4.2.1.2. Scanning electron microscopy (SEM) imaging and Energy-dispersive x-ray spectrum (EDS) analysis of Ho-substituted $CoCrFeO_4$ spinels

SEM images of Ho-substituted $CoCrFeO_4$ nanocrystals taken at 15kX and 100kX magnification are presented in Figs. 4.32a-b, Figs. 4.33a-b, Figs. 4.34a-b and Figs. 4.35a-b for CHCFO-1, CHCFO-2, CHCFO-3 and CHCFO-4, respectively. SEM imaging technique allows us to observe grains and their distribution. The grains are uniformly formed and their shapes can be defined as spherical nanocrystal. The grain size distribution for all samples has been determined by taking into account of randomly selected 100 grains in the SEM image and imageJ software. The average grain sizes of nanocrystals are found as 520, 653, 849 and 929 nm for CHCFO-1, CHCFO-2, CHCFO-3 and CHCFO-4, respectively (see Fig.4.32c, Fig.4.33c, Fig.4.34c and Fig.4.35c). The average grain size increaes with increasing Ho^{3+} content in $CoCrFeO_4$ spinel structure. This is consistent with the XRD spectrum that $HoCrO_3$/$HoFeO_3$ peaks are getting stronger when Ho-content is increased.

The EDS spectrum of Ho-substituted $CoCrFeO_4$ samples are shown in Fig.4.32d, Fig.4.33d, Fig.4.34d and Fig.4.35d for CHCFO-1, CHCFO-2, CHCFO-3 and CHCFO-4, respectively. As it can be seen that the EDS spectrum shows just our compounds element without any impurity. Insets of Fig.4.32d, Fig.4.33d, Fig.4.34d and Fig.4.35d show the weight and atomic percentage of each element in the compounds. The chemical composition determined from energy-dispersive x-ray spectroscopy analysis is consisted with the nominal compositions. The expected and EDS atomic percentage values are tabulated in Table 4.6.

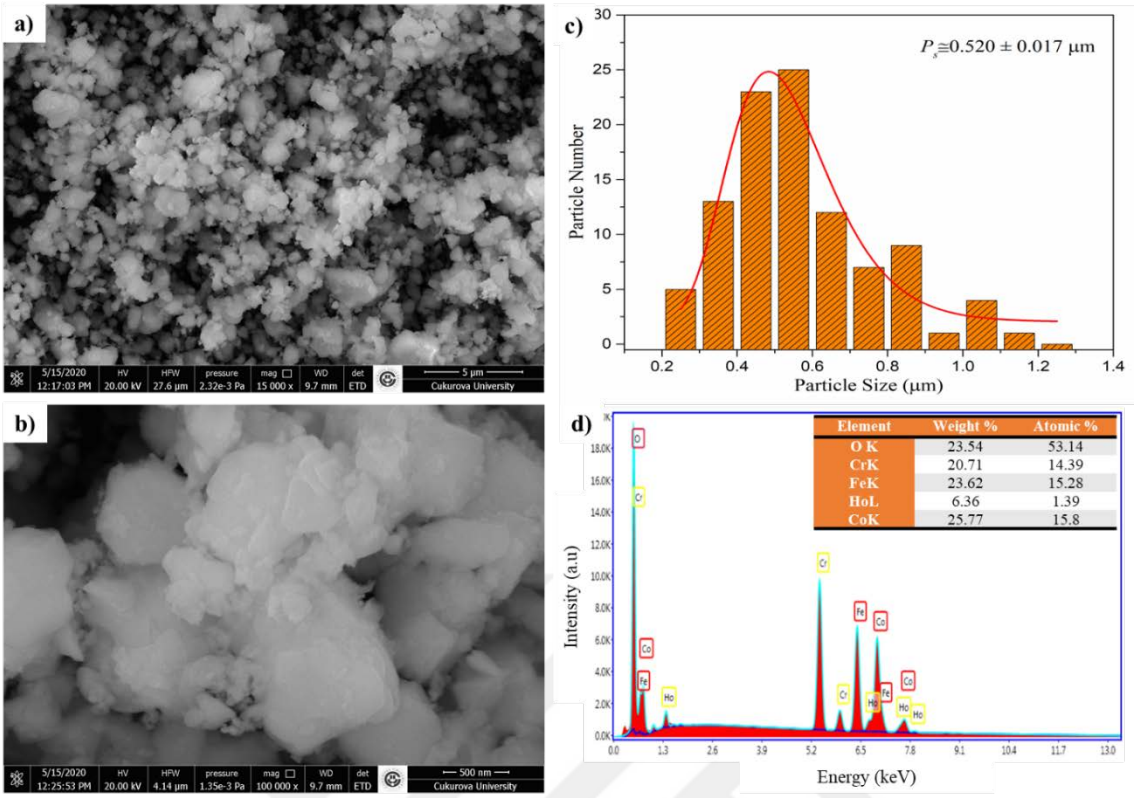

Figure 4.32. CHCFO-1 sample's; a-b) SEM images, c) particle size distribution and d) EDS spectrum. Inset of c) Atomic and weight percentage of elements.

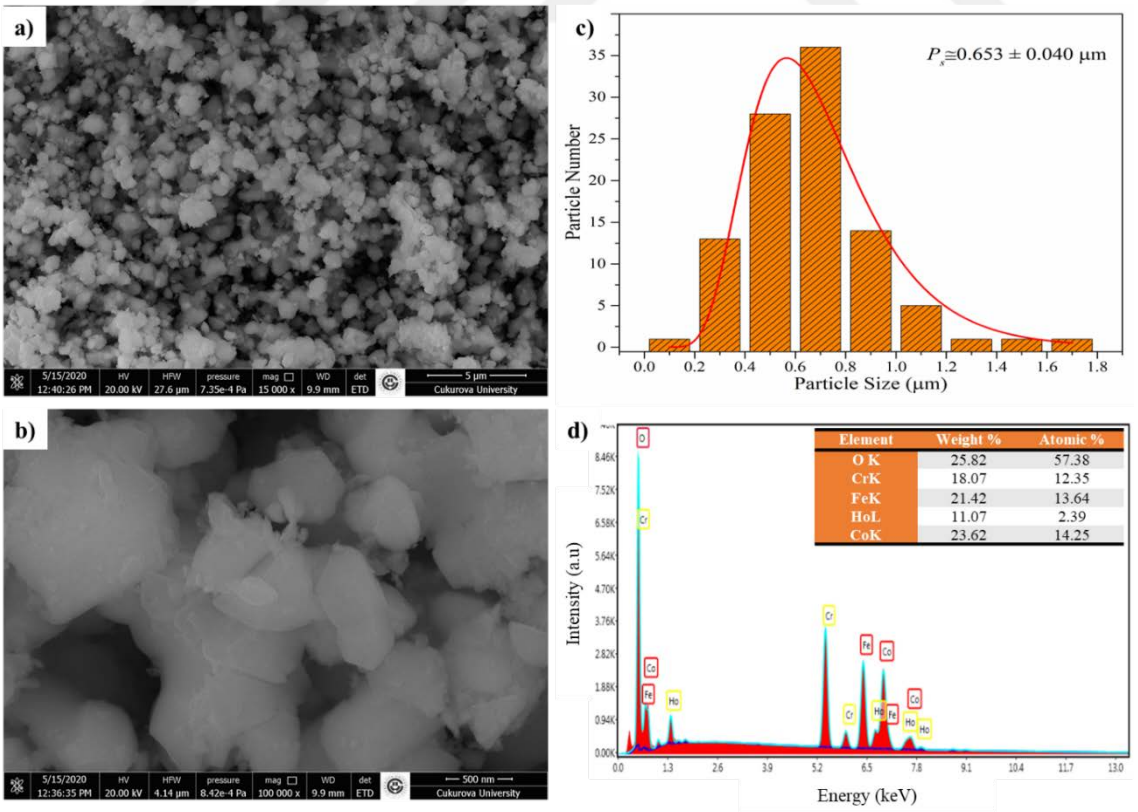

Figure 4.33. CHCFO-2 sample's; a-b) SEM images, c) particle size distribution and d) EDS spectrum. Inset of c) Atomic and weight percentage of elements.

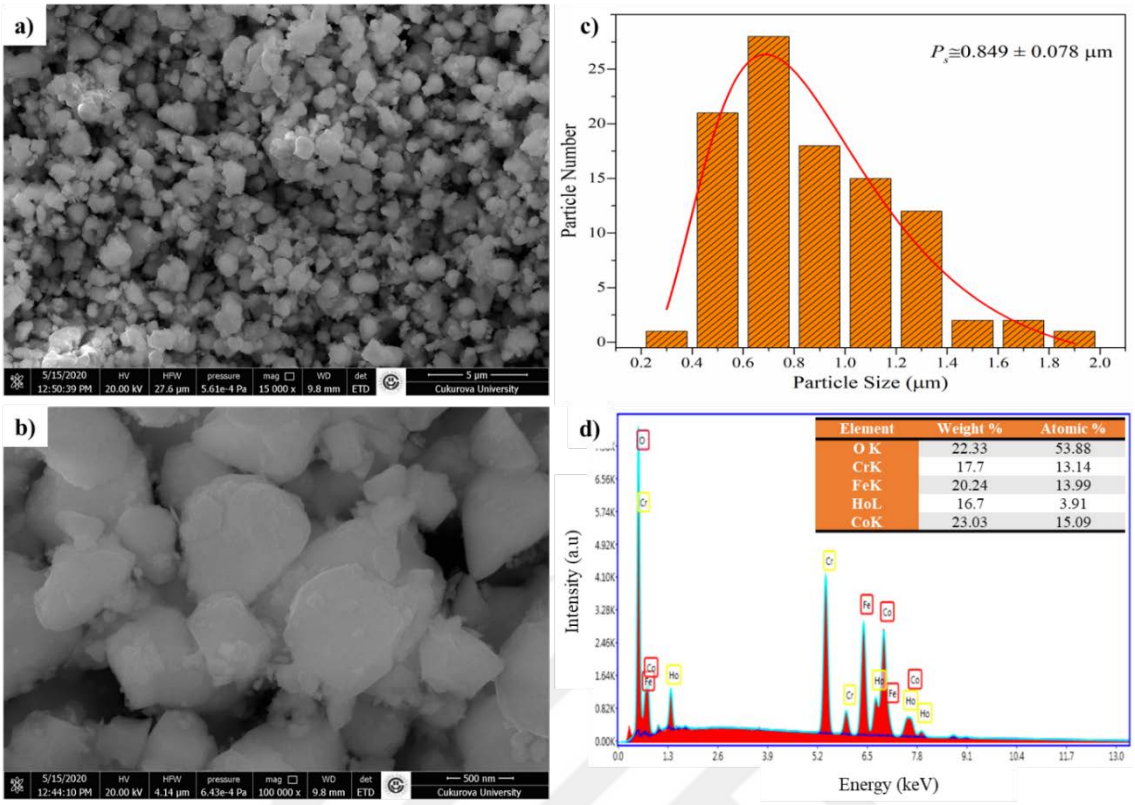

Figure 4.34. CHCFO-3 sample's; a-b) SEM images, c) particle size distribution and d) EDS spectrum. Inset of c) Atomic and weight percentage of elements.

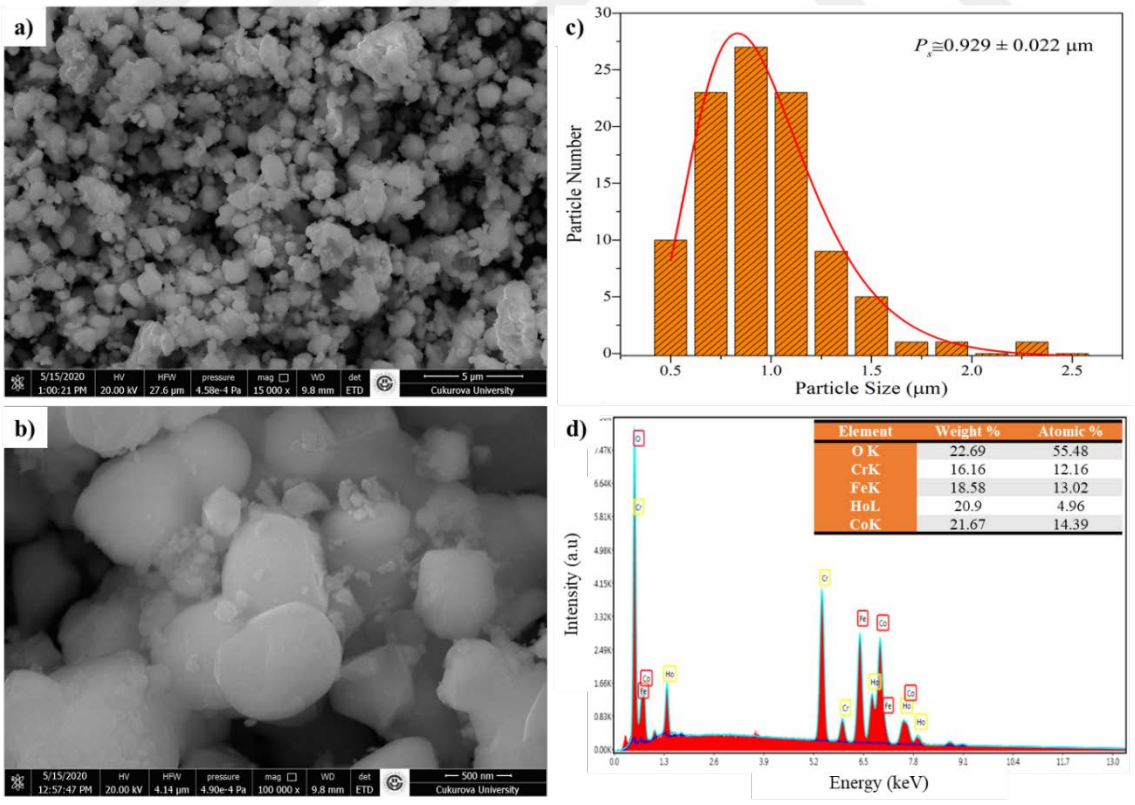

Figure 4.35. CHCFO-4 sample's; a-b) SEM images, c) particle size distribution and d) EDS spectrum. Inset of c) Atomic and weight percentage of elements.

Table 4.6. The expected and EDS results of atomic percent of each element in Ho-substituted $CoCrFeO_4$ spinel materials.

Sample Code	Expected					EDS Results				
	Co	Cr	Fe	Ho	O	Co	Cr	Fe	Ho	O
CHCFO-1	1.00	0.95	0.95	0.10	4.00	1.11	1.01	1.07	0.10	3.72
CHCFO-2	1.00	0.90	0.90	0.20	4.00	1.00	0.86	0.95	0.17	4.02
CHCFO-3	1.00	0.85	0.85	0.30	4.00	1.06	0.92	0.98	0.29	3.77
CHCFO-4	1.00	0.80	0.80	0.40	4.00	1.01	0.85	0.91	0.37	3.88

4.2.2. Magnetic properties of Ho-substituted $CoCrFeO_4$ spinel materials

4.2.2.1. Temperature dependence of magnetic properties of Ho-substituted $CoCrFeO_4$ spinel materials

Magnetic properties of Ho-substituted $CoCrFeO_4$ samples are first studied by temperature sweeping moment measurement in both zero-field-cooled (ZFC) and field-cooled (FC) conditions in the range of 5 – 380 K with an applied of 100 Oe. In ZFC magnetization measurement, the samples were cooled from room temperature to 5 K with zero field and after stabilization of temperature, then moment data were recorded when samples were warming with a field of 100 Oe. In the FC mode, a field of 100 Oe was applied then samples were cooled down from room temperature to 5 K and moment data were recorded when cooling in the same field. Figures 4.36, 4.37, 4.38 and 4.39 show the temperature dependence of magnetic moment of CHCFO-1, CHCFO-2, CHCFO-3 and CHCFO-4 samples, respectively. The magnetic transition temperatures of CHCFO-1, CHCFO-2, CHCFO-3 and CHCFO-4 samples are found as 327, 334, 344 and 330 K, respectively. The increament in T_C indicates that some Cr atoms crystallizes with Ho and O to create $HoCrO_3$ as we observed in Figs. 4.31.

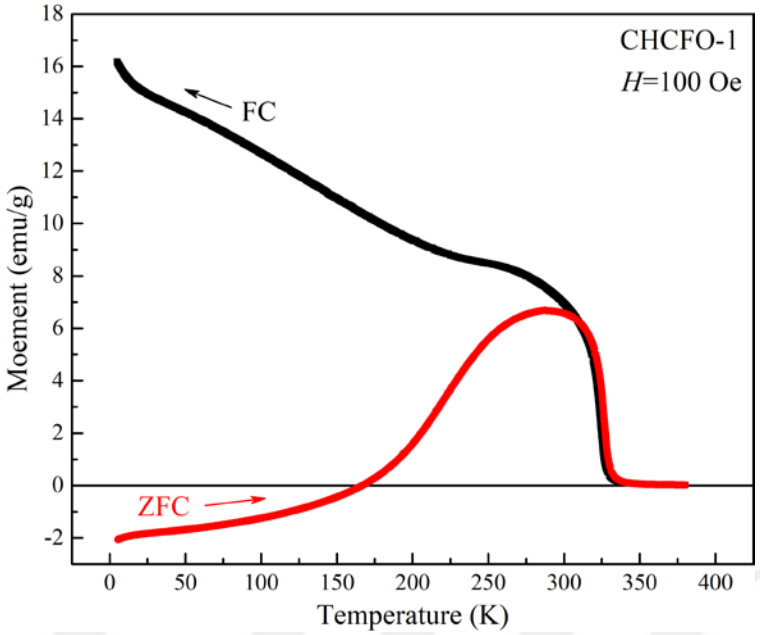

Figure 4.36. Temperature dependence of magnetic moment of CHCFO-1 sample.

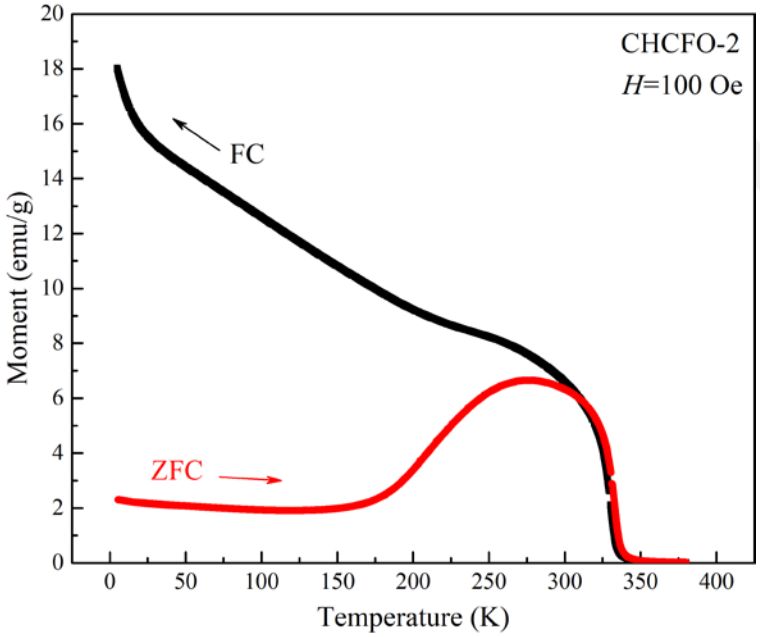

Figure 4.37. Temperature dependence of magnetic moment of CHCFO-2 sample.

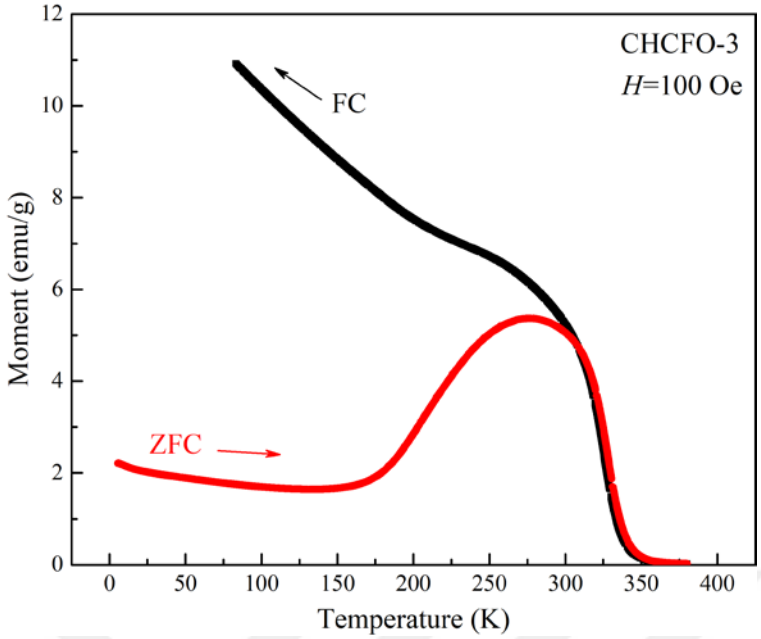

Figure 4.38. Temperature dependence of magnetic moment of CHCFO-3 sample.

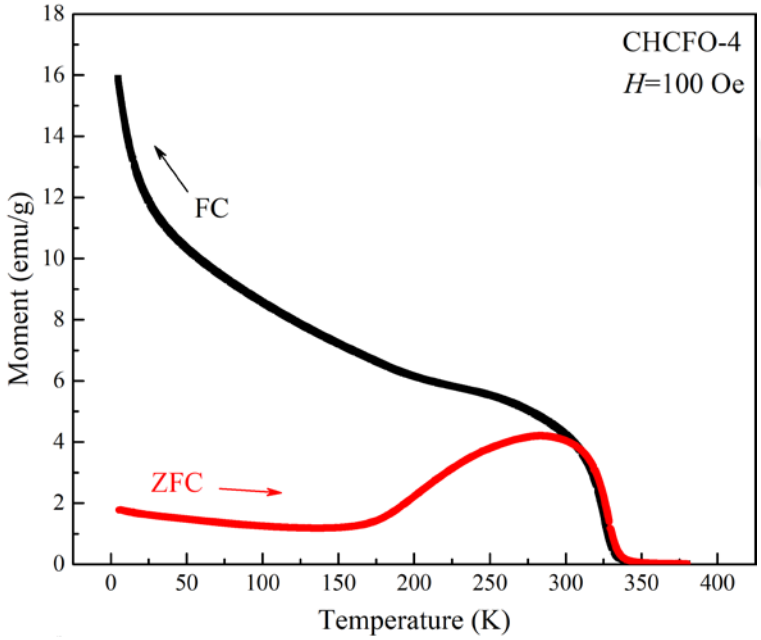

Figure 4.39. Temperature dependence of magnetic moment of CHCFO-4 sample.

4.2.2.2. Magnetic hysteresis of Ho-substituted $CoCrFeO_4$ spinel materials

The magnetic hysteresis (*M-H*) measurements were performed by sweeping applied field at low (5 K) and room temperature (300 K) for all samples. For low temperature measurements, we cooled samples without applying magnetic field. Then, magnetic field is applied to the samples at constant ramping.

Figures 4.40 and 4.41 show magnetic hysteresis curve of CHCFO-1 sample measured at 5 and 300 K, respectively. The full hysteresis curve indicates that the CHCFO-1 sample is ferromagnetically coupled at low temperature. This behavior is consistent with the *M-T* curve as shown in Figure 4.36. The H_c, M_s, M_r and M_r/M_s values are tabulated in Table 4.7. Since the sample has paramagnetic contribution, CHCFO-1 sample could not exactly sature at 5 K. Due to this unsature situation, the M_s value is extracted from the point to be that the applied field is 3 T. The coercieve field becomes almost zero at room temperature. The saturation magnetization is increased from 52.59 emu/g to 54.82 emu/g when 10% Ho-substituted into the lattice. See all magnetic parameters in Table 4.7.

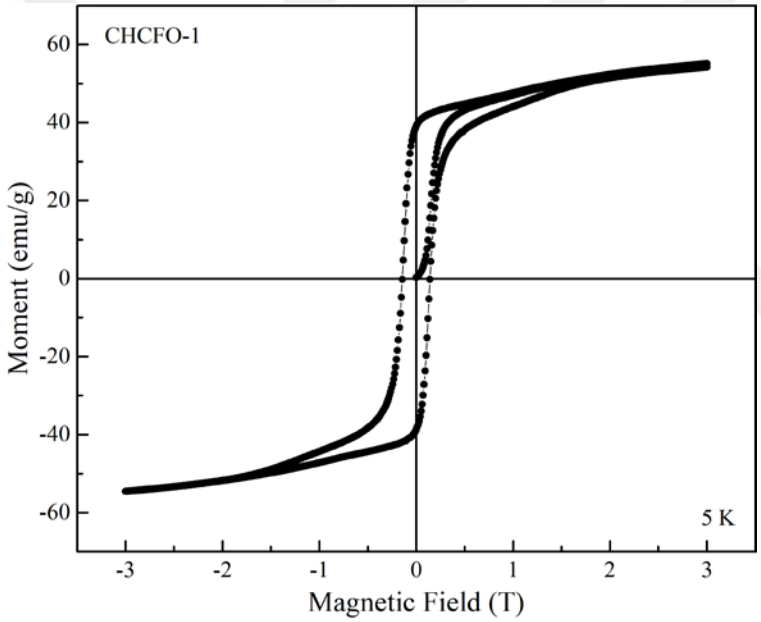

Figure 4.40. Magnetic hysteresis curve of CHCFO-1 sample at 5 K.

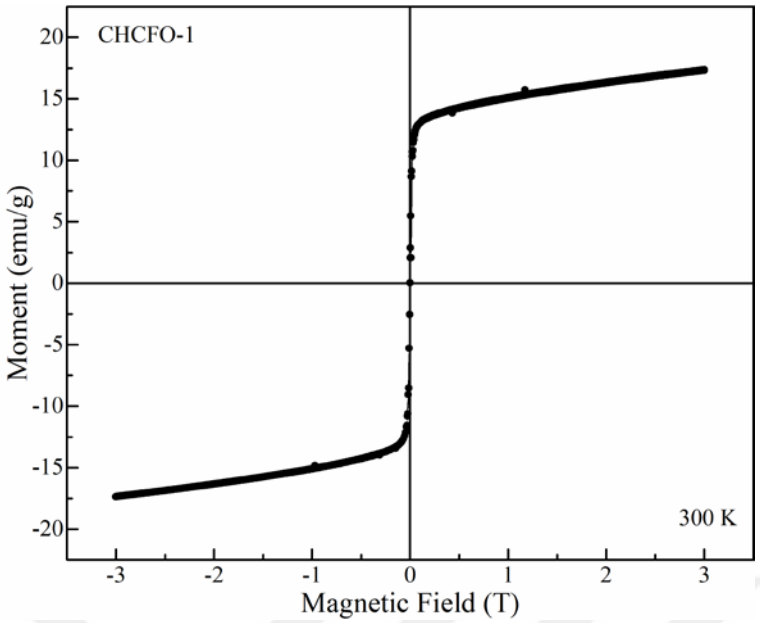

Figure 4.41. Magnetic hysteresis curve of CHCFO-1 sample at 300 K.

Figures 4.42 and 4.43 indicate CHCFO-2 sample's magnetic hysteresis curves measured at 5 and 300 K, respectively. These curves are quite similar with CHCFO-1 sample. The paramagnetic contiribution becomes larger when Ho-substituted in the main lattice. In addition, saturation magnetization decreases when Ho content is increased.

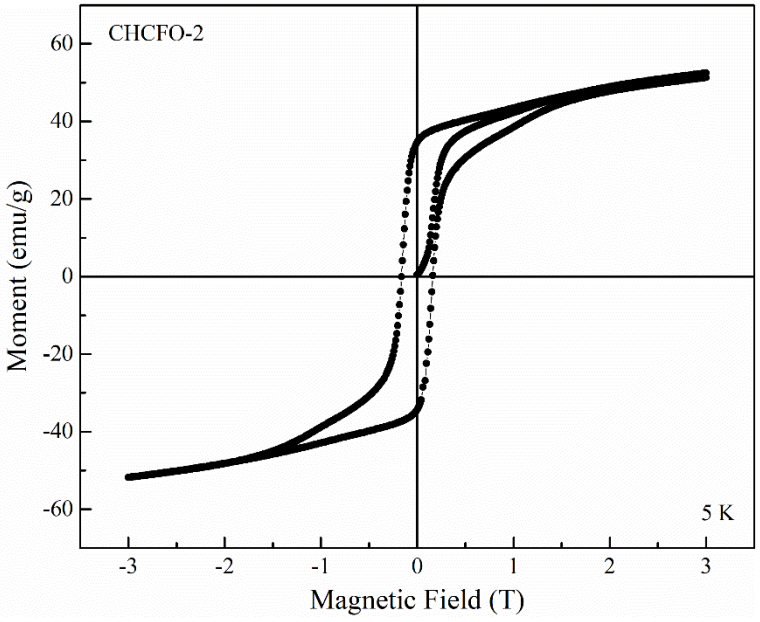

Figure 4.42. Magnetic hysteresis curve of CHCFO-2 sample at 5 K.

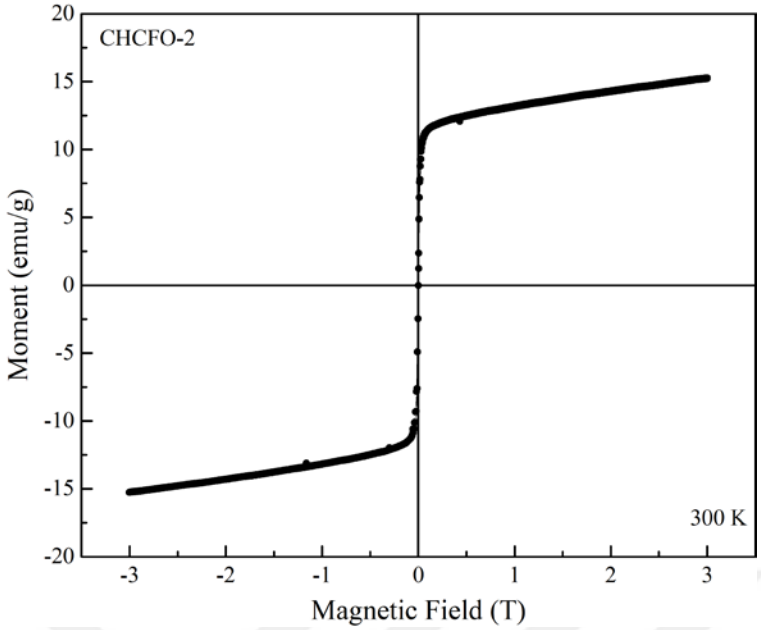

Figure 4.43. Magnetic hysteresis curve of CHCFO-2 sample at 300 K.

Figures 4.44 and 4.45 show CHCFO-3 sample's magnetic hysteresis curves measured at 5 and 300 K, respectively. As it can be seen that the hysteresis trend of both CHCFO-2 and CHCFO-3 samples, but the M_s value continues to decrease with Ho-content.

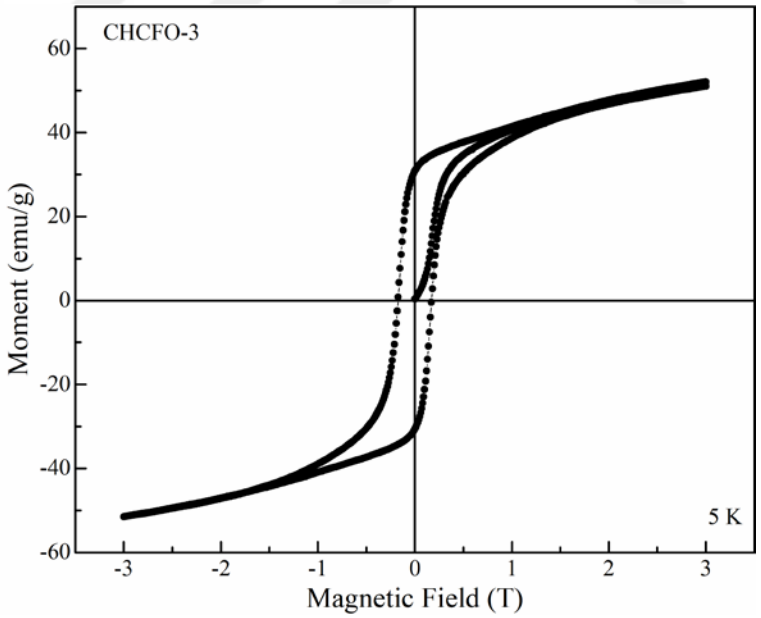

Figure 4.44. Magnetic hysteresis curve of CHCFO-3 sample at 5 K.

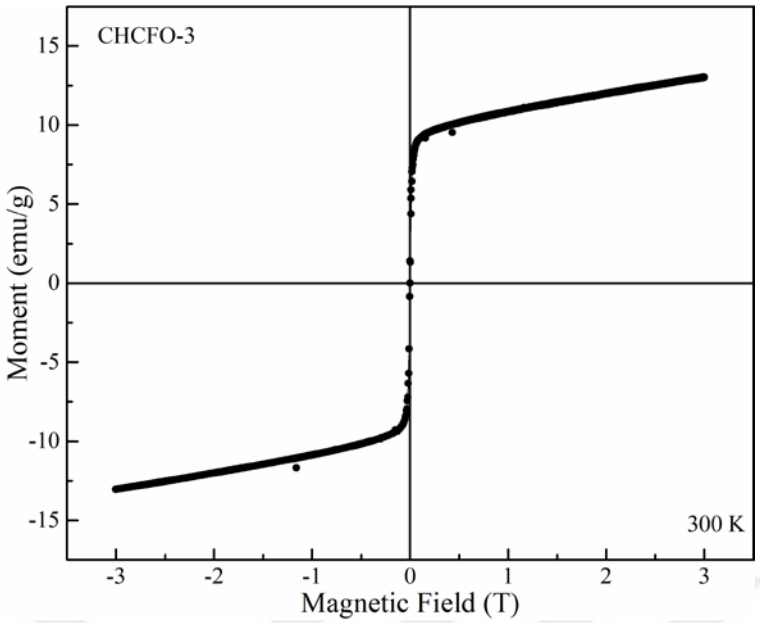

Figure 4.45. Magnetic hysteresis curve of CHCFO-3 sample at 300 K.

Figures 4.46 and 4.47 show CHCFO-4 sample's magnetic hysteresis curves measured at 5 and 300 K, respectively. In CHCFO-4 sample, we observed an increament in M_s value at low temperature experiment. Thi increament might be explained the formation of $HoFeO_3$ phases in the XRD spectrum. The $HoFeO_3$ crystal phase might be increased in the lattice which is also supported by the reduction in T_c value of CHCFO-4 sample implies a decreament Fe content in $CoCrFeO_4$.

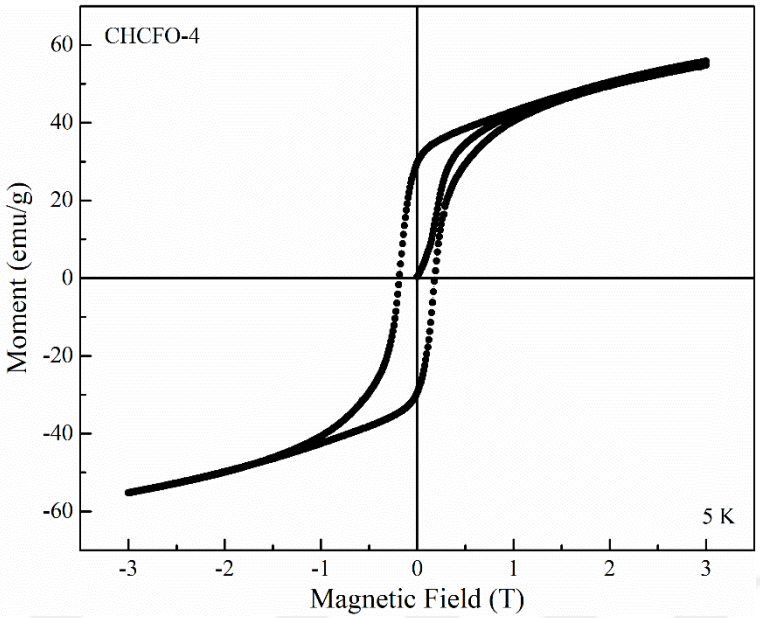

Figure 4.46. Magnetic hysteresis curve of CHCFO-4 sample at 5 K.

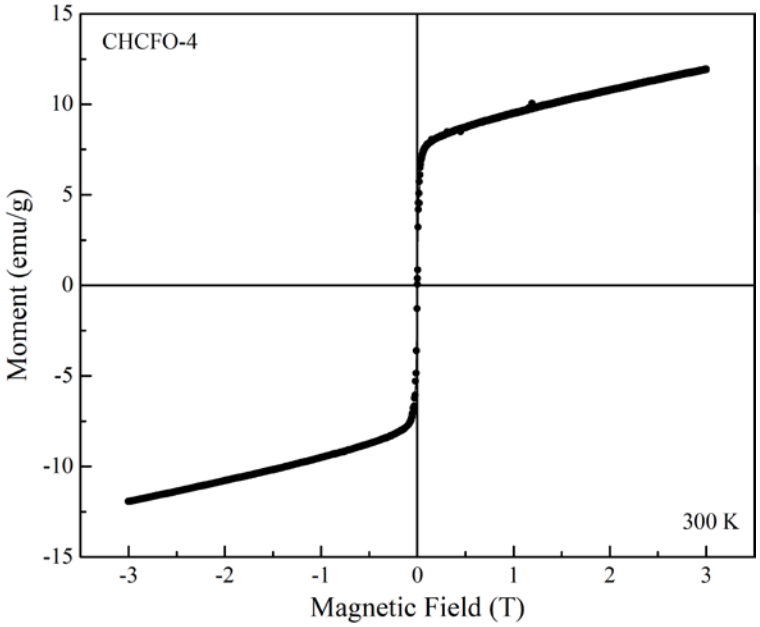

Figure 4.47. Magnetic hysteresis curve of CHCFO-4 sample at 300 K.

Table 4.7. The magnetic parameters of Ho-substituted $CoCrFeO_4$ samples.

Sample Code	T_c (K)	H_c (Oe)		M_s (emu/g)		M_r (emu/g)		M_r/M_s	
		5K	300K	5K	300K	5K	300K	5K	300K
CHCFO-1	327	1292	-	54.82	17.55	39.17	1.05	0.715	0.059
CHCFO-2	334	1611	-	52.13	15.33	35.73	0.46	0.685	0.030
CHCFO-3	344	1755	-	51.53	13.07	31.52	0.23	0.612	0.046
CHCFO-4	330	1899	-	55.18	12.03	30.74	0.045	0.557	0.003

4.2.2.3. Isothermal initial curves of Ho-substituted $CoCrFeO_4$ spinel materials

Isothermal initial curves of Ho-substituted $CoCrFeO_4$ spinel materials are measured by sweeping magnetic field from 0 to 7 T around samples' magnetic transition temperature region by 4 K temperature steps. Figures 4.48, 4.49, 4.50 and 4.51 show isothermal initial curves of CHCFO-1, CHCFO-2, CHCFO-3 and CHCFO-4 samples, respectively. In all these figures, the magnetic moment response to applied magnetic field are quite similar that while it suddenly increases with magnetic field at low measurement temperatures, the linear behavior occurs at high measurement temperatures. It indicates the magnetic property of samples changes from ferromagnetic to paramagnetic when the measurement temperature goes up from critical temperature.

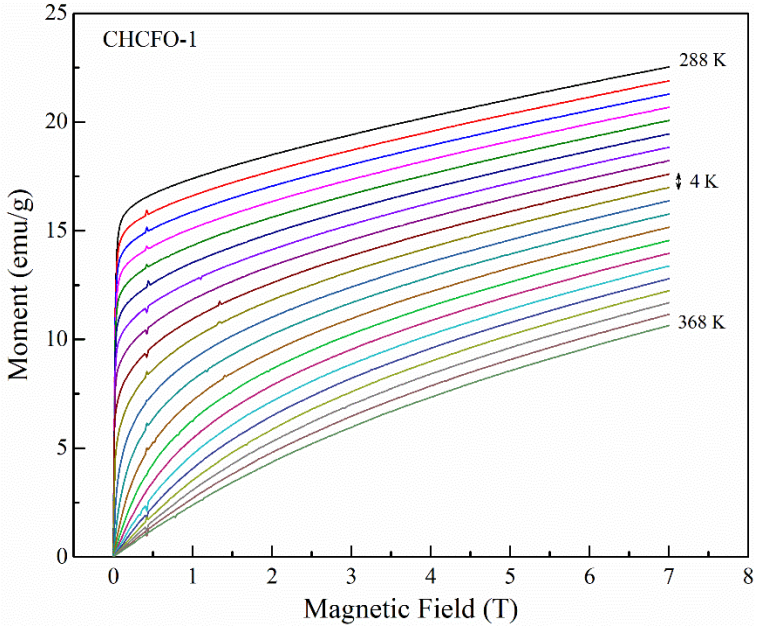

Figure 4.48. Magnetic initial curves of CHCFO-1 sample at around its transition temperature.

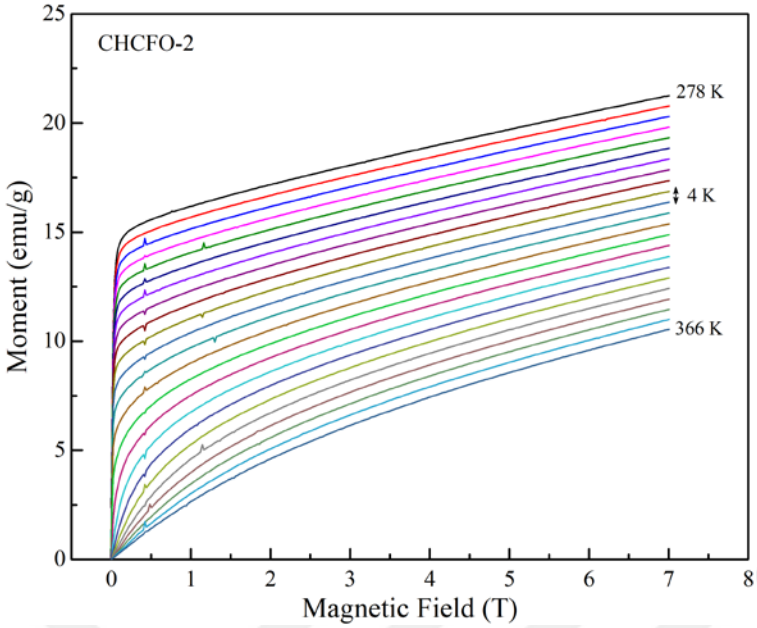

Figure 4.49. Magnetic initial curves of CHCFO-2 sample at around its transition temperature.

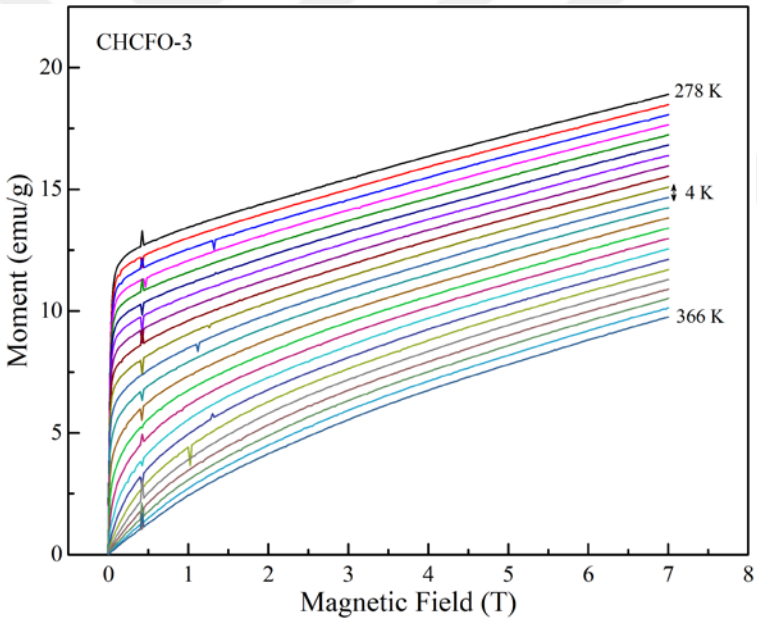

Figure 4.50. Magnetic initial curves of CHCFO-3 sample at around its transition temperature.

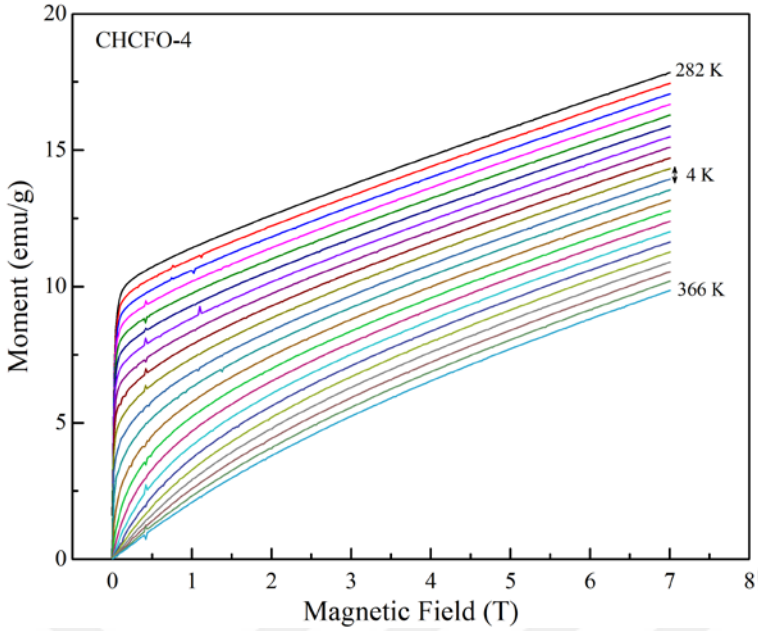

Figure 4.51. Magnetic initial curves of CHCFO-4 sample at around its transition temperature.

4.2.2.4. Temperature dependent magnetic entropy change of Ho-substituted $CoCrFeO_4$ spinel materials

As similar as we have calculated the magnetic entropy change in Section 4.1.2.4, here, the magnetic entropy change as a function of temperature values are extracted from isothermal initial curves by using thermodynamic relation (see Eq.18). The ΔS_M as a function of temperature for CHCFO-1, CHCFO-2, CHCFO-3 and CHCFO-4 samples are shown in Figures 4.52, 4.53, 4.54 and 4.55, respectively. Here, we determined ΔS_M values under 1T, 3T, 5T and 7 T magnetic fields. As it can be seen from these curves that all curves are similar shape. Figure 4.56 shows the magnitude of magnetic entropy change as a function of Ho content in $CoCrFeO_4$ spinel structure. The magnitude of ΔS_M first increases when Ho is substituted in the structure, but then it starts to decrease with increasing Ho^{3+} ions content in $CoCrFeO_4$ spinel structure.

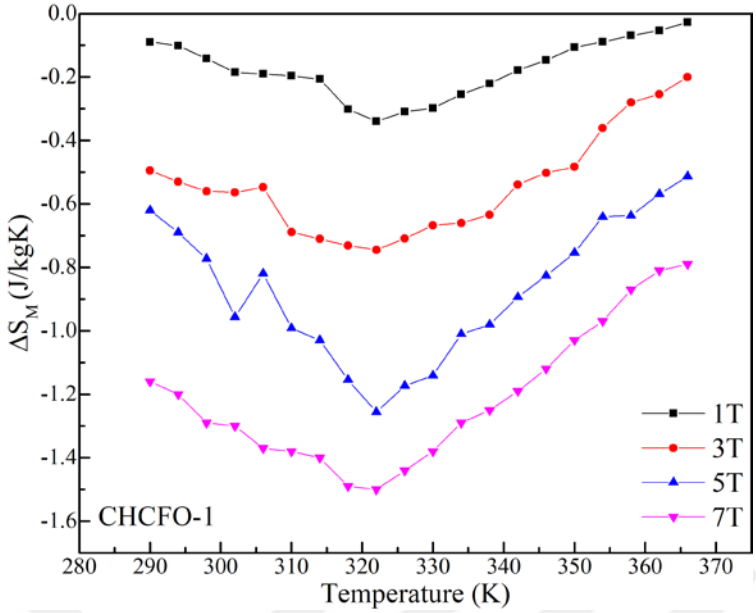

Figure 4.52. The magnetic entropy changes as a function of temperature for CHCFO-1 sample.

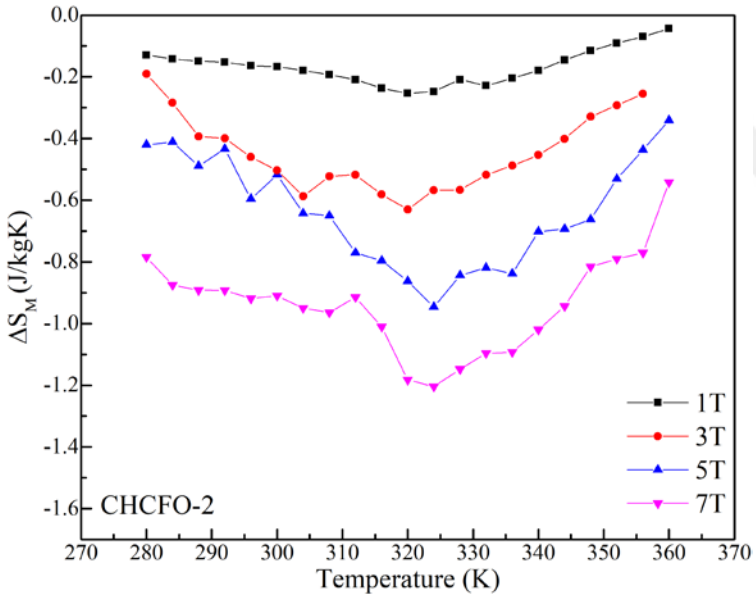

Figure 4.53. The magnetic entropy changes as a function of temperature for CHCFO-2 sample.

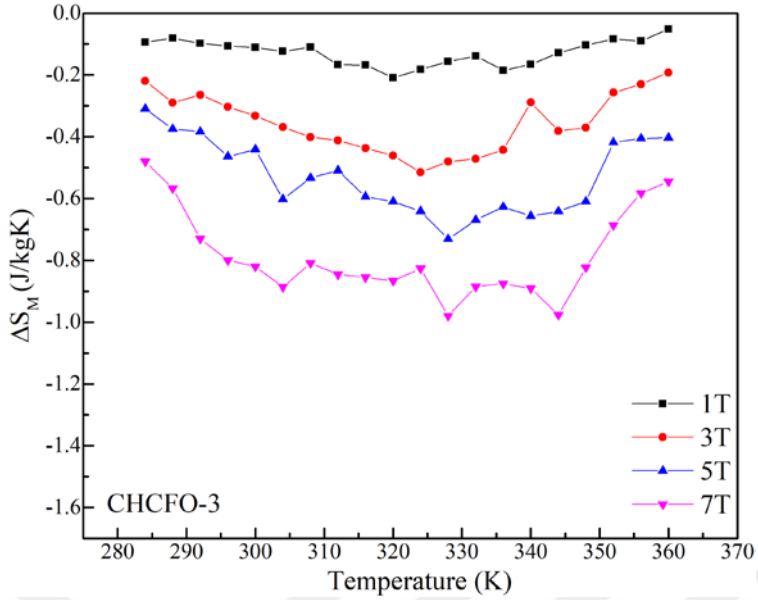

Figure 4.54. The magnetic entropy changes as a function of temperature for CHCFO-3 sample.

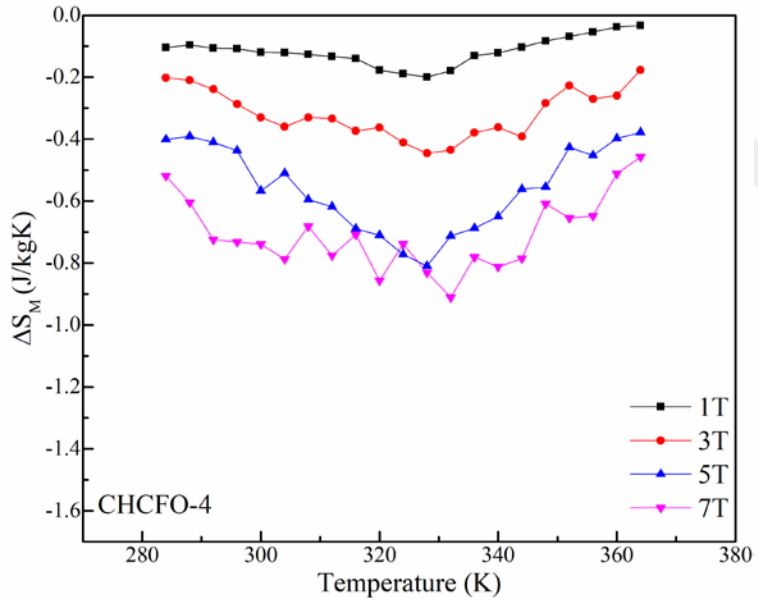

Figure 4.55. The magnetic entropy changes as a function of temperature for CHCFO-4 sample.

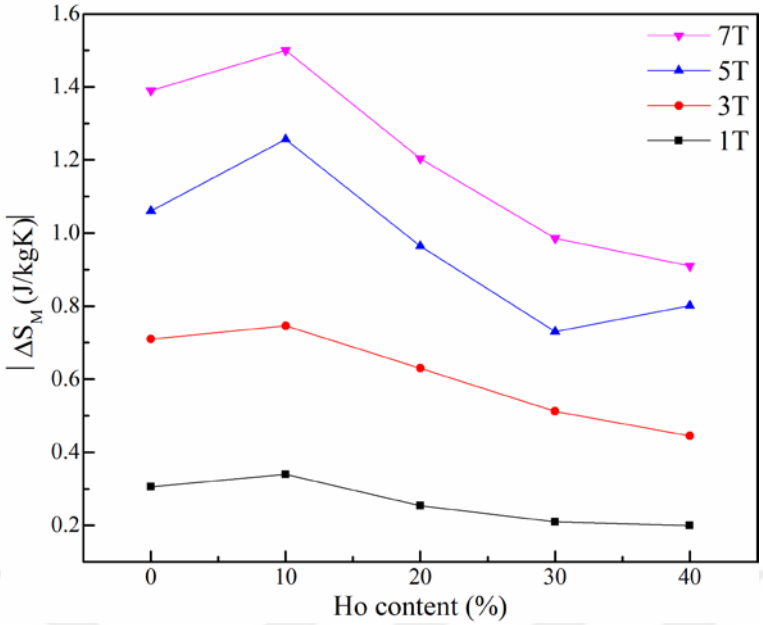

Figure 4.56. Magnitude of magnetic entropy change versus Ho content in $CoCrFeO_4$ spinel structure.

5. CONCLUSIONS

In the scope of the thesis, firstly, structural, magnetic and magnetocaloric properties of Co $(Cr_{1-x}Fe_x)_2O_4$ (x = 0.0, 0.25, 0.50, 0.75, 1.0) spinel multiferroic materials were synthesized by sol-gel method. Here, the effects of Fe substitution with Cr ions on structural, magnetic and magnetocaloric properties of the material were investigated. Then, the optimized sample was substituted with Ho^{3+} ions at various concentration. The structural, magnetic and magnetocaloric properties of the Ho-substituted compounds were investigated through this thesis.

All samples are synthesized by the sol-gel method which is a chemical reaction process. Samples obtained after synthesis were burned at 500 ºC for 1 hour and then it is calcined at 550 ºC for 5 hours. Calcined samples were ground for a total of 1 hour. Cylindrical tablets with a diameter of 10 mm were obtained by applying 15 bar pressure with hydraulic press to the ground samples. The prepared tablets were sintered in an oven at 1100 ºC for 24 hours in the air environment and the materials were made ready for measurement.

For structural analysis of the produced compounds, XRD experiment was used to determine the crystal structure and lattice parameters, SEM imaging technique was used to examine the surface morphology and to determine the particle size distributions, and EDS measurement was performed to determine the elements in the components and the amounts of these elements. For magnetic properties, in order to determine the magnetic transition temperatures, *M(T)* measurements were made in FC and ZFC processes at low field value (100 Oe). Saturation magnetization, remenant magnetization and coercive field values were obtained from magnetic hysteresis measurements performed at both low temperature (5K) and room temperature. In addition, in order to determine magnetic entropy change values, isothermal magnetization measurements *M(H)* at different temperature values were analyzed near T_C temperature values and the results obtained were analyzed.

In the first bunch of sample stacks, we have optimized some physical properties of cobalt-based spinel multiferroic samples. Fe-substitution with Cr ions does not disrupt and change the crystal properties of Co-based spinel because of its similar crystal properties. And we

could not see any impurity phase in the XRD spectra. But, we determined that the lattice parameter increases with increasing Fe content in Co $(Cr_{1-x}Fe_x)_2O_4$ spinel lattice. This is related to the bigger ionic size of Fe^{3+} than Cr^{3+} ions. In addition to XRD analysis, the SEM images taken at various magnifications indicate that grains form as a cubic shape when x=0 and they become spherical when x is increased in the lattice. Finally, the grain shape becomes worst in $CoFe_2O_4$ sample. The average particle size determined from randomly selected 100 particles in the SEM images by using imageJ software. Particle size distribution of the samples show that the average particle size increases with increasing Fe content in the Co-based spinel lattice. The elemental analysis performed by EDS measurements indicates that all samples are good agreement with our desired atomic/weight percent. In addition, we could not see any impurity element in the EDS spectrum. The magnetic transition temperature from ferromagnetic to paramagnetic was determined from *M-T* curves that show the T_c values of samples increases with Fe content. Since we can heat the sample up to 380 K because of our VSM system's temperature limit, we could not determine the magnetic transition temperature for x=0.75 and 1.00 samples. T_c values are found as 95, 170 and 315 K, for CCO, CCFO-1 and CCFO-2 samples, respectively. The saturation magnetization and remenant magnetization increases with increasing Fe content in the main spinel lattice. Due to ferromagnetic coupling in Fe ions, we observed a strong enhancement in magnetization with Fe content. Finally, we calculated magnetic entropy change from the isothermal magnetization curves measured around magnetic transition temperature. The maximum magnetic entropy changes under 7 T magnetic field were calculated as -0.87, -1.205 and -1.394 J/kgK for CCO, CCFO-1 and CCFO-2 samples, respectively. The overall experimental and theoretical calculations indicate that the optimum compound is $CoCrFeO_4$ due to its considerable high magnetization values, having room temperature magnetic transition temperature and highest magnetic entropy change compared to other samples for practical applications.

Next, the the trivalent ions in the optimized $CoCrFeO_4$ sample were substituted with Ho^{3+} ions which has the highest free magnetic moment in the periodic table. In this bunch, Ho^{3+} ions are substituted from 10 to 40% into the $CoCrFeO_4$ sample structure. The obtained samples were studied by performing similar experiment that we used in the first bunch of samples. In XRD spectrum, we observed two crystal symmetries corresponding to cubic $CoCrFeO_4$ and orthorhombic $HoCrO_3$/$HoFeO_3$ structures. The intensitiy of $HoCrO_3$/$HoFeO_3$ peaks increase with Ho-content. The lattice parameter, unit-cell volume, *d*-spacing value and

crystallite size of $CoCrFeO_4$ decrease with Ho-contetn, except CHCFO-4 sample. The particle size distributions Show that average particle size increases with Ho-content. The EDS spectrums indicate that all samples are good agreement with our desired atomic/weight percent of each element. And we could not see any impurity element in these spectrums. The magnetic measurements show that the magnetic transition temperaure and coercieve field increase with Ho content up to 30% and it reduces in 40% Ho content. In addition, the M_s, M_r and M_r/M_s decrese with Ho content, except CHCFO-4 sample. The maximum magnetic entropy changes under 7 T magnetic field were calculated as -1.394 J/kgK, -1.509 J/kgK, -1.204 J/kgK, -0.986 J/kgK and -0.910 J/kgK for CCFO-2 (Ho-free), CHCFO-1, CHCFO-2, CHCFO-3 and CHCFO-4 samples, respectively. The overall experimental and theoretical calculations indicate that the optimum compound is CHCFO-1 sample due to its considerable high magnetization values, having room temperature magnetic transition temperature and highest magnetic entropy change compared to other samples for practical applications.

6. RECOMMENDATIONS

The structural, magnetic and magnetocaloric properties of $Co(Cr_{1-x}Fe_x)_2O_4$ (x = 0.0, 0.25, 0.50, 0.75, 1.0) spinel multiferroic materials produced by sol-gel method were investigated in this thesis. Fe^{3+} ions were added to $CoCr_2O_4$ spinel structure to replace Cr^{3+} ions to optimize the magnetic transition temperature and magnetic entropy change. The magnetic transition temperature of $CoCr_2O_4$ seen at 95 K was increased to 320 K for x=0.5 value of Fe in main structure. The maximum magnetic entropy change (−1.394 J/kgK) was also observed at this Fe concentration (x=0.5). In addition, the trivalent ions in the optimum $CoCrFeO_4$ sample were substituted with Ho^{3+} rare-earth ions and their structural, magnetic and magnetocaloric properties were examined, where Ho concentrations are in a range of 10-40% in 10% steps. When the Ho is substituted into the main structure, new crystals ($HoCrO_3$ and $HoFeO_3$) were formed. Due to these crystallization, the Cr and Fe amount were changed in spinel structure. Therefore, we observed a decrease in magnetization when Ho concentration is increased. Considering all these reasons and the gains from the thesis studies, the works can be envisaged in the near future are listed below.

- The crystallite size of synthesized samples can be reduced by heat treatment process and its effects on magnetic and magnetocaloric properties should be studied.
- The Fe^{3+} substituting with Cr^{3+} ions effect on electrical properties of $CoCr_2O_4$ multiferroic material. Therefore, produced samples' electrical properties should be studied.
- Since we have already optimized the magnetic transition temperature of Co-based spinel materials, they can be used to form composite materials with another similar structure material which has large magnetic entropy change.
- Low Ho^{3+} ions concentrations (<10%) should be studied to overcome new crystal formations.

REFERENCES

Akyol, M. (2011). *Geçiş Metali Dy Katkılı Zn0.80-4yDyyOx Bileşiklerinin Yapısal ve Manyetik Özelliklerinin Araştırılması.* (Master of Science), Çukurova University, Adana, Turkey.

Akyol, M., Adanur, İ., Ayaş, A. O., & Ekicibil, A. (2017). Magnetic field dependence of magnetic coupling in CoCr2O4 nanoparticles. *Physica B: Condensed Matter, 525*(Supplement C), 144-148. doi:https://doi.org/10.1016/j.physb.2017.09.021

Akyol, M., Adanur, İ., Ayaş, A. O., Karadağ, F., & Ekicibil, A. (2018). Effect of boron content on structure and magnetic properties in CoFe2O4 spinel nanocrystals. *Journal of Alloys and Compounds, 744*, 528-534. doi:https://doi.org/10.1016/j.jallcom.2018.02.121

Bharathi, K. K., Markandeyulu, G., & Ramana, C. V. (2011). Structural, Magnetic, Electrical, and Magnetoelectric Properties of Sm- and Ho-Substituted Nickel Ferrites. *The Journal of Physical Chemistry C, 115*(2), 554-560. doi:10.1021/jp1060864

Bragg Law. (2020). Retrieved from https://www.xtal.iqfr.csic.es/Cristalografia/parte_05_5-en.html

Choi, K. R., Moon, S. J., Kouh, T., Shim, I. B., Kim, S. J., & Kim, C. S. (2009). Characterization of CoCr2O4 on Pt(111) Grown by Using Pulsed Laser Deposition. *Ieee Transactions on Magnetics, 45*(6), 2610-2612. doi:10.1109/Tmag.2009.2018913

Coey, J. M. D. (2010). *Magnetism and Magnetic Materials*. New York: Cambridge University Press.

Eisenmenger, J., & Schuller, I. K. (2003). Overcoming thermal fluctuations. *Nature Materials, 2*(7), 437-438. doi:10.1038/nmat934

Galdikas, A., Martūnas, Z., & Šetkus, A. (1992). SnInO-based chlorine gas sensor. *Sensors and Actuators B: Chemical, 7*(1), 633-636. doi:http://dx.doi.org/10.1016/0925-4005(92)80377-A

Goldman, A. (1999). *Handbook of Modern Ferromagnetic Materials* Boston: Kluwer Academic Publishers.

Gopal Reddy, C. V., Manorama, S. V., & Rao, V. J. (1999). Semiconducting gas sensor for chlorine based on inverse spinel nickel ferrite. *Sensors and Actuators B: Chemical, 55*(1), 90-95. doi:http://dx.doi.org/10.1016/S0925-4005(99)00112-4

He, H.-Y. (2014). Structural and Magnetic Property of Co1-xNixFe2O4Nanoparticles Synthesized by Hydrothermal Method. *International Journal of Applied Ceramic Technology, 11*(4), 626-636. doi:10.1111/ijac.12071

Iqbal, M. J., & Siddiquah, M. R. (2008). Electrical and magnetic properties of chromium-substituted cobalt ferrite nanomaterials. *Journal of Alloys and Compounds, 453*(1-2), 513-518. doi:10.1016/j.jallcom.2007.06.105

Ishibashi, H., & Yasumi, T. (2007). Structural transition of spinel compound at ferrimagnetic transition temperature. *Journal of Magnetism and Magnetic Materials, 310*(2), e610-e612. doi:10.1016/j.jmmm.2006.10.1131

Jr., W. F. B. (1959). Relaxational Behavior of Fine Magnetic Particles. *Journal of Applied Physics, 30*(4), S130-S132. doi:10.1063/1.2185851

Kamenskyi, D., Engelkamp, H., Fischer, T., Uhlarz, M., Wosnitza, J., Gorshunov, B. P., . . . Pronin, A. V. (2013). Observation of an intersublattice exchange magnon in CoCr2O4 and analysis of magnetic ordering. *Physical Review B, 87*(13). doi:ARTN 134423
10.1103/PhysRevB.87.134423

Karimunnesa, S., Ullah, A. K. M. A., Hasan, M. R., Shanta, F. S., Islam, R., & Khan, M. N. I. (2018). Effect of holmium substitution on the structural, magnetic and transport properties of CoFe2-xHoxO4 ferrites. *Journal of Magnetism and Magnetic Materials, 457*, 57-63. doi:https://doi.org/10.1016/j.jmmm.2018.02.077

Kim, B. N., Hiraga, K., Morita, K., & Sakka, Y. (2001). A high-strain-rate superplastic ceramic. *Nature, 413*(6853), 288-291.

Koseoglu, Y., Baykal, A., Toprak, M. S., Gozuak, F., Basaran, A. C., & Aktas, B. (2008). Synthesis and characterization of ZnFe(2)O(4) magnetic nanoparticles via a PEG-assisted route. *Journal of Alloys and Compounds, 462*(1-2), 209-213.

Kuncser, V., Keune, W., Vopsaroiu, M., Bissell, P. R., Sahoo, B., & Filoti, G. (2003). Easy axis distribution in modern nanoparticle storage media: A new methodological approach. *Journal of Optoelectronics and Advanced Materials, 5*(1).

Lawes, G., Melot, B., Page, K., Ederer, C., Hayward, M. A., Proffen, T., & Seshadri, R. (2006). Dielectric anomalies and spiral magnetic order in CoCr2O4. *Physical Review B, 74*(2). doi:ARTN 024413
10.1103/PhysRevB.74.024413

Leslie-Pelecky, D. L., & Rieke, R. D. (1996). Magnetic Properties of Nanostructured Materials. *Chemistry of Materials, 8*(8), 1770-1783. doi:10.1021/cm960077f

Li, C. L., Yan, T. Y., Barasa, G. O., Li, Y. H., Zhang, R., Fu, Q. S., . . . Yuan, S. L. (2018). Negative magnetization and exchange bias effect in Fe-doped CoCr2O4. *Ceramics International, 44*(13), 15446-15452. doi:https://doi.org/10.1016/j.ceramint.2018.05.200

Li, X.-H., Xu, C.-L., Han, X.-H., Qiao, L., Wang, T., & Li, F.-S. (2010). Synthesis and Magnetic Properties of Nearly Monodisperse CoFe2O4Nanoparticles Through a Simple Hydrothermal Condition. *Nanoscale Research Letters, 5*(6), 1039. doi:10.1007/s11671-010-9599-9

Muthuselvam, I. P., & Bhowmik, R. N. (2010). Connectivity between electrical conduction and thermally activated grain size evolution in Ho-doped CoFe2O4ferrite. *Journal of Physics D: Applied Physics, 43*(46), 465002. doi:10.1088/0022-3727/43/46/465002

Panneer Muthuselvam, I., & Bhowmik, R. N. (2010). Mechanical alloyed Ho3+ doping in CoFe2O4 spinel ferrite and understanding of magnetic nanodomains. *Journal of Magnetism and Magnetic Materials, 322*(7), 767-776. doi:https://doi.org/10.1016/j.jmmm.2009.10.057

SEM. (2020). Retrieved from https://www.mse.iastate.edu/research/sem/microscopy/how-does-the-sem-work/high-school/how-the-sem-works/

Shirsath, S. E., Mane, M. L., Yasukawa, Y., Liu, X., & Morisako, A. (2014). Self-ignited high temperature synthesis and enhanced super-exchange interactions of Ho3+–Mn2+–Fe3+–O2− ferromagnetic nanoparticles. *Physical Chemistry Chemical Physics, 16*(6), 2347-2357. doi:10.1039/C3CP54257B

Spinel structure. (2020). Retrieved from https://chem.libretexts.org/Bookshelves/Inorganic_Chemistry/Book%3A_Introduction_to_Inorganic_Chemistry/08%3A_Ionic_and_Covalent_Solids_-_Structures/8.07%3A_Spinel%2C_Perovskite%2C_and_Rutile_Structures

Tomiyasu, K., Fukunaga, J., & Suzuki, H. (2004). Magnetic short-range order and reentrant-spin-glass-like behavior in CoCr2O4 and MnCr2O4 by means of neutron scattering and magnetization measurements. *Physical Review B, 70*(21). doi:ARTN 214434 10.1103/PhysRevB.70.214434

Weiss, P. (1906). La variation du ferromagnetisme avec la temperature. *Comptes Rendus des Séances de l'Académie des Sciences, 143*, 1136-1139.

Willard, M. A., Kurihara, L. K., Carpenter, E. E., Calvin, S., & Harris, V. G. (2004). Chemically prepared magnetic nanoparticles. *International Materials Reviews, 49*(3-4), 125-170. doi:10.1179/095066004225021882

Yang, S., Bao, H. X., Xue, D. Z., Zhou, C., Gao, J. H., Wang, Y., . . . Otsuka, K. (2012). Magnetodielectric effect from the onset of ferrimagnetic transition in CoCr2O4. *Journal of Physics D-Applied Physics, 45*(26). doi:Artn 265001
10.1088/0022-3727/45/26/265001

Yousaf, M., Akhtar, M. N., Wang, B., & Noor, A. (2020). Preparations, optical, structural, conductive and magnetic evaluations of RE's (Pr, Y, Gd, Ho, Yb) doped spinel nanoferrites. *Ceramics International, 46*(4), 4280-4288. doi:https://doi.org/10.1016/j.ceramint.2019.10.149

Zakrzewska, K. (2001). Mixed oxides as gas sensors. *Thin Solid Films, 391*(2), 229-238. doi:10.1016/s0040-6090(01)00987-7

Zhang, H.-g., Wang, W.-h., Liu, E.-k., Tang, X.-d., Li, G.-j., Zhang, H.-w., & Wu, G.-h. (2013). Compensation effect and magnetostriction in CoCr2−xFexO4. *physica status solidi (b), 250*(7), 1287-1292. doi:10.1002/pssb.201248470

CURRICULUM VITAE

Semiramis GÜLKESEN was born in Adana, Turkey in 1991. She graduated from Bilfen High School College in 2010. After then, she recieved her B.S. from Material Science and Engineering department from the Erciyes University, in 2017. Then, she started her Master of Sceince degree in Nanotechnology and Engineering Science department at Adana Alparslan Türkeş science and Technology University. Her research areas are nano-particles and nano-magnetizm for technological applications. She has been working as an engineer at İsdemir for half a year.